DESIGN AND TESTING OF A

THERMOACOUSTIC POWER CONVERTER

A Thesis
Presented to
The Academic Faculty

by

Mark P. Telesz

In Partial Fulfillment
of the Requirements for the Degree
Masters of Science in the
School of Mechanical Engineering

Georgia Institute of Technology
August 2006

DESIGN AND TESTING OF A

THERMOACOUSTIC POWER CONVERTER

Approved by:

Dr. Tim C. Lieuwen, Advisor
School of Aerospace Engineering
Georgia Institute of Technology

Dr. Ben T. Zinn, Advisor
School of Mechanical Engineering
Georgia Institute of Technology

Dr. Samuel V. Shelton
School of Mechanical Engineering
Georgia Institute of Technology

Date Approved: May 16, 2006

ACKNOWLEDGEMENTS

The work that this thesis encompasses was made possible with the support of many individuals. First of all I thank Dr. Wayne Whiteman and the Center for Distance Learning Staff at Georgia Tech who helped with the logistical issues that made this "distance learning" thesis possible. Thanks also to my advisor Dr. Tim Lieuwen whose flexibility and technical guidance, especially at the onset of work when I was absolutely lost in the science, enabled me to get past those initial barriers. Moreover, I appreciate Dr. Ben Zinn and Dr. Samuel Shelton for taking the time and serving on my reading committee.

I also have a great deal of gratitude for Dr. Scott Backhaus of Los Alamos National Laboratory whose knowledge and experience in thermoacoustic engines and their application, fabrication and troubleshooting is probably unparalleled. His insight on a variety of topics was not only valuable but the way that he seemed to drop everything and immediately answer all of my questions, whenever I asked, truly impressed me.

Thanks as well to my co-workers Dr. Josef Parrington, Mr. Trevor Munroe, Mr. Joe Nehrbauer, Mr. Bill Johnson, Mr. John Wuthrich, Dr. Martin Pollack and Dr. Brian Aviles and also Dr. Robert Keolian of Penn State whose diverse expertise, guidance, support, flexibility and encouragement enabled me to produce a functioning device to be proud of in only fourteen months.

TABLE OF CONTENTS

ACKNOWLEDGEMENTS III

LIST OF TABLES VII

LIST OF FIGURES VIII

LIST OF SYMBOLS XIII

SUMMARY XVII

CHAPTER 1: INTRODUCTION 1

CHAPTER 2: BACKGROUND 4
2.1 History 4
2.2 Important Length Scales 8
2.3 Thermoacoustic Engines 10
2.3.1 Standing wave 12
2.3.2 Traveling wave - Stirling 15
2.3.2.1 Thermodynamics 15
2.3.2.2 Acoustic Network 17
2.4 Electroacoustic Power Transducer 22

CHAPTER 3: DESIGN 23
3.1 Clarifying the Design Task 23
3.2 Embodiment Design 24
3.3 Detail Design 26
3.3.1 Linear Alternators 26
3.3.2 DeltaE Computer Model 29
3.3.3 TAPC Engine 31
3.3.3.1 Thermodynamic Section 33
3.3.3.1.1 Hot Heat Exchanger (HHX) 35
3.3.3.1.2 Regenerator 40
3.3.3.1.3 Thermal Buffer Tube (TBT) 42
3.3.3.1.4 Ambient Heat Exchanger (AHX) 43
3.3.3.2 Acoustic Section 45
3.3.3.2.1 Compliance 45

3.3.3.2.2 Feedback Inertance Tube 46
3.3.3.2.3 Centerplate 48
3.3.3.2.4 Alternator Vessel 50
3.3.3.2.5 Jet Pump 50

CHAPTER 4: EXPERIMENT SET-UP 54
4.1 Measurements 54
4.1.1 Temperature 54
4.1.2 Pressure 55
4.1.2.1 Static Pressure 56
4.1.2.1.1 Dial Gauges 56
4.1.2.1.2 Piezoresistive Pressure Transducers 56
4.1.2.2 Dynamic Pressure 56
4.1.2.2.1 Piezoelectric Pressure Transducers 56
4.1.3 Alternator Piston Location 57
4.1.4 Power 58
4.1.4.1 Heat Input 58
4.1.4.2 Acoustic Power 59
4.1.4.2.1 Two Pressure Sensor Method 59
4.1.4.2.2 Alternator Piston Motion Method 60
4.1.4.3 Electric Output 61
4.2 Supporting Devices 62
4.2.1 Heat Source 64
4.2.1.1 Temperature Controller 64
4.2.1.2 DC Power Supply 64
4.2.2 Heat Sink 65
4.2.3 Power Amplifier 65
4.3 Data Acquisition System 65
4.3.1 Hardware 65
4.3.2 Software 66

CHAPTER 5: TESTING 69
5.1 Initial Shakedown Testing 69
5.1.1 Lessons Learned - Rubbing Alternator Pistons 74
5.2 Further Testing 76
5.2.1 Lessons Learned - Acoustic Streaming 78
5.2.1.1 Gedeon Streaming 78
5.2.1.2 Boundary-layer TBT Streaming 82
5.2.1.3 Jet-Driven Streaming 82
5.3 Performance Testing To Date 83
5.3.1 70 Watt Test Runs 84

CHAPTER 6: CONCLUSIONS 88
6.1 Recommended Work 89
6.1.1 Larger Jet Pump 89
6.1.2 Secondary Ambient Heat Exchanger 89

6.1.3 Flow Straighteners 90
6.1.4 New Alternators 90
6.1.5 Internal Thermocouples 91

APPENDIX A: DELTAE INPUT/OUTPUT FILE 92

APPENDIX B: PRESSURE VESSEL ANALYSIS 101
B.1 Materials 101
B.2 Hydrostatic Pressure Test 103
B.2.1 Hydrostatic test pressure calculation 103
B.3 Pressure Containment 106
B.3.1 Fill System 106
B.3.2 TAPC System 106
B.4 Pressure Vessel Analysis 107
B.4.1 Hot Heat Exchanger stay cross-sectional area 108
B.4.2 Stayed plate thickness 109
B.4.3 Hot Heat Exchanger plug fillet welds 110
B.4.4 Regenerator and Thermal Buffer Tube wall 111
B.4.5 Thermal Buffer Tube and Regenerator lap joint loose type flanges 112
B.4.6 Ambient Heat Exchanger wall thickness 115
B.4.7 Compliance volume 117
B.4.8 Inertance tube wall thickness 122
B.4.9 Centerplate 122
B.4.10 Alternator Vessel 126
B.4.11 Jet Pump 132
B.4.12 Other Components 133

REFERENCES 134

LIST OF TABLES

Table 2.1: Approximate temperature oscillations resulting from various sounds in standard temperature and pressure air 4

Table 2.2: Network Analogies 21

Table B.1: Allowable stresses of the materials that make up the TAPC [4] 102

Table B.2: Inconel 625 pre and post heat treatment tensile data (at room temp) 103

Table B.3: Maximum pressure by calculation 105

Table B.4: Fill system components 106

Table B.5: Allowable Stress in Inconel 625 Grade 2 [4] 107

Table B.6: Component pressure ratings. 133

LIST OF FIGURES

Figure 1.1: Energy conversions within a Thermoacoustic Power Converter 1

Figure 2.1: Original concept for two acoustic engines mounted in opposition for vibration balance. Reproduced from U.S. Patent No. 2,836,033 (1958) [9] 5

Figure 2.2: The thermoacoustic Stirling engine concept. Reproduced from US Patent No. 4,355,517 (1982) [11]. 6

Figure 2.3: Los Alamos National Laboratory's 1kW thermoacoustic-Stirling heat engine (TASHE) [11] surrounded by its designers..... 7

Figure 2.4: Northrop Grumman and Los Alamos National Lab traveling-wave thermoacoustic electric generator [15]. Another view of the engine portion is shown in Figure 3.1(b). 8

Figure 2.5: Soundhauss tube demonstration. The porous plug of aluminum foam is heated on one side with a battery powered nichrome wire and cooled on the other with the air that streams into the tube. The resonating tube emits a loud tone when the wire is heated and effectively demonstrates a thermoacoustic engine. A small speaker is mounted on the right side to represent the linear alternator and provide a complete model of the Thermoacoustic Power Converter. 9

Figure 2.6: Standing wave thermoacoustic engine schematic ¼λ in length. Also shown is a stainless-steel parallel plate stack [18]..... 13

Figure 2.7: Single gas parcel within the stack during "standing wave" displacement towards the cold side. 13

Figure 2.8: Gas pressure distribution within a standing wave resonator that is closed on the left end and opened on the right, so it has length $\lambda/4$. The red and blue sides of the stack represent hot and cold. The bold lines are the pressure and velocity distributions within the tube at time zero and the thin lines are the same quantities one-half of the acoustic cycle in time later ($\frac{1}{2}\omega^{-1}$). 14

Figure 2.9: Single gas parcel within the regenerator during "traveling-wave" displacement towards the cold side. 16

Figure 2.10: Stirling cycle pressure versus volume diagram..... 17

Figure 2.11: TAPC component layout. 20

Figure 2.12: TAPC system simple oscillator analogy 22

Figure 3.1: Thermoacoustic-Stirling heat engines. (a) LANL 1kW design [13]. (b) Northrop Grumman/LANL design [15]. (c) and (d) are schematics of the engines' internals with their corresponding parts labeled. 24

Figure 3.2: TAPC vibration balanced component layout 25

Figure 3.3: TAPC model final revision. (a) isometric view and (b) cross-section. 26

Figure 3.4: Four views of the CFIC, Inc. *1S102M STAR*™ linear alternators [2]. 29

Figure 3.5: TAPC drawings: (a) front view and (b) cross-section, (c) side view and (d) cross-section 32

Figure 3.6: Thermodynamic Section. (a) Assembly drawing. (b) Full-scale cross-section plastic rapid-prototype model used to assist discussions with the machinist. The "integral stays," thin tube walls, Regenerator side central "post" and the blue plugs to be fillet welded are shown. (c) Individual components prior to weld. (d) Ready for first spot weld tack on Regenerator housing. (e) Ready for final assembly. (f) Post-weld inside diameter bore in a milling machine. 35

Figure 3.7: Computer model of helium flowing through the Hot Heat Exchanger rectangular duct as heat is applied to the four cartridge heater holes. The temperature gradients in degrees Fahrenheit are shown in (a), (b) and (c) with arbitrary insulation surrounding the component. The heat flux is in (d). 37

Figure 3.8: Hot Heat Exchanger. Views of gas flow path in (a) and (b). (c) Outlets to Thermal Buffer Tube and Regenerator. (d) Insertion of cartridge heaters. 39

Figure 3.9: Regenerator hardware. (a) Empty screen canister ready to be filled with 419 cleaned 1.202 inch diameter 180 mesh screens. (b) Assembled stack 1.565 inches tall. (c) Looking into HHX from Regenerator housing prior to Thermodynamic Section welding. 42

Figure 3.10: Ambient Heat Exchanger. (a) Prior to assembly. (b) During assembly, shows configuration of "water jacket" with respect to the inlet and outlet ports. (c) Looking down from Regenerator side. (d) View from Compliance volume 45

Figure 3.11: The empty space with the diameter and length shown makes up the Compliance Volume. 46

Figure 3.12: Inertance Tube. 47

Figure 3.13: Centerplate. (a) view of the radius on the TBT sided bore, (b) view of the alternator piston looking through the compression space, (c) alternator mounted to Centerplate, (d) a few layers of 24 wires per inch copper mesh that serve as a TBT flow straightener and a secondary heat exchanger, (e) rapid prototype plastic model of ½ of the Centerplate, made to assist in design and manufacturing discussions and (f) mounted alternator wired to electrical feedthru and ready to be housed within the alternator vessel. 49

Figure 3.14: Jet Pump. (a) full assembly, (b) zoomed-in view of the tapered region depicting the 1st order acoustic velocity during the two halves of the acoustic cycle [51], (c) small jetting area was adjusted and determined by the amount of exposed Jet Pump thread, (d) exposed thread, (e) 0.900 inch diameter Jet Pump looking down from AHX side, (f) Inertance Tube inlet radius, (g) 0.875 inch and (h) 0.625 inch diameter Jet Pumps, (i) Jet Pump in lathe and (j) three different diameter Jet Pumps side by side. 53

Figure 4.1: Sensor locations 55

Figure 4.2: (a) LVDT core mounted to the alternator's piston. (b) Alternator and its core mounted to the Centerplate of the TAPC, prior to the Alternator Vessel being bolted on. 58

Figure 4.3: Load circuit for the TAPC. The power analyzer is wired in parallel with the resistive load to monitor voltage and in series between the alternators and rheostat in order to read the current through the load. It is noted that "less load" is synonymous with a higher load resistance because it means less current is going through the circuit and is effectively approaching an "open" condition. A lower rheostat value allows more current to flow with a limit of 0Ω causing a "closed circuit." 62

Figure 4.4: TAPC test facility during operation. 63

Figure 4.5: TAPC data display during operation. 68

Figure 5.1: Updated TAPC circuit includes a 3-way switch. 70

Figure 5.2: Alternator piston peak-to-peak stroke (normalized by input AC power) versus motoring frequency at various temperatures during shakedown Test #2. The resonance frequency becomes more defined as temperature is increased. 72

Figure 5.3: Quality factor inverse as a function of temperature. This factor is based on the average resonance plots in Figure 5.2 72

Figure 5.4: TAPC engine-linear alternator system stability. If there is sliding friction within the alternator, it will need to be kick-started [78]. 76

Figure 5.5: TAPC system stability. Useful power production and un-useful power dissipations are plotted as a function of the pressure or voltage amplitude squared. The linear alternator under a resistive load is naturally unstable [78]. 77

Figure 5.6: Temperature distributions over the normalized thermodynamic section for various Jet Pump positions. Each line is a different test run and small jetting area, which are given in the legend. The black lines are the ideal temperature profiles between the respective hot and cold ends of the Thermal Buffer Tube and Regenerator [15]. 80

Figure 5.7: Regenerator temperature profile vs. the small end jetting area. 81

Figure 5.8: Boundary-layer TBT streaming causes a DC "annular convection roll" [13]. The radial mass-flux causes a DC enthalpy stream downward towards the alternators near the walls and upward in the middle. 82

Figure 5.9: Jet-driven streaming in the TBT as described in Reference [18]. There is a flow straightener at the bottom entrance, but no straightener at the top bordering the HHX. (a) 10° spread angle of the jets leaving the HHX. (b) Broadly distributed flow profile leaving the copper mesh flow straightener screens at the interface to the Centerplate. The superposition of these profiles result in a (c) normal oscillating "plug" flow and a (d) "convection roll" like the boundary-layer driven streaming. 83

Figure 5.10: Alternator stroke and power output during a 70 watt test run. The crossing point between the two alternator stroke plots is the result of inaccuracies in the data. 86

Figure 5.11: Acoustic pressure during a 70 watt test run 87

Figure B.1: Post bend test sample. Multiple 180° bend tests were performed in accordance with and qualified per Reference [81] on welded samples of the Grade 2 Inconel. Both sides of the weld saw strain by bending different samples in each of the two directions. 102

Figure B.2: TAPC assembled, secured and ready for the hydrostatic pressure test. It was mounted in this position in order to utilize the large LVDT entry hole for filling with water. 105

Figure B.3: TAPC fill system schematic 106

Figure B.4: TAPC heat input control system 107

Figure B.5: Hot Heat Exchanger cross-sectional views..... 108
Figure B.6: Thermal Buffer Tube and Regenerator..... 111
Figure B.7: Ambient Heat Exchanger drawing. (a) top view and (b) cross-section..... 116
Figure B.8: Compliance..... 118
Figure B.9: Centerplate flange assembly cross-section..... 123
Figure B.10: TAPC cross-section through Alternator Vessels..... 126
Figure B.11: Jet Pump assembly..... 132

LIST OF SYMBOLS

English letters

A	cross-sectional area of a duct (Eqs. 2.3, 2.5, 2.8, 2.9, 4.2, 4.3)
A_p	cross-sectional area of alternator piston (Eq. 4.5)
B	magnetic field (Section 2.4)
C	compliance, a duct's volume to pressure ratio (Eq. 2.7)
c_p	constant pressure heat capacity per unit mass (Eq. 2.1)
D_p	drag on piston (Eq. 5.1)
D_{wire}	wire diameter in mesh screen (Eq. 3.2, 3.3)
E_2	acoustic power (Eqs. 2.4, 4.2, 4.3)
I	acoustic intensity (Eq. 4.1, 4.2)
i	$\sqrt{-1}$ (Eq. 2.5)
K	spring constant (Eq. 3.1)
k	thermal conductivity (Eq. 2.1)
L	inertance (Eq. 2.8)
M	mass (Eq. 3.1)
M_p	piston mass (Eq. 5.1)
M_2	time-averaged second order DC mass flux, Gedeon Streaming (section 3.3.3.2.5)
n	number of screens per inch, wire mesh number (Eq. 3.2)
p	pressure (Eq. 4.1, 4.2)
p_m	mean pressure (Eqs. 2.5, 2.7, 2.10)
p_1	complex pressure amplitude (Eq. 2.4), $pressure(t) = \lvert p_1 \rvert \cos(\omega t + \phi) = \mathrm{Re}\left[P_1 e^{i\omega t}\right]$
p_{1c}	acoustic pressure amplitude in compression space (Eq. 4.4)

Q quality factor of resonance (Eq. 5.1, 5.2)

R resistance (Section 3.1.1)

R_v viscous resistance (Eq. 2.9)

R_κ thermal relaxation resistance (Eq. 2.10)

r_h hydraulic radius (Eq. 2.3, 3.3)

S surface area (Eq. 2.10)

t time (Eq. 4.1, 4.2)

T temperature in Kelvin (Eq. 5.3)

T_h Regenerator's hot face temperature (Eq. 2.6)

T_c Regenerator's cold face temperature (Eq. 2.6)

V volume of a duct (Eq. 2.7)

v velocity (Eq. 4.1, 4.2)

U_1 complex volumetric velocity amplitude (Eq. 2.4), $U(t) = |U_1|\cos(\omega t + \phi) = \mathrm{Re}\left[U_1 e^{i\omega t}\right]$

U_{1p} volumetric velocity amplitude of piston (Eq. 4.4)

x position (Eqs. 2.5, 2.8, 2.9, 4.3)

X_{mech} mechanical reactance (Eq. 3.1)

X_{pp} peak to peak volumetric stroke (displacement) of helium (Figure 5.2)

Z acoustic impedance, ratio of pressure to velocity (Eq. 2.11)

Greek letters

γ ratio of isobaric to isochoric specific heats (Eq. 2.5, 2.7, 2.10)

Δ difference (Section 5.2.1)

δ_k thermal penetration depth (Eq. 2.1, 2.10)

δ_v viscous penetration depth (Eq. 2.2, 2.9)

η_a alternator efficiency – ratio of acoustic power to electrical output (Section 3.1)

η_{Carnot} Carnot efficiency – thermodynamic limit (Eq. 5.3)

η_e engine efficiency – ratio of heat input to acoustic power output (Section 3.1)

η_T TAPC efficiency – ratio of heat input to electrical output (Section 3.1)

$\theta_{p\xi}$ phase angle between compression space pressure and piston motion (Eq. 4.6)

λ wavelength (Section 2.3)

μ dynamic viscosity (Eqs. 2.2, 2.9)

ϕ_{pU} phase angle between p_1 and U_1 (Eq. 2.4)

ρ density (Eqs. 2.1, 2.2)

ρ_m mean density (Eqs. 2.8, 4.3)

Ω ohms (sections 4.1.4.3, 5.1)

Φ porosity (Eqs. 3.2, 3.3)

ω angular frequency (Eqs. 2.1, 2.2, 2.5, 2.10, 3.1, 4.3)

ω_r resonant angular frequency (Eq. 5.2)

ξ gas displacement amplitude (Sections 2.2, 3.3.3.1.1), $|\xi_1| = |U_1|/\omega A$

Π perimeter (Eq. 2.3)

π 3.141592…

T averaging time (Eq. 4.1)

τ temperature ratio (Eq. 2.6)

Acronyms

AC Alternating Current

AHX Ambient Heat Exchanger

ASME American Society of Mechanical Engineers

ASTM American Society of Testing and Materials

DAQ Data Acquisition

DC	Direct Current
DeltaE	Design Environment for Low-Amplitude Thermoacoustic Engines [3]
dB	decibels
EDM	electro-discharge machining
FFT	Fast Fourier Transform
He	Helium
HHX	Hot Heat Exchanger
LVDT	Linear Variable Differential Transducer
OFHC	oxygen free high conductivity, referring to a type of copper
Pr	Prandtl number (Section 2.3)
psi	pounds per square inch
psig	pounds per square inch gauge, referring to internal TAPC pressure
REG	Regenerator
RMS	Root Mean Square
TAPC	Thermoacoustic Power Converter
TASHE	Thermoacoustic-Stirling Heat Engine
TBT	Thermal Buffer Tube
UNS	Unified Numbering System

SUMMARY

Thermoacoustic engines convert heat into acoustic pressure waves with no moving parts; this inherently results in high reliability, low maintenance and low manufacturing costs. Significant increases in the performance of these devices have enabled rivalry with more mature energy conversion methods in both efficiency and power output. This optimal production of acoustic power can be ultimately used to achieve cryogenic temperatures in thermoacoustic refrigerators, or can be interfaced with reciprocating electro-acoustic power transducers to generate electricity.

This thesis describes the design, fabrication and testing of a Thermoacoustic Power Converter. The system interfaces a thermoacoustic-Stirling heat engine with a pair of linear alternators to produce 100 watts of electricity from a heat input. It operates with helium at 450 psig internal pressure and a hot side temperature of 1200°F. Through thermoacoustic phenomena, these conditions sustain a powerful pressure wave at a system specific 100 Hz. This pressure wave is used to drive the two opposed linear alternators in equal and opposite directions to produce a single phase AC electrical output at that same system frequency. The opposing motion of the two alternators enables a vibration-balanced system.

The engine has created 110 watts of acoustic power and the complete Thermoacoustic Power Converter system has produced 70 watts of AC electricity. Compensating for some heat leaks, the converter reaches 26.3% heat to acoustic power efficiency and 16.8% heat to electric efficiency when those maximum values are

achieved. This conversion of heat to acoustic power is 40% of the Carnot thermodynamic efficiency limit.

CHAPTER 1

INTRODUCTION

The Thermoacoustic Power Converter (TAPC) developed in this thesis combines a hybrid thermoacoustic-Stirling heat engine with an electro-acoustic power transducer. The thermoacoustic engine portion of this device effectively converts heat into an acoustic pressure wave within a vessel of inert gas without any moving parts. This pressure wave is then used to cycle a pair of electro-acoustic power transducers, specifically linear alternators, in order to produce an electrical output. This conversion process is pictorially represented in Figure 1.1.

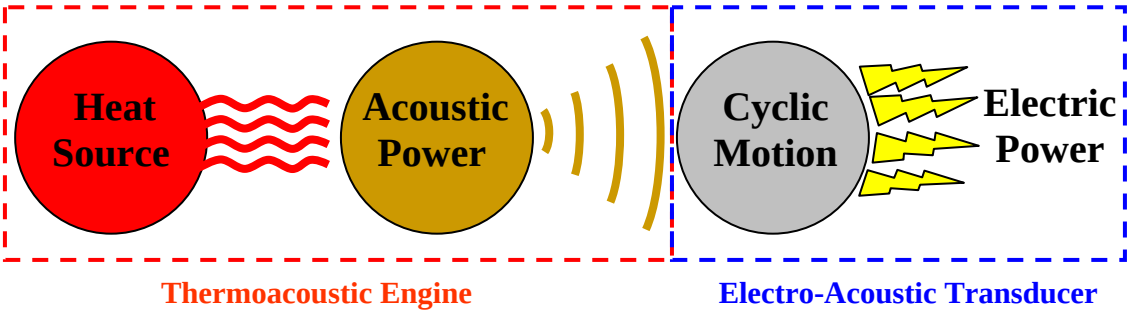

Figure 1.1: Energy conversions within a Thermoacoustic Power Converter

This design attempts to improve upon a thermoacoustic-Stirling engine and linear alternator combination previously developed [1] that achieved 58 watts of electricity at 18% heat to electric efficiency. It was aspired to improve upon these statistics, so design goals were set at 100 watts electric and 20% system efficiency. Based on these objectives, linear alternators were sized accordingly and procured from a motor/alternator manufacturer [2]. After obtaining the alternators' specifications, work to design a suitable thermoacoustic-Stirling engine portion of the converter began with the

application of a first-principles accurate modeling program, namely Los Alamos National Laboratory's DeltaE (Design Environment for Low-amplitude Thermoacoustic Engines) [3]. This code numerically integrates a one-dimensional wave equation over any geometry and with any working gas for a complete engine-alternator combination.

The design of the TAPC was approached with modularity in mind, as the performance is dependent on the harmonization of a variety of components. This approach enables the ability to relatively easily change components under the circumstance that performance might be lacking as the result of a certain part. Such an approach was considered necessary because crucial issues might be overlooked during the design phase. Hence, wherever possible, welds were substituted with flanges in order to easily accommodate new components if any of these issues arose during testing.

The TAPC is subjected to high internal pressure and, in certain locations, temperature, so the design was structurally analyzed per the ASME Boiler and Pressure Vessel Code [4]. Also per this code, and prior to testing, the assembled pressure vessel was hydrostatically pressurized and confirmed to be capable of maintaining the internal operating pressures.

The power produced by the TAPC is dissipated in a rheostat and read with both analog voltage and amperage meters and a power analyzer. Electrical control of the device and power peaks are determined by manually changing the electrical load (rheostat) on the alternators.

In order to quantify the performance, the TAPC was outfitted with a series of sensors to monitor the temperatures, pressures (both static and dynamic), and the alternator's motion. The dynamic data acquired was high frequency and care was taken in putting together a sufficient data acquisition system. This system had to display real time and accurate data in order to enable active and immediate control.

This Thesis describes the research and basic science, modeling, design process, fabrication, testing, analysis and performance to date of the TAPC. Specifically, Chapter

2 reviews the science of various thermoacoustic devices and their respective components. Chapter 3 details the TAPC design by discussing the computer model, material issues, manufacturing, assembly, structural analyses and functionality. Chapter 4 looks into the experimental set-up and operation by detailing the various sensors and measurements. Chapter 5 discusses both the shakedown and performance to date testing of the TAPC and finally Chapter 6 concludes the thesis by developing recommendations for future work.

CHAPTER 2

BACKGROUND

When a sound wave travels through air or any other compressible fluid it creates pressure, motion and temperature oscillations in that media. In other words, if a particular gas molecule experiences a sufficiently rapid pressure increase from an acoustic wave, such that the heat doesn't have time to flow away, its temperature will rise. Yet in normal day-to-day audio acoustics, this physical relationship is unimportant [5], as is shown explicitly why in Table 2.1. Recently though, this interaction has been harnessed in thermoacoustic engines, in order to efficiently produce a pressure wave from a temperature gradient.

Table 2.1: Approximate temperature oscillations resulting from various sounds in standard temperature and pressure air

Sound	Sound-Pressure Level (dB)	Sound Pressure (psi)	Temperature Oscillation (°F)
Whispering	30	10^{-7}	$\pm 10^{-6}$
Speaking	70	10^{-6}	$\pm 10^{-4}$
Shouting	90	10^{-5}	$\pm 10^{-3}$
Pain Threshold	120	10^{-2}	$\pm 10^{-2}$

2.1 History

Thermoacoustics, the interaction between heat and sound, was first noticed in the mid 19th century when glassblowers observed that when a hot glass bulb was attached to a cooler tube, it would emit a tone [6]. This noise emitter became known as a Soundhauss tube after a German who quantitatively investigated the sounds. Towards

the end of the 1800's, Lord Rayleigh, a British physicist, qualitatively understood that these heat-driven tones (thermoacoustic pressure oscillations) would occur if heat flowed into the gas while its density is high and out of the gas while its density is low [7]. However, up thru the mid 20th century these coupled pressure and temperature oscillations in a Soundhauss tube were considered nothing more than a science demonstration that could make a loud noise.

Around 1950 Bell Telephone Laboratories received a few patents [8, 9] for devices that would use this thermoacoustic phenomenon to produce electricity, i.e. the very first "thermoacoustic power converter" concepts, see Figure 2.1. These devices would convert heat (from an open flame) into a pressure wave (acoustic power) with a thermoacoustic engine (synonymous to a Soundhauss tube), and then the acoustic power was converted into electricity by cycling an acoustical-to-electrical transducer (basically a speaker tasked to operate in reverse, i.e. motion conversion to electricity). The concept for these devices was attractive because the conversion of heat into acoustic power required no moving parts, hence they were relatively inexpensive to build, reliable and would require a low amount of maintenance. However, they weren't considered applicable because the conversion of heat into acoustic power was not very efficient (<10%) and furthermore, the pressure oscillations were relatively weak.

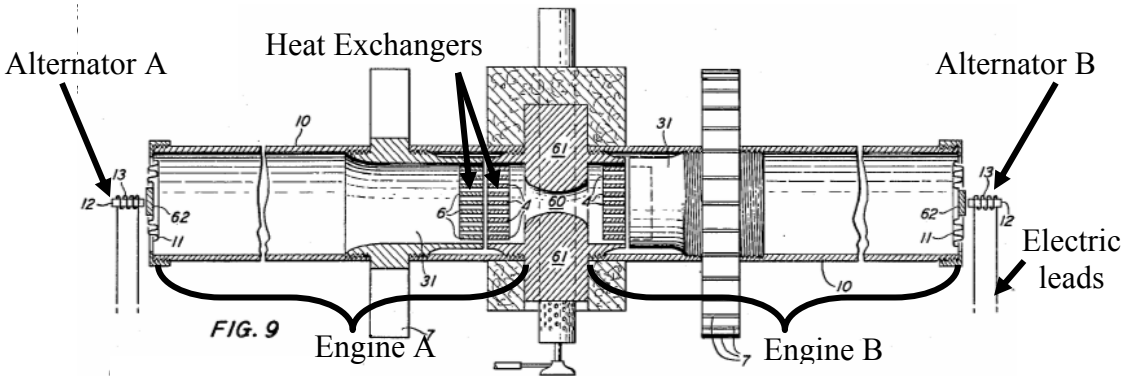

Figure 2.1: Original concept for two acoustic engines mounted in opposition for vibration balance. Reproduced from U.S. Patent No. 2,836,033 (1958) [9]

However, in 1979 [10] it was recognized that much better thermoacoustic engine efficiencies (heat into acoustic power) could be achieved if the acoustic wave produced was forced to undergo phasing similar to the inherently reversible and thus highly thermal efficient Stirling thermodynamic cycle. This insight merged 150 years of Stirling Engine technology with the newer thermoacoustic engine concepts. What resulted was improved reliability through the idea to substitute the Stirling engine's sliding and wearing piston, rotating crankshaft and moving connecting rods with solely the acoustic wave's inertia within the working gas; it was predicted that this could occur with no sacrifice of Stirling engine efficiency. This realization led to an invention [11], shown in Figure 2.2, that achieved the sought after simplicity and reliability through the elimination of moving parts. However, it was unsuccessful at actually amplifying the acoustic power.

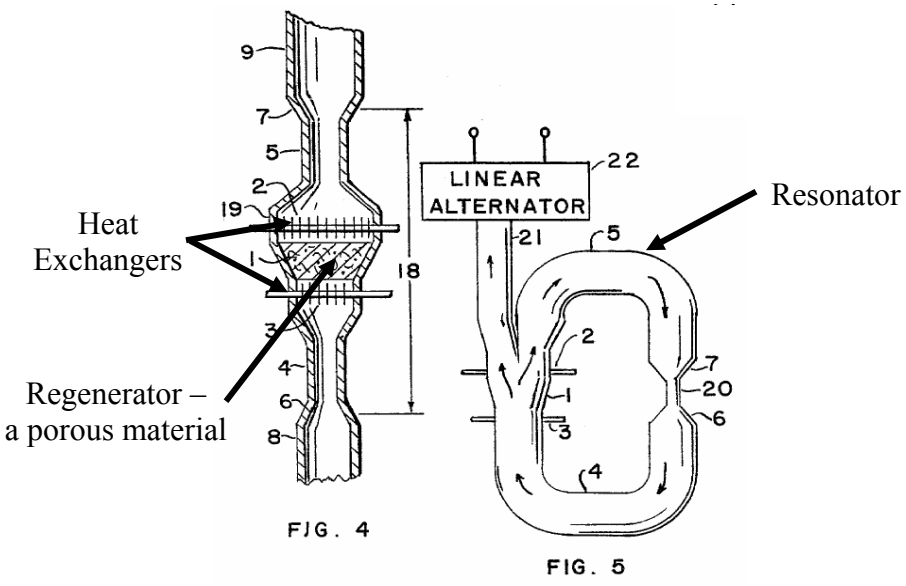

Figure 2.2: The thermoacoustic Stirling engine concept. Reproduced from US Patent No. 4,355,517 (1982) [11].

It wasn't until 1998 that this concept of a thermoacoustic-Stirling hybrid engine was demonstrated [12], although its efficiency was lower than expected because of unanticipated heat and viscous losses. However, a year later the bulk of these heat losses

were accounted for and an acoustical method to counteract the viscous losses was devised, this resulted in the high efficient hybrid engine that was first conceived of twenty years earlier [13], which is shown in Figure 2.3. Specifically, this new type of engine converted 30% of the heat input into acoustic power, which was 50% better than the most efficient of the non-hybrid thermoacoustic engines. In fact, this performance even rivaled the much more mature generic Stirling engine which currently operates at 20%-38% thermal to mechanical efficiency [14].

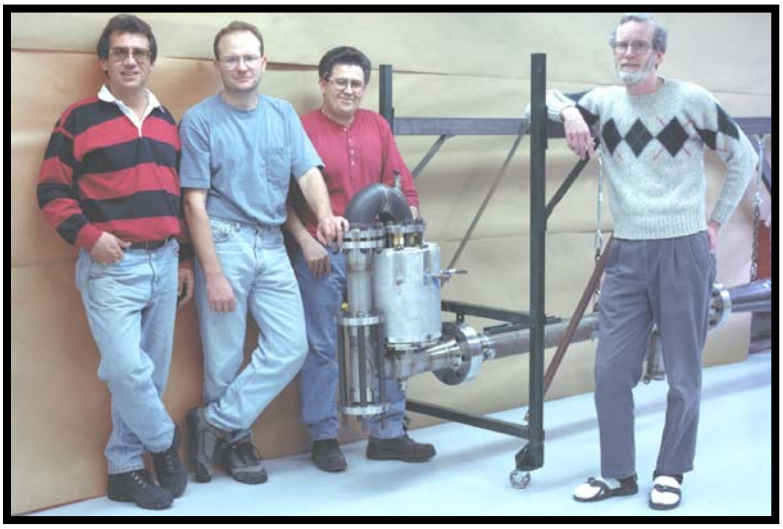

Figure 2.3: Los Alamos National Laboratory's 1kW thermoacoustic-Stirling heat engine (TASHE) [11] surrounded by its designers.

In 2003 a smaller version of that highly efficient thermoacoustic-Stirling hybrid engine was effectively joined to a pair of linear alternators (electro-acoustic power transducers), Figure 2.4, in order to take another step and produce useful electricity from the engine's powerful acoustic wave. Even though this was a first of its kind "proof-of-concept" project, the unit maintained a heat to acoustic power efficiency near the 30% reference and actually produced 57 watts of electricity at up to 17.8% thermal to electric efficiency [15].

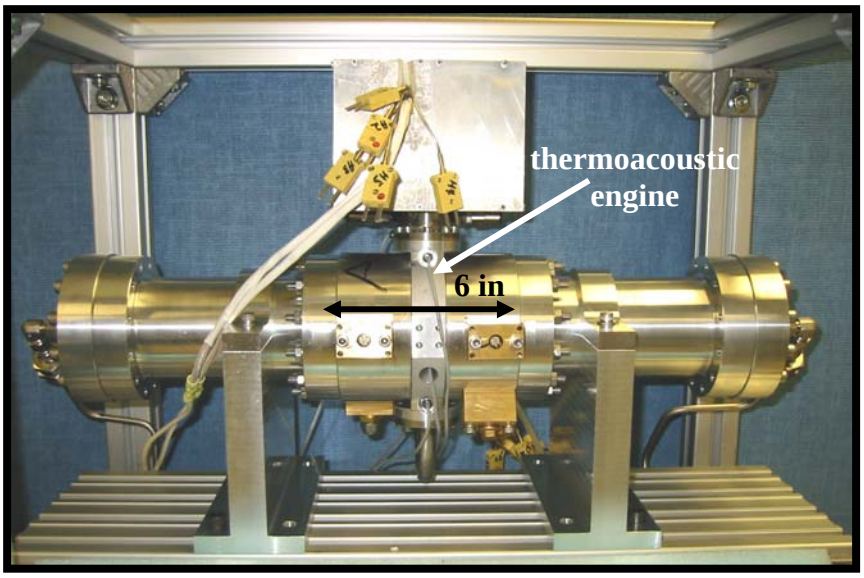

Figure 2.4: Northrop Grumman and Los Alamos National Lab traveling-wave thermoacoustic electric generator [15]. Another view of the engine portion is shown in Figure 3.1(b).

2.2 Important Length Scales

In order to produce pressure oscillations capable of doing useful work in thermoacoustic engines, the working gas must handle a large temperature span. This is accomplished by putting the gas in contact with a solid that inherently has a much greater heat capacity which imposes a temporally isothermal boundary condition on the gas [16]. Now the solid will tend to keep the temperature of the gas, which is carrying a sound wave, stable as it both absorbs the heat of compression and exudes heat of expansion. This idea was first realized when a short, relative to the tube, porous metal gauze was placed inside a Soundhauss tube [17], see Figure 2.5.

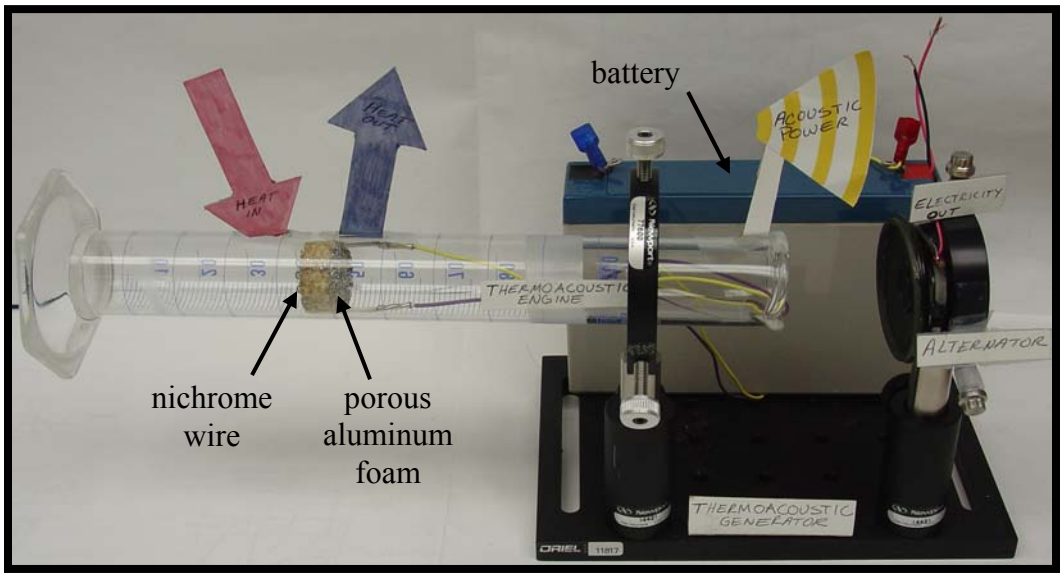

Figure 2.5: Soundhauss tube demonstration. The porous plug of aluminum foam is heated on one side with a battery powered nichrome wire and cooled on the other with the air that streams into the tube. The resonating tube emits a loud tone when the wire is heated and effectively demonstrates a thermoacoustic engine. A small speaker is mounted on the right side to represent the linear alternator and provide a complete model of the Thermoacoustic Power Converter.

The thermal interaction of the sound wave with the solid boundary stimulates a heat flux along the solid, thus it is important to note the distance over which the diffusion of heat to or from the solid occurs. This distance is known as the thermal penetration depth and it is a function of the sound wave's frequency and the gas' properties [18]:

$$\delta_\kappa = \sqrt{\frac{2k}{\omega \rho c_p}} \tag{2.1}$$

The heat exchanger components of a thermoacoustic engine must have lateral dimensions comparable to this depth in order to ensure sufficient heat exchange between the solid and the working gas.

Likewise, the viscous penetration depth is the lateral distance (perpendicular to the gas motion) that momentum can diffuse in a period of oscillation divided by π (ω^{-1}):

$$\delta_\upsilon = \sqrt{\frac{2\mu}{\omega \rho}} \tag{2.2}$$

When the gas is at distances to the nearest solid much greater than these depths, the gas experiences no thermal or viscous contact.

The degree of interaction that an acoustic wave has with a solid boundary can be measured by comparing these penetration depths with the average distance between the gas and solid, namely the hydraulic radius:

$$r_h = \frac{A}{\Pi} \tag{2.3}$$

This distance can be considered a ratio of the gas volume to the gas-solid contact area.

Another important length is the displacement amplitude of the gas, ξ, which, in terms of a thermoacoustic engine, is the absolute distance that a gas particle travels during half of the sound wave's period. In other words, it is the peak-to-peak length of the gas' position oscillation within the acoustic wave. This is an important dimension because it limits the length of the heat exchangers in thermoacoustic engines [19]. Basically, each gas molecule only travels a limited distance because of the oscillatory nature of the gas motion, thus having a heat exchanger longer than this distance has no benefit. This displacement amplitude is much larger then the previously mentioned penetration depths in a thermoacoustic engine, note that the opposite holds true in normal audio acoustics.

2.3 Thermoacoustic Engines

The function of a thermoacoustic heat engine is to produce net work from heat in the form of an acoustic pressure wave, thus the conventional device will contain a pressurized compressible fluid that is capable of sustaining acoustic oscillations. The choice of gas in these devices often involves a compromise between power, efficiency and what is available for laboratory use [18]. Thermoacoustic power is generally proportional to the gas' speed of sound, its mean pressure and the cross-sectional area dedicated to heat input [20]. Obviously pumping the engine to a higher mean pressure or

using a gas that can support a greater speed of sound will result in the best volumetric power density.

Even though similar work with other gases has been proven [21], the light gas helium (Grade 5.0, 99.999% pure He, was used during the testing of the TAPC, however Grade 3.0 would be good enough) is often used because:

- high speed of sound
- high thermal conductivity - results in larger thermal penetration depth (beneficial until a high mean pressure counteracts it)
- low Prandtl (Pr) number – the square of the ratio between the viscous and thermal penetration depths
- non-flammable
- convenient and easily attainable (within the United States)

The principle variables of the gas in these devices, and wave propagation in general, are the continuity and momentum equation coupled oscillating acoustic pressure amplitude, p_1, and oscillating volumetric flow rate amplitude, U_1. Through these variables, acoustic power, E_2, is defined as:

$$E_2 = \frac{1}{2}|p_1||U_1|\cos(\phi_{pU}), \tag{2.4}$$

where ϕ_{pU} is the phase angle between p_1 and U_1. It is obvious that greater pressure and volumetric velocity swings will result in more power. This is supported by pressurizing the gas in the engine which effectively increases its acoustic power density while reducing the impact of non-pressure dependent thermal conduction losses in the regenerator [22]. Intuitively this makes sense, but is made obvious by seeing that the oscillating pressure is directly related to the mean pressure, p_m, of the gas:

$$p_1 = -\frac{\gamma \cdot \Delta U_1}{i \cdot \omega \cdot A \cdot \Delta x} \cdot p_m . \tag{2.5}$$

The discussion of thermoacoustic engines often refers to the acoustic pressure amplitude ratio of the internal working gas. This quantity is defined as the percentage of the oscillating acoustic pressure to the mean pressure. As an example, a 10% acoustic pressure amplitude exists if the TAPC has a mean pressure of 450 psig and is producing 45 psig pressure swings.

2.3.1 Standing wave

One version of a thermoacoustic engine is the "standing wave" type, which refers to the acoustic phasing throughout the resonator/engine. Imagine a volume of gas enclosed within a resonator (tube) that is shut on one end and open on the other. If provoked to do so, the sound will bounce back and forth in such a manner that the gas' pressure extremes (antinodes) and velocity zeroes (nodes) will always occur at the hard end of the tube. Intuitively this makes sense because when the gas hits the end wall it has no velocity and feels the most pressure. The opposite is true at the tube's open end; at this point the gas has highest velocity (antinode) and the lowest pressure (node) because it is open to the surrounding atmosphere. The result is always a tube with a longitudinal length equal to one-quarter of the gas' wavelength, λ. This creates an acoustic standing wave, oscillating at frequency ω where pressure is in phase with displacement. In other words, the pressure reaches a maximum or minimum value at the same time that the gas is at an extreme of its oscillation.

If the heat retaining solid plates mentioned in the previous section are grouped to form a matrix of axial paths, relative to the tube, they form what is called a stack. This is basically the piece of aluminum foam in Figure 2.5; another picture is also shown in Figure 2.6. Then, if this stack is put inside a resonator and a steep temperature gradient is forced upon it with a hot and cold heat exchanger, heat will be driven into and out of the gas. This heat exchange provokes the gas to do net work on its surroundings, namely initiate and amplify an acoustic wave.

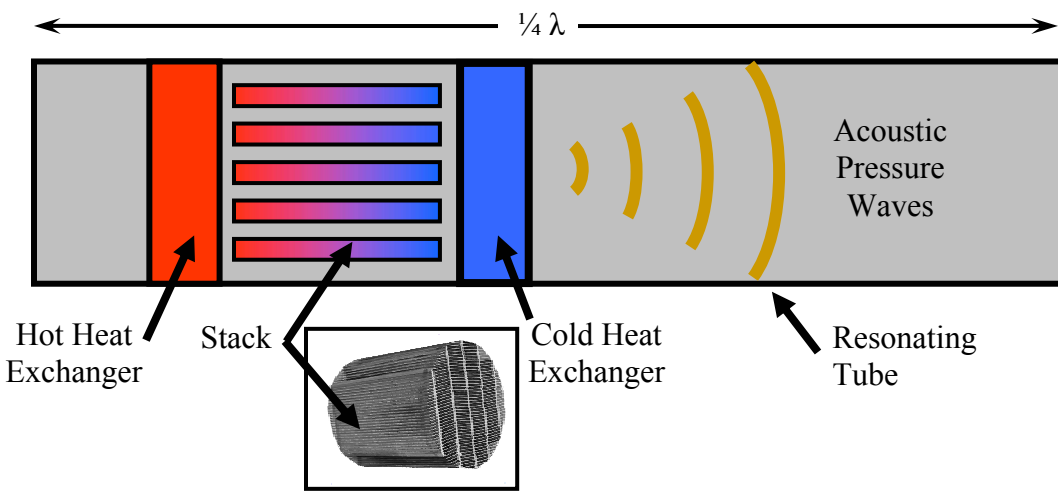

Figure 2.6: Standing wave thermoacoustic engine schematic ¼λ in length. Also shown is a stainless-steel parallel plate stack [18].

Figure 2.7 looks at a single gas parcel as it translates one "displacement amplitude" during half of the acoustic cycle within the stack to help show the source of this thermoacoustic net work, the colors represent the relative temperatures. As a gas parcel oscillates through the stack, it will experience changes in temperature as a result of both an acoustic pressure induced adiabatic compression and expansion and the local temperature of the stack. Specifically, when the parcel is on the hot side, it is cooler than the surrounding stack so it will absorb heat, likewise, when the parcel is on the cold side it is warmer and will reject heat into the stack. Therefore the particle thermally (as a result of temperature) expands while on the hot side and thermally contracts when it is at the cold end.

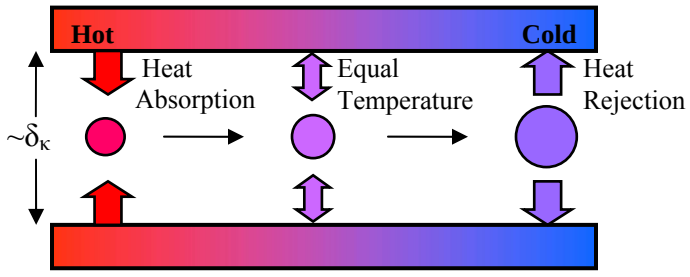

Figure 2.7: Single gas parcel within the stack during "standing wave" displacement towards the cold side.

The standing wave inherent to the closed-opened resonator (Figure 2.6) works in conjunction with these thermal expansions and contractions in order to produce acoustic power. The fact that the hot end of the stack is situated closer to the hard end of the resonator forces it to heat when it is under a higher relative pressure, see the brown lines in Figure 2.8. When the parcel is allowed to cool at the cold end, it is under a lower relative pressure then when it is towards the left, causing a larger gas parcel volume in Figure 2.7. In summary, the thermal expansion of the parcel occurs while the pressure is rising and the thermal contraction occurs when the pressure is falling, and as a result, the gas in the stack pumps acoustic power into the standing wave. This pressure increase is what keeps the volume of the parcel at the hot end small in Figure 2.7 even when it is thermally expanding and the pressure decrease keeps it large at the cold end even when it is thermally contracting. The thermal expansion at high pressure and thermal contraction at low pressure is what develops into an acoustic wave, or more simply, a sound that is resonated by the tube.

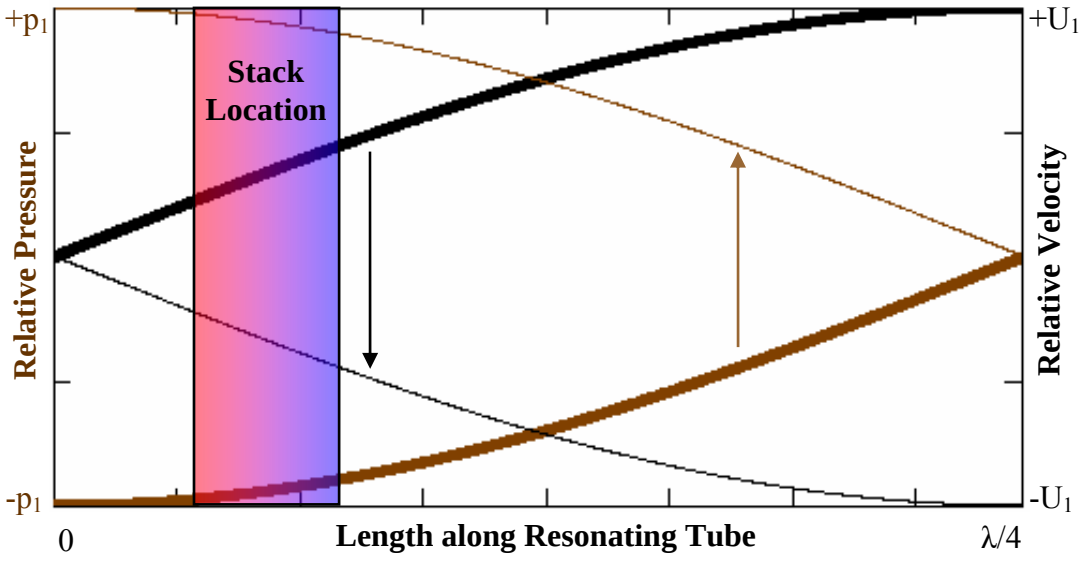

Figure 2.8: Gas pressure distribution within a standing wave resonator that is closed on the left end and opened on the right, so it has length λ/4. The red and blue sides of the stack represent hot and cold. The bold lines are the pressure and velocity distributions within the tube at time zero and the thin lines are the same quantities one-half of the acoustic cycle in time later ($\frac{1}{2}\omega^{-1}$).

The stacks in these standing-wave thermoacoustic engines have gaps similar in magnitude to the gas' thermal penetration depth. At these distances the gas parcels are in good enough thermal contact that they exchange some heat with the stack, but poor enough that there is a necessary time delay between the parcel's motion and heat transfer. This delay is required to enable the thermal expansions and contractions to be in phase with the oscillating pressure and displacement or 90° out of phase with the oscillating velocity. Heat exchange only occurs at the peaks of the gas parcels displacement which causes an inherent irreversibility and thus lower efficiency in standing wave thermoacoustic engines.

2.3.2 Traveling wave - Stirling

Another type of thermoacoustic heat engine is known as the traveling wave or thermoacoustic-Stirling engine. In this version the oscillating gas pressure and velocity are mostly in phase within the heat exchange portion of the engine; this is the same phasing as in a generic Stirling engine [10], hence the name. In theory, this type of phasing results in optimal acoustic power output because the phase angle between the oscillating pressure and volumetric velocity essentially goes to zero, see Equation 2.4.

2.3.2.1 Thermodynamics

Replacing the standing wave's stack in this type of thermoacoustic engine is a regenerative heat exchanger known as the regenerator; this component stores thermal energy during half of the acoustic cycle and returns it during the other half. In contrast to the stack's imperfect thermal contact with the gas, the regenerator in a traveling wave thermoacoustic engine strives for optimal heat exchange between the solid and gas in order to let the thermal expansions and contractions be in phase with the pressure and volumetric velocity oscillations. This level of thermal contact is accomplished by building a stack-like structure with gaps that achieve a hydraulic radius much less than

the thermal penetration depth of the gas. This insures that at every point the gas and regenerator are at essentially the same temperature.

Unlike in the standing wave engine, Figure 2.9 shows through like colors that the regenerator solid and gas parcel are at the same temperature at every point. This causes the gas to move toward the hot side and thermally expand when the pressure is high and likewise it displaces to the cold side and thermally contracts while the pressure is low, resulting in the amplification of acoustic power. The increased acoustic power output is represented by the increased gas parcel volumes in Figure 2.9 versus Figure 2.7.

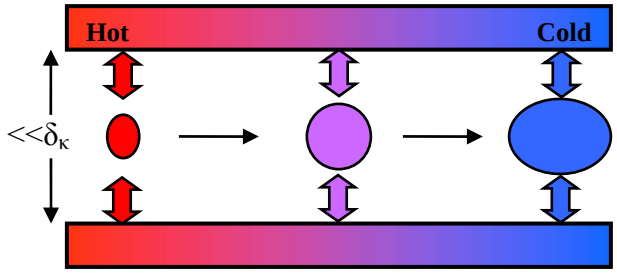

Figure 2.9: Single gas parcel within the regenerator during "traveling-wave" displacement towards the cold side.

The pressure-volume diagram for the Stirling thermodynamic cycle [23] is depicted in Figure 2.10. The steps that the gas parcel undergoes within the regenerator as a traveling acoustic wave propagates through it, starting from the cold end, is summarized in order to qualitatively show the relationship to the Stirling cycle:

a. While nearly stationary at the cold end of the regenerator, the acoustic wave compresses the parcel as it undergoes nearly isothermal compression (the result of excellent thermal contact and high heat capacity).
b. The gas parcel thermally expands as the acoustic wave forces it up the temperature gradient.
c. Nearly stationary at the hot end of the regenerator, the acoustic wave allows the gas to isothermally expand while it absorbs heat during the pressure reduction.

d. Parcel moves towards cold side and returns heat to the regenerator while thermally contracting at low pressure.

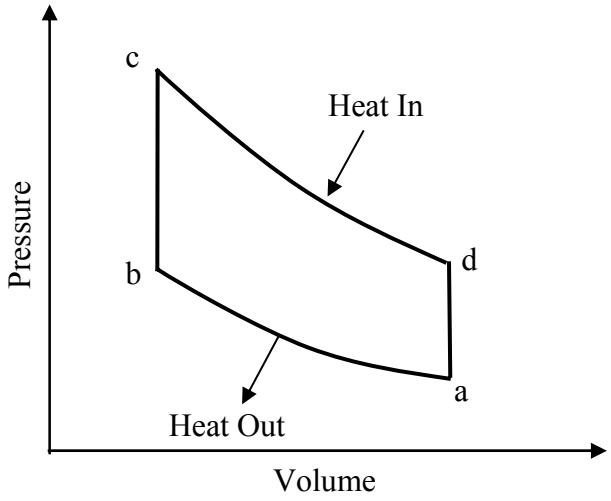

Figure 2.10: Stirling cycle pressure versus volume diagram

2.3.2.2 Acoustic Network

The standing wave type of engine requires only a simple "closed-closed" or "closed-opened" (referring to the resonator ends) with length equal to $\lambda/2$ or $\lambda/4$ respectively. However, in a traveling wave Stirling-thermoacoustic engine acoustic trickery within a torus (doughnut) shaped resonator is necessary [13] to convert the resonator's standing wave into the necessary traveling-wave phasing within the regenerator. This enables the regenerator, with its steep temperature gradient, to thermoacoustically amplify the acoustic power that is fed into the cold end. This amplification gain is related to the absolute temperature ratio, τ, between the hot and cold ends:

$$\tau = \frac{T_h}{T_c}. \tag{2.6}$$

The acoustic trickery is accomplished with an adjoined compact network of channels that have various amounts of compliance, inertance and resistance. These

resonator characteristics are fully developed in Reference [18] but will be summarized here for the sake of completeness. The compliance, C, can be thought of the compressibility of a gas within a certain channel's volume and is defined as:

$$C = \frac{V}{\gamma p_m}. \tag{2.7}$$

The inertance, L, of a gas within a channel describes its inertial (mass-like) properties:

$$L = \frac{\rho_m \Delta x}{A}. \tag{2.8}$$

Finally the acoustic resistance is a result of either oscillating velocity dependent viscosity or pressure dependent thermal relaxation. Specifically the viscous penetration depth along the channel's inside surface causes resistance R_ν:

$$R_\nu = \frac{\mu \pi \Delta x}{A^2 \delta_\nu}. \tag{2.9}$$

The oscillating pressure within each channel causes an oscillating temperature (as in Table 2.1) which develops a thermal relaxation resistance, R_κ, over the total thermal penetration depth volume (surface area multiplied by δ_κ) along the channel:

$$R_\kappa = \frac{2\gamma p_m}{\omega(\gamma - 1) S \delta_\kappa}. \tag{2.10}$$

These resonator characteristics group to form various amounts of an important quantity known as the acoustic impedance, Z, which is defined as the ratio between the pressure and volumetric flow rate amplitudes:

$$Z = \frac{p_1}{U_1}. \tag{2.11}$$

References [13] and [14] detail how the scientists at Los Alamos National Laboratory assembled channels with various amounts of compliance, inertance and resistance to effectively form a torus shaped acoustic network that enabled the advantageous traveling wave phasing within the regenerator [10]. Beyond this phasing issue, the magnitudes of C, L and R were also designed to create high acoustic impedance

(large p_1 relative to U_1) in the regenerator. This is critical to compensate for what would be huge viscous losses [24] (proportional to the square of the oscillating volumetric velocity) in the regenerator because of its numerous torturous paths.

This loss is directly analogous to the power dissipated in an electrical resistor, which is proportional to the square of the current that flows through it [6]. Designers compensate for this in AC electrical power transmission lines by increasing the voltage and decreasing the current. Likewise, the power dissipated in the regenerator is minimized by increasing the pressure and decreasing the volumetric velocity; this is synonymous to maximizing the acoustic impedance, all while keeping power (proportional to pressure multiplied by velocity) constant.

Figure 2.11 depicts a schematic of a Thermoacoustic Stirling heat engine (the addition of the linear alternator makes it represent the entire TAPC). Basically the regenerator amplifies a traveling acoustic wave that in turn pumps acoustic power out of the hot heat exchanger. This power is used to either drive the linear alternator or provide "new" acoustic power to the cold end of the regenerator that is in turn amplified. The acoustic network (specifically between the inertance and compliance) enables the required traveling wave phasing in the regenerator through the following steps [25]:

1. Since the regenerator has high flow resistance, the majority of the pressurized gas moves through the low acoustic impedance Inertance tube at a high acoustic velocity (rather then the parallel regenerator path) into the compliance as the linear alternator moves to the left in Figure 2.11.
2. The flow passing through the parallel inertance and regenerator paths pressurizes the gas in the compliance volume by twice the pressure amplitude, but lags the flow by 90° of time phase.
3. The flow in the inertance tube creates a pressure drop across both it and the regenerator that also forces the pressure oscillation to lag the flow by 90°. This

pressure drop is what drives the flow through the regenerator and enables the pressure oscillation and flow to be in time phase.

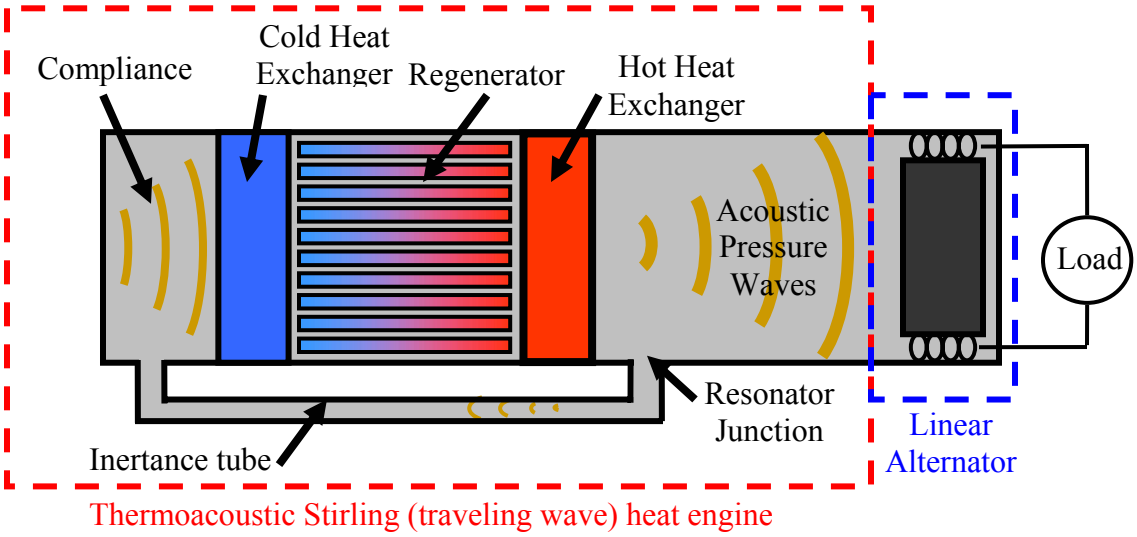

Figure 2.11: TAPC component layout.

Through an electrical analogy, the various components of the traveling wave heat engine can be represented and a first attempt at system optimization and synchronization can be undertaken; see Table 2.2. Specifically the compliance acts as a capacitor, inertance an inductor, regenerator a resistor in series with a τ dependent current source (representative of the thermoacoustic power gain) [10], and the linear alternator acts as an inductive reactance. Reference [13] develops in great detail the integration of these components and how they enable the AC voltage (oscillating pressure) to be in phase with the AC current (oscillating volumetric velocity) within the regenerator. However, as a preference for mechanical systems, the same analogy (somewhat simplified) can be developed in a simple oscillator system [26].

Table 2.2: Network Analogies

Acoustic	Simple Oscillator	AC Electricity
pressure p_1	force	AC voltage
volumetric velocity U_1	velocity	AC current
compliance C	spring	capacitance
inertance L	mass	inductance
resistance R	damper	resistance

The mechanical mass-spring-damper system in Figure 2.12 is representative of the TAPC. The first thing to notice is that the compliance spring and the linear alternator piston mass are intentionally much larger than the other components. This is to signify the fact that the system oscillation frequency, ω, is determined primarily by the resonance condition between the gas in the compliance and the mass of the alternator's piston [13].

The regenerator's temperature profile, τ, amplifies the velocity (and thus power which equals force times velocity) that is driven into the cold end and forced through the regenerator damper. It is also noted that if the magnitude of the inertance mass is small compared to the viscous dependent resistance of the regenerator, then the force and velocity in the regenerator are nearly in phase. This is because the velocity in the inertance is always 90° out of phase from that in the regenerator. In summary, the steep temperature gradient in the regenerator causes the thermoacoustic power gain which can be thought of as a "tickle" that sustains system oscillation by overcoming the electric load on the alternator and any other "natural" losses.

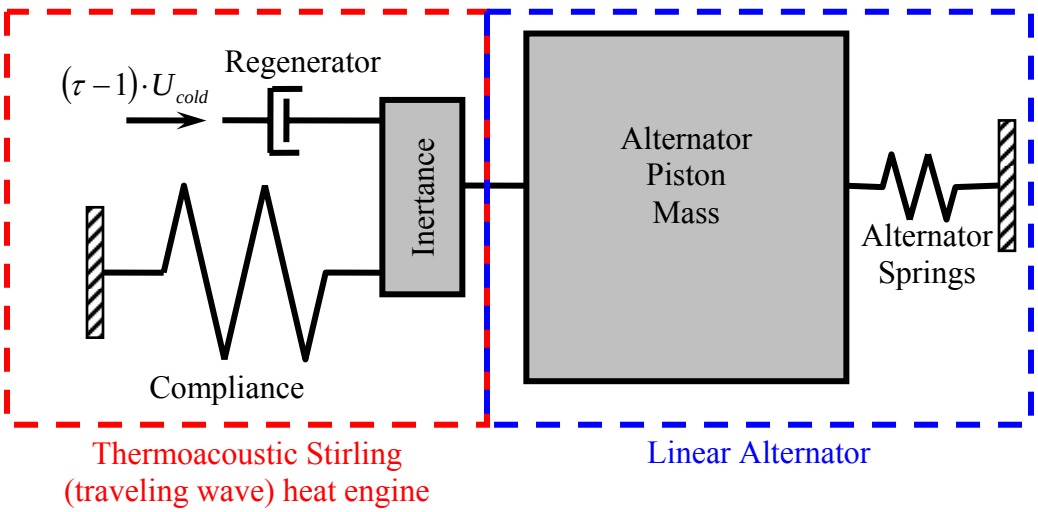

Figure 2.12: TAPC system simple oscillator analogy

2.4 Electroacoustic Power Transducer

The acoustic pressure wave created by the thermoacoustic Stirling heat engine is converted into electricity with an electro-acoustic power transducer, specifically a linear alternator. This device, which can be considered a highly efficient loudspeaker, uses a permanent magnet transduction mechanism for the energy conversion (dynamic to electric). There is a piston-magnet assembly that is held in-line with a set of springs. The acoustic wave cycles this assembly between coils of copper wire and then by Faraday's law and the "BL product" (transduction coefficient), which is the magnetic field multiplied by the length of the wire in the field, an AC voltage is induced at the frequency of oscillation.

CHAPTER 3

DESIGN

The Thermoacoustic Power converter is partly a traveling wave thermoacoustic-Stirling heat engine that is conceptually based on work performed at Los Alamos National Lab (LANL) [13, 14, 27]. Furthermore, because of time constraints, the design embodiment [28] refers to a Northrop Grumman funded effort [1, 15, 29, 30] that joined, for the first time, a scaled one-quarter wavelength LANL traveling wave thermoacoustic-Stirling engine with a pair of alternators in order to produce electricity. Figure 3.1 shows these two engines with their analogous components labeled.

3.1 Clarifying the Design Task

The task of the TAPC design was to demonstrate thermoacoustic energy conversion technology in a unit that could achieve 100 watts of electricity and thus improve upon the 58 watts produced by the referenced work [1]. It was also desired to achieve this power output while maintaining a heat to electric efficiency (η_T) of 20%. Note that this efficiency target is based on a "control volume" that does not include some of the losses due to poor insulation; the method for determining these losses is outlined later. Furthermore, there was no consideration of volumetric nor mass power density so convenience was achieved through the use of heavy and bulky flanges and Swagelok [31] tube fittings. This non-consideration enabled a secondary task of designing the TAPC as a modular device, one that could easily accommodate any re-designed components if deemed necessary during testing.

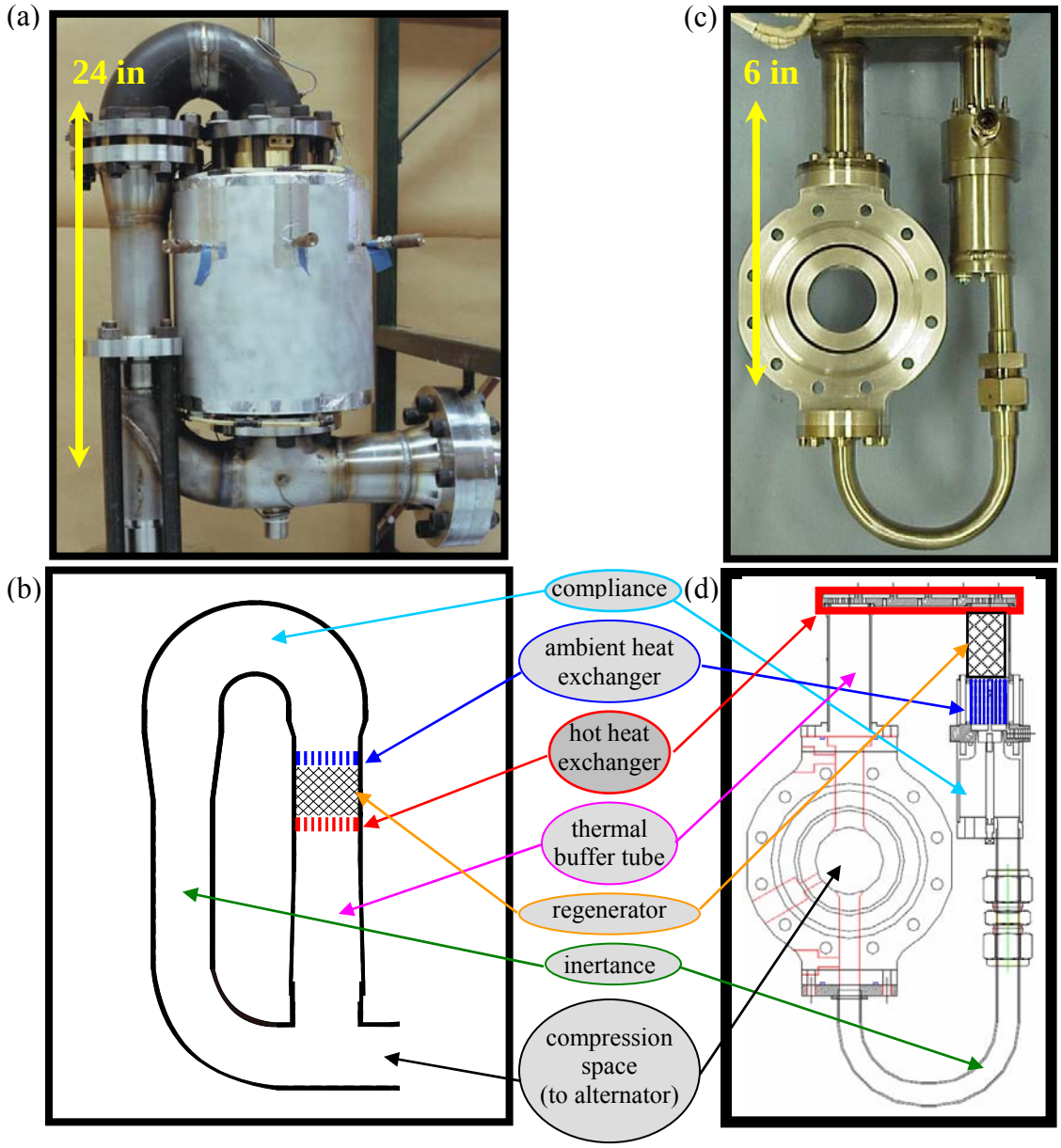

Figure 3.1: Thermoacoustic-Stirling heat engines. (a) LANL 1kW design [13]. (b) Northrop Grumman/LANL design [15]. (c) and (d) are schematics of the engines' internals with their corresponding parts labeled.

3.2 Embodiment Design

Careful consideration must be given to the layout of TAPC components (Figure 2.11) because of the enormous level of vibration that the working gas in a high-amplitude thermoacoustic heat engine is potentially capable of producing [32]. The need to control

this vibration has been understood since the early concepts (Figure 2.1) and demonstrated more recently (Figure 2.4) by joining the linear alternators "end-to-end" in order to achieve vibration cancellation by the fact that the alternator pistons could only cycle in equal and opposite directions. Figure 3.2 below updates Figure 2.11 as a "vibration balanced system."

As mentioned previously, the component layout (inertance tube, regenerator, compliance, etc.) in the TAPC design is like that of the Northrop Grumman work. This was done intentionally to save time by basically skipping the embodiment design and jumping immediately into the detail work. Various views of the final revision of the TAPC model are depicted in Figure 3.3. The two opposed linear alternators are mounted in the pinkish-colored vessels.

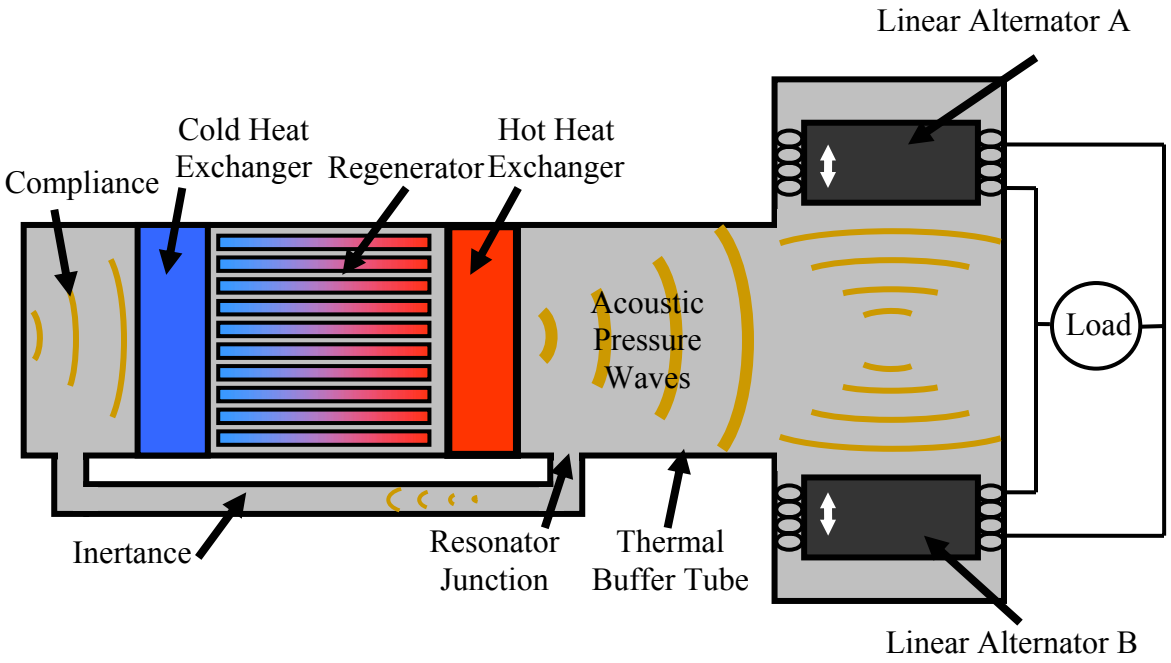

Figure 3.2: TAPC vibration balanced component layout

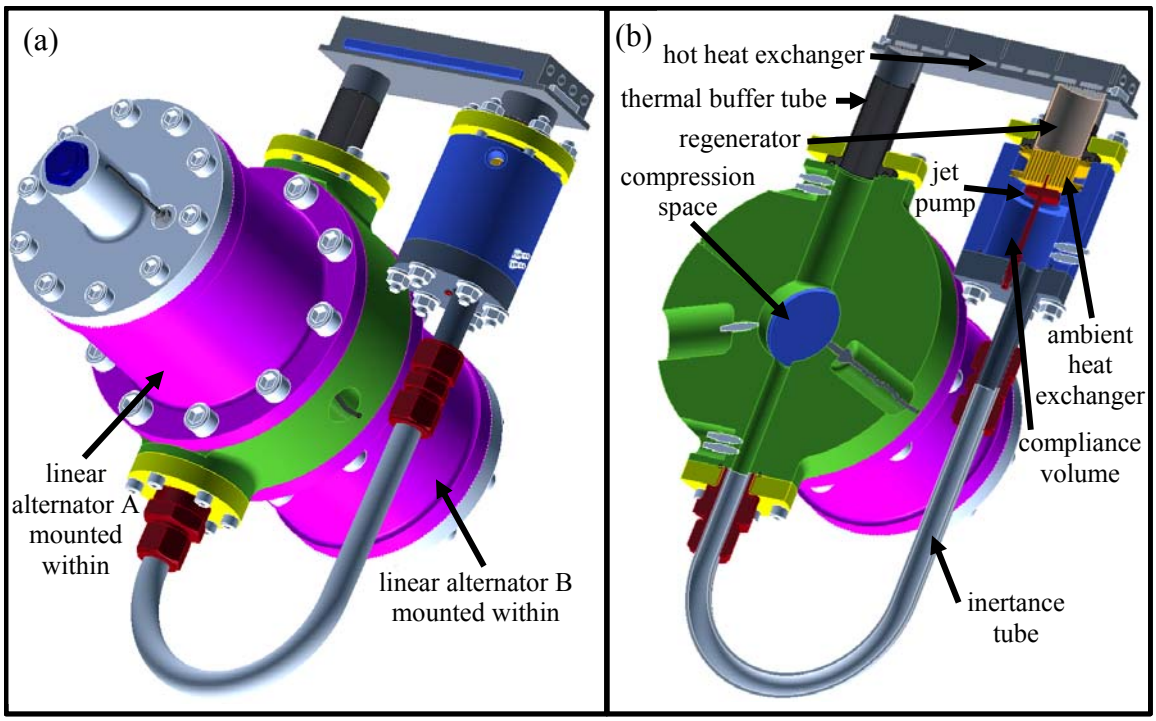

Figure 3.3: TAPC model final revision. (a) isometric view and (b) cross-section.

3.3 Detail Design

After understanding the embodiment, the first part of the detail design was to pick the linear alternators. This approach was taken because these devices are an "off the shelf" component and any engine could be designed to effectively harmonize with them.

3.3.1 Linear Alternators

Through the recommendation and technical support of Dr. Scott Backhaus of LANL [33], *Clever Fellows Innovation Consortium, Inc*. [2], a manufacturer of linear alternators and motors, was identified as a vendor. Technical design discussions began with only an electrical output target of 100 watts at efficiency high enough to realize a TAPC system value of approximately 20% heat to electric. Based on the statistics of the reference engines [1, 14] for heat to acoustic efficiency (η_e) and assuming that an engine

with comparable efficiencies could be realized in the TAPC, an alternator efficiency (η_a) of about 70% was sought, a value that is achievable but not guaranteed.

In order to achieve high efficiency in a linear alternator, both mechanical and electrical resistances are minimized while the mechanical resistance is also designed to be much less than both terms of the alternator's mechanical reactance [18]:

$$X_{mech} = \omega M - \frac{K}{\omega}. \tag{3.1}$$

The M value is the mass of the alternator's piston, the constant K, defines the springs that hold the piston in place (while allowing it to cycle in one dimension) and ω is the angular resonant frequency of the operational TAPC. The CFIC, Inc. alternators easily hit this efficiency design requirement as their mass and spring reactance terms are two and one order of magnitude, respectively, greater than their mechanical resistance.

Alternator efficiency doesn't rest solely on these values; there are in fact other losses that must be considered, like radial clearance gap blow-by, power dissipation (I^2R losses) in the copper coils, thermal losses (hysteresis) in the volume of gas behind the pistons, magnetic losses and mechanical friction [33].

The radial clearance gap is the distance between the alternator's piston outside diameter and the inside surface of the cylinder that it cycles co-axially within; this dimension greatly effects its efficiency. Intuitively, as the dynamic pressure wave of the gas hits the piston, it is easier for it to "squeak" through this radial gap rather than "push" against the alternator and its relatively high mechanical resistance. This reality results in an efficiency drop that basically scales with the square of the gap and obviously, the problem gets worse as the acoustic pressure amplitude increases. Fortunately though, CFIC was able to manufacture alternators with radial piston gaps approaching six tenths (0.0006 inch), a value that could achieve the desired 70% efficiency (η_a).

The other target was to produce a working TAPC capable of producing 100 watts electric, a value that was greatly considered when choosing the appropriate alternator.

The important quantities when designing for power output is the volumetric stroke of the alternator and the engine's acoustic power production, values that basically link the alternator and the thermoacoustic-Stirling heat engine. During operation the thermoacoustic engine cycles a certain volume of gas with inherent pressure and volumetric velocity standing waves. This volumetric stroke is then what impedes the two opposed linear alternator pistons and forces them to move a magnet through their respective copper coils in equal and opposite directions to produce an AC electrical output at the systems resonant frequency. Thus an alternator capable of withstanding the engine's acoustic pressure wave must have a certain piston diameter given its linear stroke and stiffness (function of the piston's mass and the springs that hold it in place). This is because the amount of power stored in the piston's motion is much greater than the amount extracted from the piston [15]. The result was a two inch diameter piston that could stroke (peak to peak) a half-inch, about ± 0.785 in^3 in terms of volumetric stroke. Figure 3.4 shows four pictures of the CFIC, Inc. *1S102M STAR*™ linear alternators purchased for integration within the TAPC.

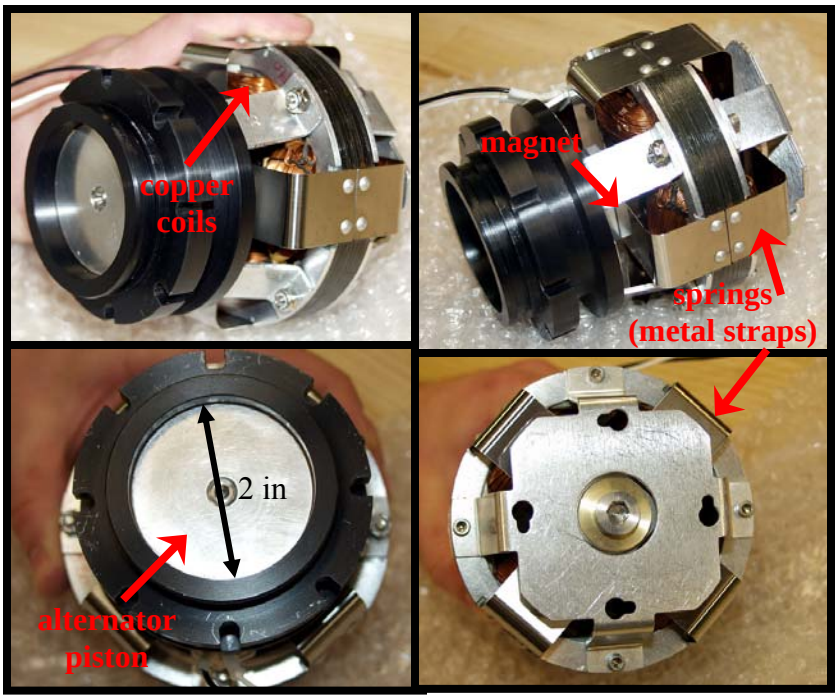

Figure 3.4: Four views of the CFIC, Inc. *1S102M STAR*™ linear alternators [2].

3.3.2 DeltaE Computer Model

Once the specifications for the alternators (piston diameter, electrical and mechanical resistances, transduction coefficient, piston mass, spring constant, allowable stroke and the magnetic field of the stator) were determined, work on the detail design of a harmonizing thermoacoustic-Stirling heat engine could commence. The modeling of the engine was done with a LANL written computer code known as DeltaE (Design Environment for Low-Amplitude ThermoAcoustic Engines) [3,34]. This "first-principles" (low acoustic amplitude) accurate modeling program numerically integrates a one-dimensional wave equation over any geometry with a selected working fluid.

Basically the user defines a geometric configuration of acoustic elements, such as compliance volumes, inertance ducts, electro-acoustic transducers, heat exchangers and regenerators, and the program solves the appropriate 1-D wave equation through each of these "segments." The program does this for the complete "system of segments" by

ensuring that the pressure and volumetric flow rates (both real and imaginary components) are matched at the boundaries of each segment, all while tracking the acoustic power and energy flow between these interfaces.

The computer model of the complete TAPC, referring to Figure 3.3(b), starts at the jet pump (Section 3.3.3.2.5), integrates counter-clockwise through the torus and temporarily ends in the compression space. Integration then starts again at the compliance and travels clockwise until it reaches the compression space junction again, at which point the complex pressure amplitudes between the two integration paths must match up [34]. Next the program splits to one of the two alternators and integrates the wave equation through the radial clearance gap (quoted from CFIC, Inc. as 15 μm which equals 0.0006 in) and pauses. DeltaE now moves the piston its peak stroke displacement with the remaining acoustic power (that didn't leak through the clearance gap) and again matches complex pressure amplitudes with the waiting value from the result through the gap. This piston motion induces the electrical wattage output based on the electro-magnetic specifications of the alternator. At this point the program integrates the wave equation over the volume of gas behind the alternator and ends. Given the alternator specifications, DeltaE can return acoustic and electric power outputs (for the one alternator it analyzed); efficiency can than be calculated using the DeltaE determined heat input necessary to support oscillation at a targeted acoustic amplitude.

The DeltaE input/output file for the TAPC, which was fully integrated with the support of Dr. Backhaus [25], is found in Appendix A. This model provided good insight to inner-geometries of every component and worked in conjunction with the details of the pressure vessel analysis (design under the guidelines of Reference [4]), system integration and the relative component tolerancing to develop "machine shop worthy" drawings. The model ignored a few "secondary" areas of acoustic dissipation (like flow straightening copper screens or heat related power dissipation in the copper coils) so it was accepted that the output numbers were probably not within the full capabilities of

DeltaE predictions. However, the model allowed a scoping of component geometries and resulted in final TAPC model predictions of 170 watts acoustic power, 120 watts electric power, and a system efficiency (η_T) of 22% at its full capability which means maximum alternator piston stroke and a 10% acoustic pressure amplitude. Acoustic pressures at these magnitudes have exhibited optimal performance without suffering non-linear thermoacoustic characteristics.

3.3.3 TAPC Engine

The engine portion of the TAPC is essentially a looped (torus-shaped) flow path that forces the helium, at 450 psig internal mean pressure, to execute the Stirling cycle within the regenerator [13]. The entire loop is basically a ¼ wavelength resonator configured in such a way that the regenerator is placed near the velocity node (pressure antinode) in order to minimize velocity dependent viscous losses. It is noteworthy that the engine has no moving parts, so the complete design, as developed in the DeltaE model, is solely based on the internal geometries and surface finishes of the set of components that make up the loop. The drawings of the TAPC are shown in Figure 3.5 to assist in the following discussion of the design details.

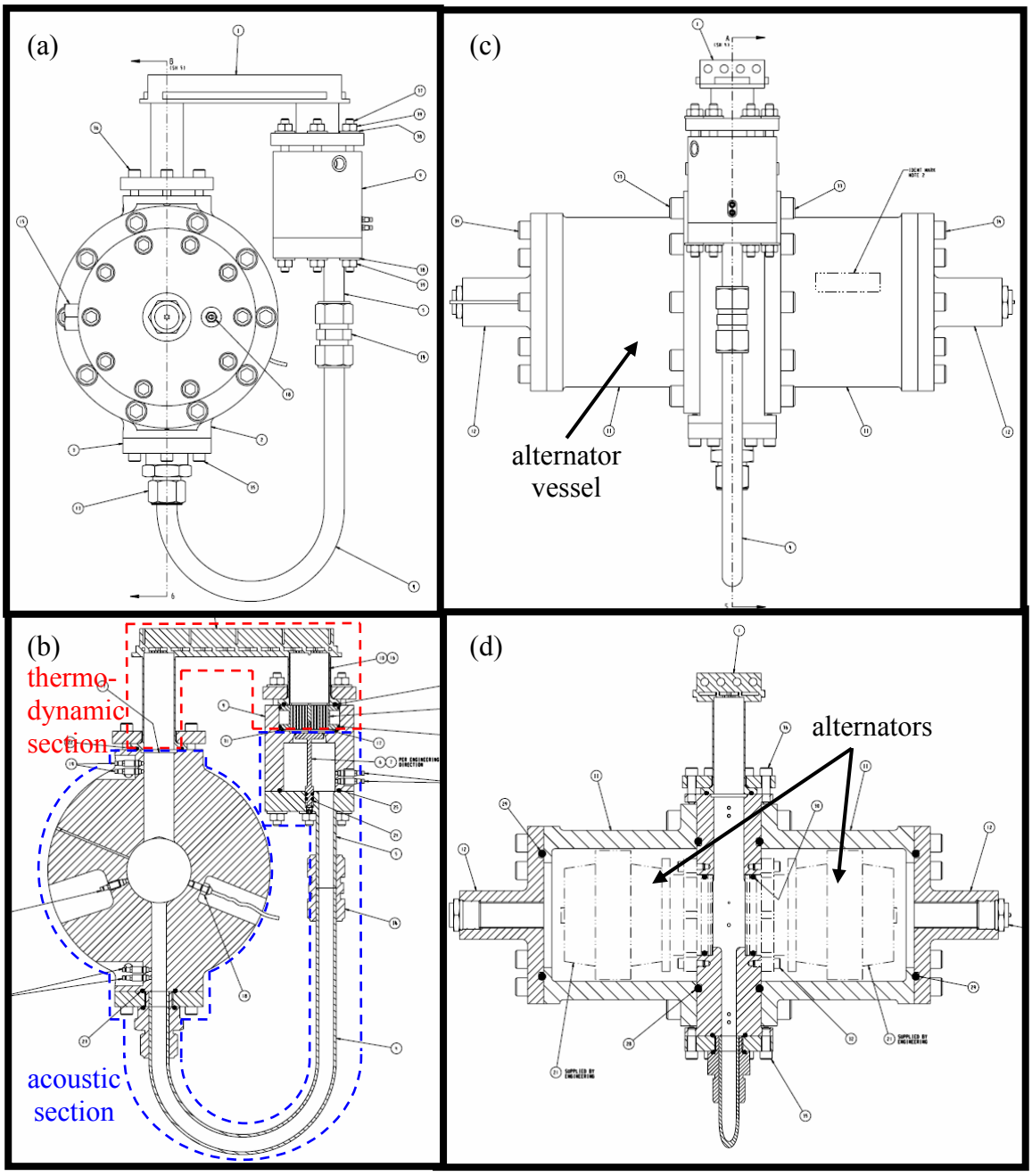

Figure 3.5: TAPC drawings: (a) front view and (b) cross-section, (c) side view and (d) cross-section

3.3.3.1 Thermodynamic Section

The Ambient Heat Exchanger, Regenerator, Hot Heat Exchanger and the Thermal Buffer Tube components make up the thermodynamic section of the engine, see Figure 3.5(b). This section is subjected to high temperatures (~1200°F) at the hot heat exchanger and ambient temperatures at the borders to the Acoustic Section (Section 3.3.3.2). Thus each component subjected to the heat must be able to withstand the temperature and/or the steep temperature gradient without losing strength at the operating internal pressures and without recklessly conducting away heat; this would result in an unwanted efficiency loss.

These components, minus the Ambient Heat Exchanger, were manufactured out of a nickel based alloy - Inconel 625 (UNS N06625, ASME SB-446, Grade 2 - Solution Annealed) for a variety of reasons. The first of which being the fact that this nickel-chromium-molybdenum alloy has very high strength at elevated temperatures (the allowable stress values are in Table B.5). The second reason is its very low thermal conductivity [23], about three times less than stainless steel. This avoids performance and efficiency loss through what would be massive heat leaks down the vessel's walls away from the hot heat exchanger. Thirdly are the thermal expansion characteristics which are about 20% better than stainless steel at any temperature. Finally was the fact that this material was readily available, albeit Grade 1, it was easily heat treated to achieve Grade 2 characteristics (see Section B.2).

The Hot Heat Exchanger was machined with two weld prepped tubes that were later welded to matching lap joint stubs after a slip-on loose type flange was slid on [35]. The resulting tube-like features make up the Thermal Buffer Tube and Regenerator housing, as is depicted in Figure 3.6. It is noted that all of these tube-like features were initially machined with a wall thickness twice the final dimension desired; this extra material served as a "weld backing." After the welding, these features were bored on an upright milling machine to a final wall thickness of 0.035 inches for both the Thermal

Buffer Tube and Regenerator tube features, as is shown in Figure 3.6(f) and is analyzed in Appendix B.4.4. It was vital to keep these pressure vessel walls thin in order to prevent the undesired heat leaks down the wall and away from the Hot Heat Exchanger that were previously mentioned.

The upright milling machine configuration enabled easy access; however it resulted in a long and tedious process. Firstly, the High Speed Steel boring tool could only remove a few thousandths of an inch (radial dimension) per pass because it was feared that the torque on the thin wall would cause it to tear. The result was multiple shallow cuts which were not beyond the "work-hardened" thickness. This made it necessary to sharpen the tool after almost every pass, obviously increasing the overall machine time. Another problem was that the chips found their way through the 0.060 inch inlet holes and into the welded shut Hot Heat Exchanger (HHX). This was anticipated, so a layer of wax that could later be melted out was pressed into every hole. However, this attempt at plugging the holes turned out to serve little good as the wax seemed to melt away after the first boring pass and many chips fell inside the HHX. Prior to assembly some of these chips were pulled out with a needle while others were removed in the ultrasonic bath. However it wasn't until the component was heated up that the chips eventually shriveled and could be blown out.

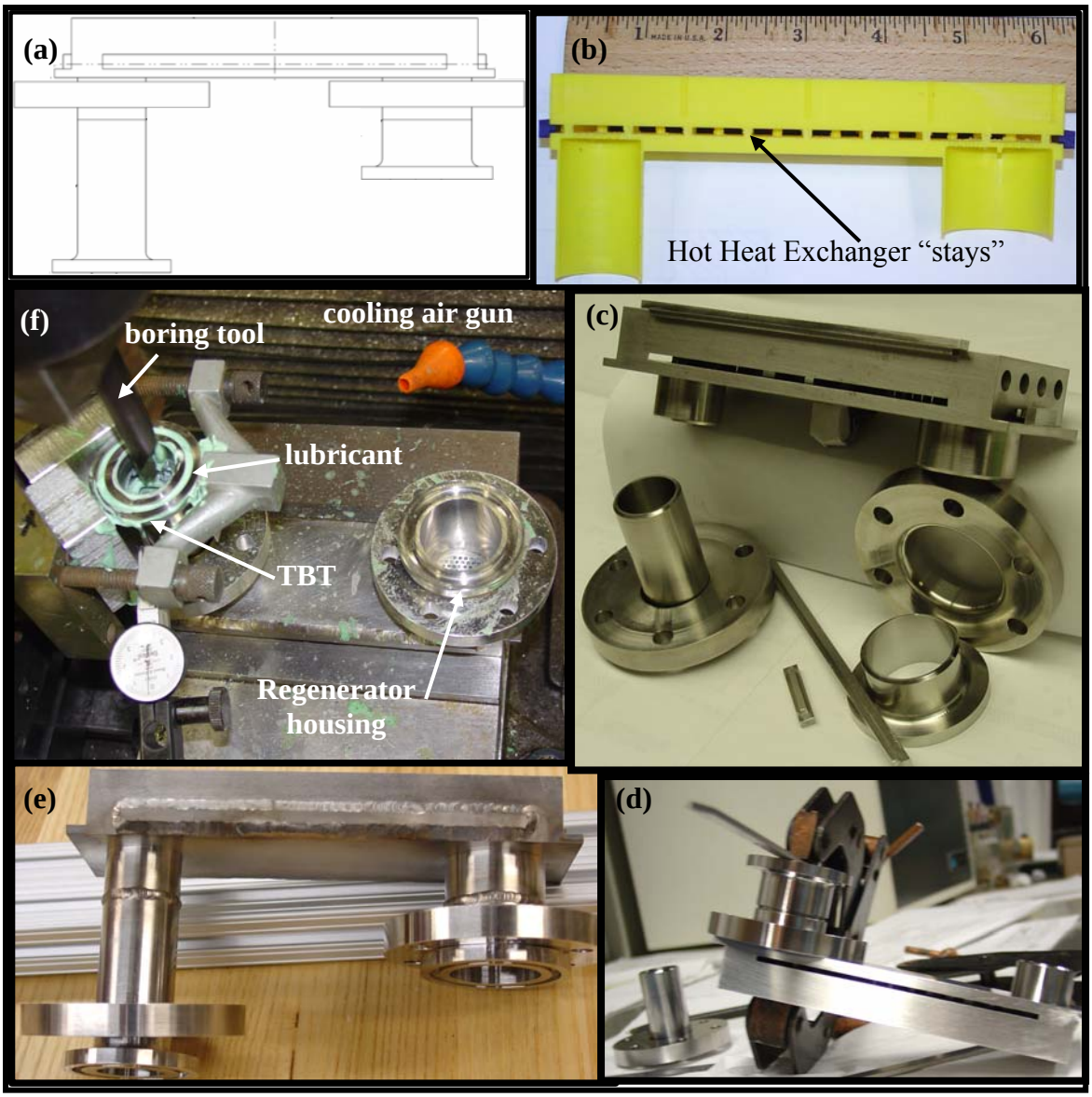

Figure 3.6: Thermodynamic Section. (a) Assembly drawing. (b) Full-scale cross-section plastic rapid-prototype model used to assist discussions with the machinist. The "integral stays," thin tube walls, Regenerator side central "post" and the blue plugs to be fillet welded are shown. (c) Individual components prior to weld. (d) Ready for first spot weld tack on Regenerator housing. (e) Ready for final assembly. (f) Post-weld inside diameter bore in a milling machine.

3.3.3.1.1 Hot Heat Exchanger (HHX)

Heat enters the system through four one-quarter inch diameter cartridge heaters [36] that are imbedded in the upper portion of the hot heat exchanger, as depicted in

Figure 3.8(a); each is capable of outputting 400 watts of heat. Subsequently, the heat conducts through the Inconel and brings the gas, internal to component, to the 1200°F operating temperature. It is noted that even though the TAPC was expected to operate with approximately 475 watts (see the DeltaE model in Appendix A) of heat input, four electric cartridge heaters were run in parallel in order to enable even heating and prevent the inevitable burn-out of overtaxed heaters.

Simple static conduction problems were solved in order to ensure that the heat at the cartridge heaters would reach the internal gas boundary. This heat transfer issue was also modeled dynamically with Abaqus "finite element analysis" software [37] by applying heat at the location of the cartridge heaters and forcing helium through the internal gas region [38], see Figure 3.7. It is noted that the gas motion in the Abaqus model was not cyclic, but using the TAPC's operating frequency (DeltaE determined it to be approximately 100 Hz) and the HHX's cross-sectional internal gas dimensions, the maximum flow rate at the peaks of the volumetric velocity oscillation was determined and applied to the flowing Helium in the Abaqus model. It was assumed that if enough heat at the solid-gas boundary could convect into the Helium at this maximum DC flowrate, then there would be no issue with the actual cyclic gas velocity.

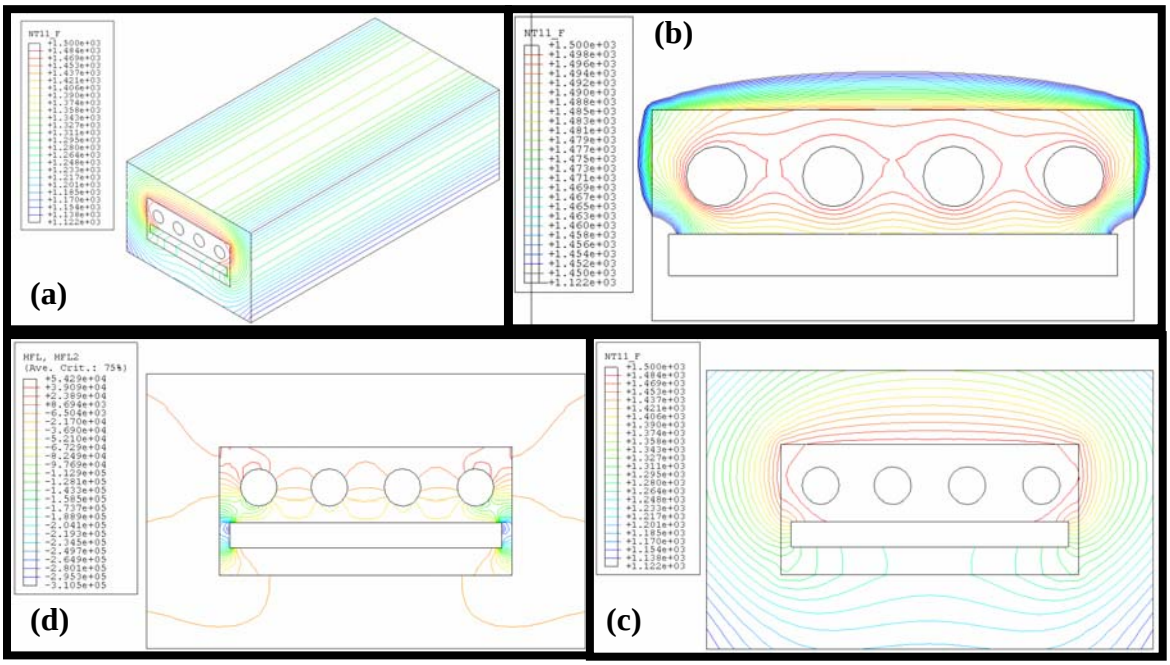

Figure 3.7: Computer model of helium flowing through the Hot Heat Exchanger rectangular duct as heat is applied to the four cartridge heater holes. The temperature gradients in degrees Fahrenheit are shown in (a), (b) and (c) with arbitrary insulation surrounding the component. The heat flux is in (d).

The length of the HHX was dimensioned to span one "gas displacement amplitude," ξ. Thus at the optimal 10% acoustic pressure ratio operation, a gas molecule bordering the Regenerator shuttles to the Thermal Buffer Tube and back again during every period of oscillation. Introduced in Section 2.2, this is the optimal heat exchanger dimension (parallel to the gas motion) because at greater lengths the gas molecules never reach certain portions of the heat exchanger, wasting heat, and at shorter lengths the gas molecule will travel into unheated segments during portions of the cycle and cool prematurely. This dimension of six inches was determined with the DeltaE model.

Great care was devoted to designing this portion of the thermodynamic section because it is subjected to hot temperatures and high internal pressure. Thus, in order for it to be rectangular and allow correspondingly easy heat input from the cartridge heaters, it was designed with a series of "stays" that prevent the thin bottom plate from bowing

outward under the mean 450 psig internal pressure. Basically a stay is a "rib" of material or bolt that is attached to opposing internal sides of a pressure vessel and prevents it from exploding or collapsing during internal or external pressurization, respectively. Normally these stays are either bolted or welded in place, as Reference [4] specifies and Section B.4.1 uses for analyses. In fact the earliest set of drawings for the TAPC had a HHX based on this "welded stay construction." However, the welding would've been quite difficult, so it was determined early on to design the HHX in order to simplify the required welding. This resulted in an expensive to machine, but cheap to weld final design.

The gas flow paths were machined into a single block of the Grade 2 Inconel 625 with a process known as Electro-Discharge Machining (EDM). Shown in the cross-sectional view of Figure B.5, multiple perpendicular passages of the EDM process resulted in a "checkerboard" of ribs, i.e. "integral to the component" stays, which enabled internal pressurization. After these flow paths were completed the four remaining slots that the EDM process used for access into the center of the HHX were plugged with parts machined out of the same material and then fillet welded into place (Appendix B.4.3)

Electro-discharge machining is a process in which a conductive workpiece is machined by electric sparks that travel through a dielectric fluid from a "cutting tool." This tool, which serves as the electrode, can be either a thin wire (usually copper, tungsten or molybdenum) in the wire EDM process or a pre-machined tool (usually graphite or brass) that is a replica of the material to be removed in the plunge EDM version [39]. The machining of the HHX flow paths began by drilling small holes through each of the perpendicular passages, the wire was then fed through these holes one at a time, and finally the wire EDM machine moved the wire through a pre-programmed rectangular shape burning away material as it translated.

Obvious in Figure B.5, the plunge EDM process was used in the corners where a wire could not be thread all the way through the workpiece. This version was only used

for these few instances because the pre-shaped tool electrode burns away the material in a very slow repetitive pecking manner, in fact it took three hours to burn through a two inch span. It is noted that these corners provided two benefits: they minimized areas internal to the HHX that the oscillating gas flow would not readily access during operation and they also provided a region of thick backing material for the eventual fillet welding of the four plugs.

The EDM process proved ideal for these complicated features; however, the high voltage at the cutting surface left a recast layer which is basically a change in the material property because of the high heat. This layer (a few thousandths of an inch thick) would be a problem in the HHX because it greatly inhibits heat transfer. It can be chemically dissolved in a "pickling" process, however, it was determined that a non recast layer forming low-voltage "skimming" final cut with the wire EDM would be sufficient.

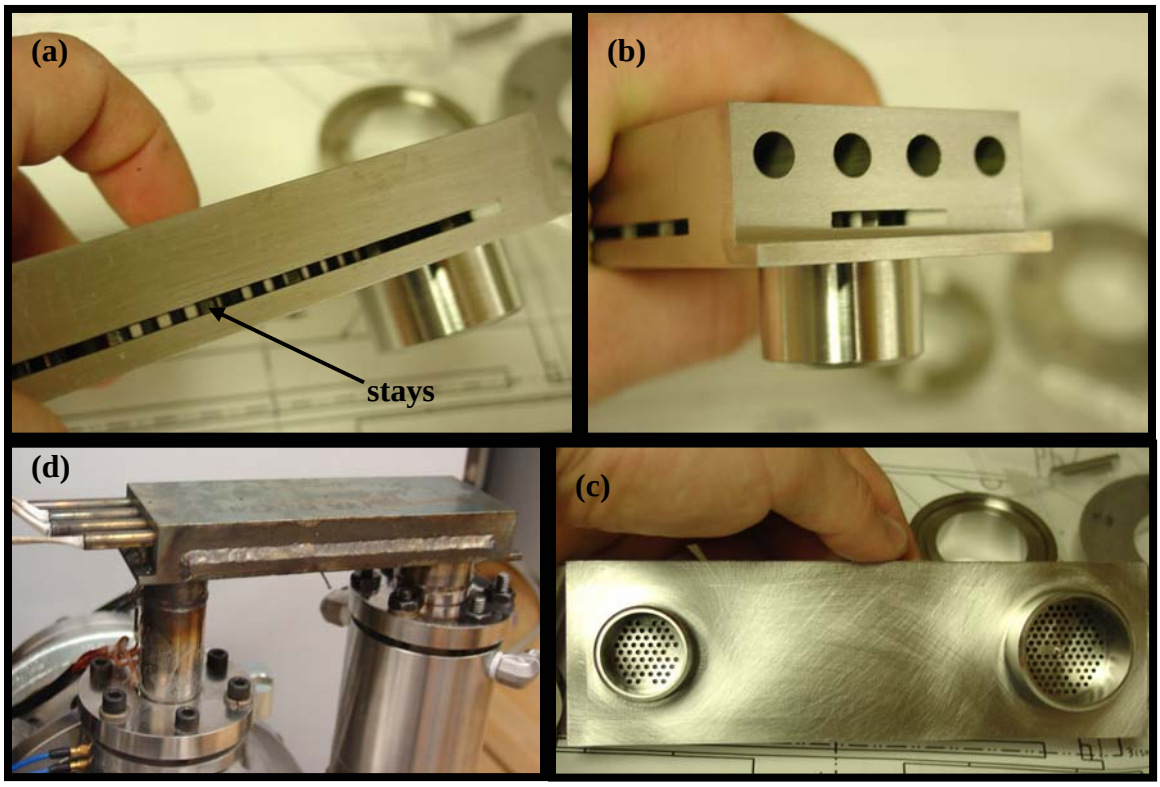

Figure 3.8: Hot Heat Exchanger. Views of gas flow path in (a) and (b). (c) Outlets to Thermal Buffer Tube and Regenerator. (d) Insertion of cartridge heaters.

3.3.3.1.2 Regenerator

One inlet to the HHX is the regenerator which is made up of a stack of 419 Type 304-stainless steel screens, measuring 1.565 inches in height. The chosen mesh for these screens was 180 wires per inch (0.0018 wire diameter) which has the appropriate porosity, Φ, to achieve the required (Section 2.3.2.1) small hydraulic radius, $r_{h,}$:

$$\Phi = 1 - \frac{\pi \cdot n \cdot D_{wire}}{4}, \tag{3.2}$$

$$r_h = D_{wire} \frac{\Phi}{4(1-\Phi)}, \tag{3.3}$$

where n is the mesh number in wires per inch [40]. Based on the dimensions from the wire mesh manufacturer [41], these equations resulted in a porosity of 0.75 and a hydraulic radius of 1.3 thousandths of an inch which is much smaller than the thermal penetration depth of the helium in the regenerator. In fact, this depth ranges from 10 to 14 thousandths of an inch from the cold to hot ends respectively, basically an order of magnitude greater than the hydraulic radius, enabling the excellent thermal contact between the solid screen and helium within the regenerator.

The screens were cut to 1.202 inch diameter circles with the wire EDM process. One lesson learned is that the EDM water bath (the dielectric fluid) should be cleaned prior to cutting the fine mesh screens because metal chips from previous EDM jobs will find their way into the screens' pores. In order to rid the screens of these chips, the entire lot went through a series of ultrasonic cleanings in a solution of an anionic detergent [42] and water. They were then air dried, as is depicted in Figure 3.9(b).

Also shown in Figure 3.9, the screens were randomly stacked into a thin-walled Type 304 stainless steel "screen canister" that enabled easy installation and removal. During installation this canister was slid into the appropriate tube feature of the Thermodynamic Section and under the event that the fit was too tight, there is a "lip" feature at the bottom of the canister that can be hooked for easy removal.

Depicted in Figure 3.9(c), another feature of the Regenerator region was a small 0.062 inch long central "post" of material left on the interface to the HHX. This post ensures that the screens will not rest against the holes that make up the entrance to the HHX, allowing a necessary gas mixing region [33]. The diameter of this HHX entrance is the same as the Regenerator; however, the 115 holes amount to only 29% of the Regenerator's cross-sectional area. If the Regenerator screens were pressed tightly against these holes, only 29% of the first few layers of screen would have been able to carry the volumetric velocity. This would result in a high viscous dissipation of acoustic power at this point [18]. It is also noted that the gap that results from the post of material cannot be too large because the region would essentially act like two independent isothermal surfaces with limited heat transfer between them. The 0.062 inch gap chosen is similar to a gap used in Reference [13].

Based on the total weight of screens in the canister and the density of Type 316 stainless steel, the real experimental screen porosity was determined to be 0.76. Equation 3.2 was then used to find a corresponding hydraulic radius of 1.4 thousandths of an inch, a value that is negligibly different from the above quoted design values used in the DeltaE model.

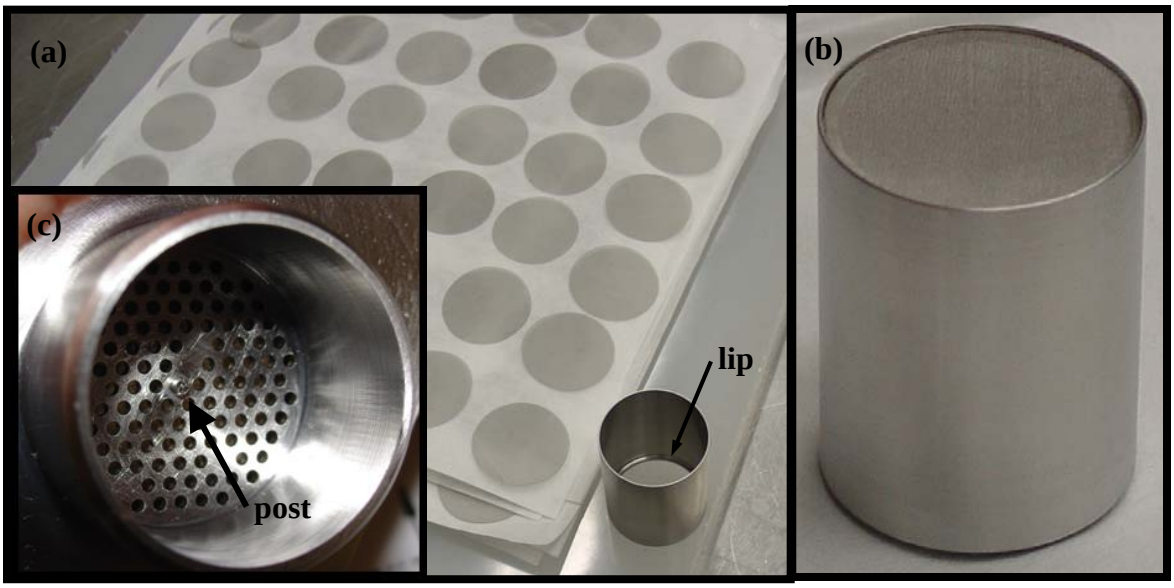

Figure 3.9: Regenerator hardware. (a) Empty screen canister ready to be filled with 419 cleaned 1.202 inch diameter 180 mesh screens. (b) Assembled stack 1.565 inches tall. (c) Looking into HHX from Regenerator housing prior to Thermodynamic Section welding.

3.3.3.1.3 Thermal Buffer Tube (TBT)

The Thermal Buffer Tube is a 0.868 inch inside diameter 3 inch long cylinder that thermally buffers the alternator from the HHX while allowing acoustic power to flow away from the HHX. This inside diameter is much larger than the thermal penetration depth, so there is minimal heat transfer between the solid wall and oscillating gas. Thus from an acoustical point of view, the TBT acts solely as a compliance volume. It was also necessary to have an inside surface finish less than the thermal and viscous penetration depths; the final boring process actually achieved a surface finish value about three orders of magnitude smaller at 32 micro-inches.

The length of the TBT should be several peak-to-peak gas displacement amplitudes long. However, final TAPC component integration constrained this to the three inch length, a value that the DeltaE model calculates to be only two amplitudes long. Reference [18] recommends that the TBT length should be greater than two

amplitudes if thermal isolation is to be maintained between the HHX and alternators, it has also been stated that roughly six amplitudes are required for good insulation [43].

It was already stated that a thin TBT pressure vessel wall is required to prevent large conduction heat leaks; it is also crucial to avoid large convective heat leaks within the flowing helium that result from non-uniform flow across the TBT's cross-section. There is a flow straightener made up of three layers of 22 wires per inch copper mesh screen secured at the bottom of the TBT. This small stack was made out of high conductivity copper screen to act as a heat exchanger, which is another barrier to prevent the hot helium from reaching the alternators. However, these flow straightening screens were omitted at the sharp 90° HHX-TBT junction because it is difficult to secure them in place.

3.3.3.1.4 Ambient Heat Exchanger (AHX)

The Ambient Heat Exchanger is situated below the Regenerator and functions as a means to keep the cold end of it at ambient temperature (around 100°F). It is a basically a cylinder of OFHC (oxygen free high conductivity, UNS. No. C10200, ASTM B152) copper with 126, 0.062 inch diameter holes drilled through it. This type of copper was chosen in order to maximize the effectiveness of the heat exchange between water flowing around the outside of the AHX and the helium oscillating within its holes, see Figure 3.10. It actually has a thermal conductivity about two, ten and forty times better than aluminum, stainless steel and Inconel respectively [23], making it the obvious material of choice.

Shown in Figure 3.10, the number of holes was optimized for the given cross-section (function of the Regenerator's diameter) by laying them out in a hexagon shape, analogous to the "face-centered" packing studied in undergraduate chemistry [44]. The waste heat rejected by the TAPC is then carried away by a stream of water flowing around the outside hexagon "ring" of holes. The outside perimeter that borders the water

was cut with a matching hexagon cross-section, rather than circular, in order to minimize and make constant the amount of copper between the outside ring of gas holes and water; another means of optimizing the heat exchange. The thickness of this copper ligament wall between the internal pressurized helium and low pressure water jacket is analyzed in Appendix B.4.6.

As in the Regenerator's border to the HHX, there is another central "post" on the top side AHX in order to keep that same gap discussed in Section 3.3.3.1.2. This feature functions just like the post on the HHX, it allows the gas to mix as it cycles between the Regenerator screens and the 66% smaller in cross-sectional flow area AHX. One final feature is a stack of two 24 wires per inch copper mesh screens situated below the AHX that break up the flow jets coming out of its holes.

Figure 3.10 also shows the multiple radial o-rings that were used to seal both the water and internal gas volumes. There is also an axial o-ring groove machined into the mating surface of the Compliance component. This seal is not needed, but serves as an extra guarantee of seal for the adjacent radial o-ring groove. It is noted that all o-rings were lubricated with vacuum grease during assembly.

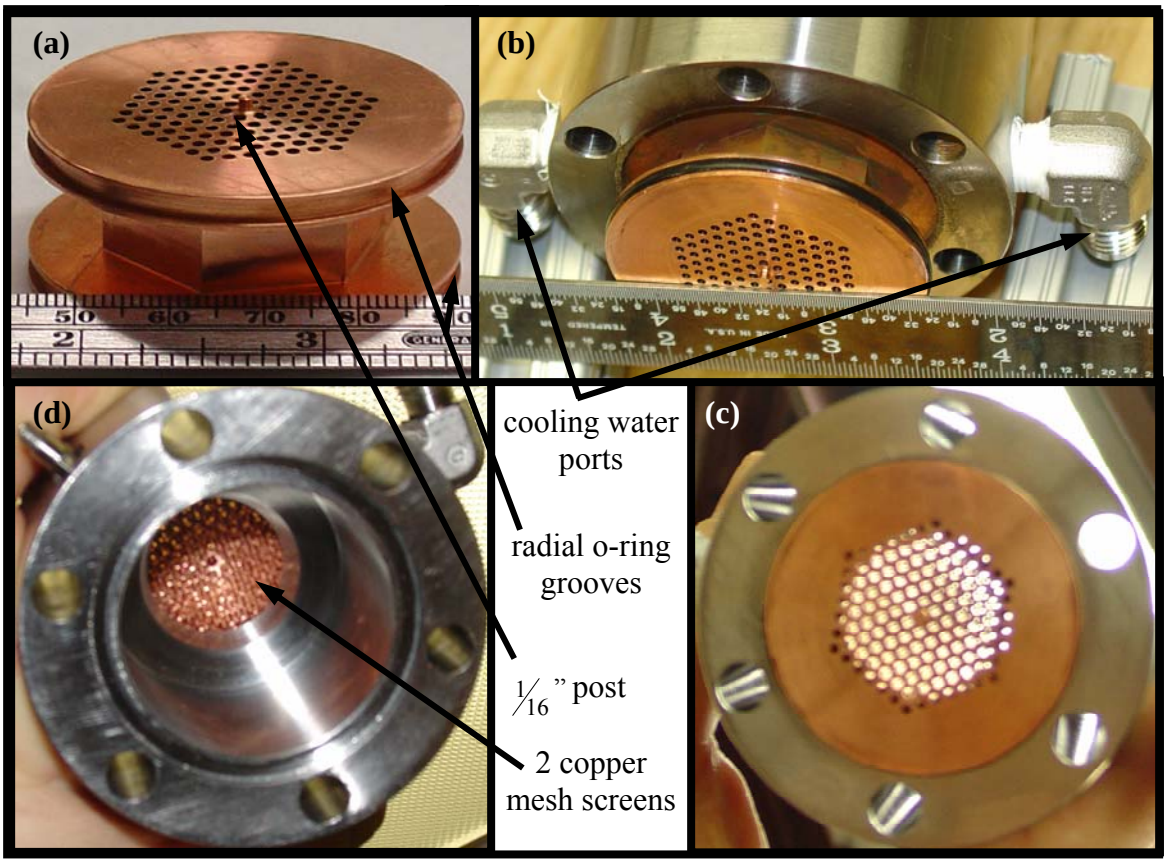

Figure 3.10: Ambient Heat Exchanger. (a) Prior to assembly. (b) During assembly, shows configuration of "water jacket" with respect to the inlet and outlet ports. (c) Looking down from Regenerator side. (d) View from Compliance volume.

3.3.3.2 Acoustic Section

Below the thermodynamic section lays the acoustic section, Figure 3.5, which is basically made up of a compliance volume below the AHX and an inertance tube that connects this volume to the TBT. This network of components is critical to forcing the in-phase traveling wave pressure and velocity oscillations within the Regenerator [13].

3.3.3.2.1 Compliance

The Compliance chamber is simply an open volume of approximately 3 in^3. Depicted in Figure 3.11, this 1.5 inch long and 1.6 inch diameter polished internal space lies within the same stainless steel component as the AHX.

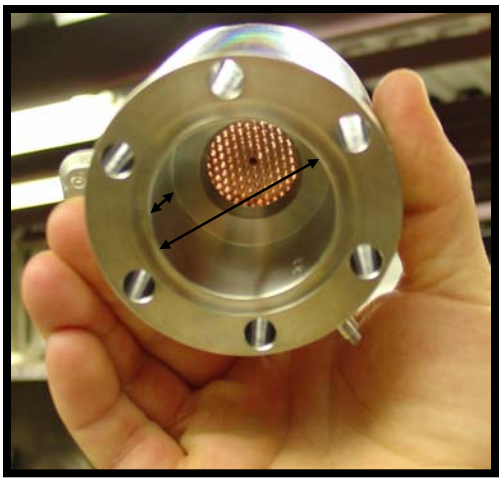

Figure 3.11: The empty space with the diameter and length shown makes up the Compliance Volume.

3.3.3.2.2 Feedback Inertance Tube

The Feedback Inertance Tube enables acoustic power to be fedback into the ambient end of the regenerator. It is a stock 0.625 inch seamless Type 304 stainless steel (UNS S30400, ASTM A269) [45] tubing about 18 inches long (including the 180° bend). The first few inches of this tube (below the Compliance) was machined into the stainless steel Compliance flange with the same wall thickness and inside diameter as the stock tubing. It was then connected to the rest of the inertance tube with a "bored-thru" tube fitting union. Normally these fittings have a "step" in the central portion that the two tubes rest against during the Swagelok [31] union process. Thus in the normal tube fitting union there would be two steps that the gas would travel past during operation. In order to minimize this to one potentially gas motion inhibiting step, the union used was "bored-thru" so that the ends of the two tubes would rest against each other rather than against a step in the normal union. The other end of the tube is connected to a flange with a Swagelok® male straight thread O-seal tube fitting. The bored-thru version of this fitting was used for the same reason as the bored-thru union previously described.

Another feature of the Inertance tube is the entry into the Compliance volume which has a radius in order to avoid flow separation. This radius was limited to a value of 0.62 inches because of the o-ring groove that seals the Compliance flange against the Compliance region. However to avoid flow separation, a lip radius to hole diameter ratio greater than 15% is desired [46], in this instance a 14% ratio is attained. One final feature of the Inertance tube is its inside surface which was polished to a 32 micro-inch finish to minimize viscous losses during high acoustic amplitudes, that is to say high volumetric velocity operation.

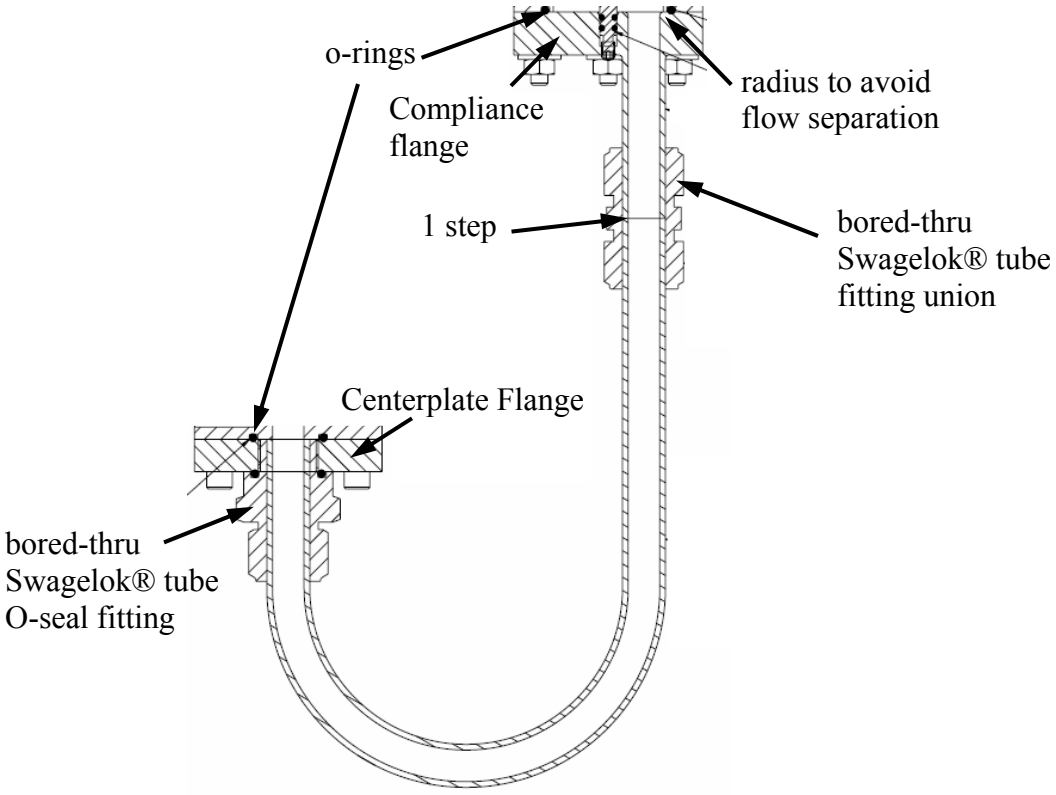

Figure 3.12: Inertance Tube.

3.3.3.2.3 Centerplate

The two geometrically opposed linear alternators are mounted on a large double sided flange termed the Centerplate. Internal to this component are two identical in length and different in diameter bores that connect the TBT and Inertance tube to the compression space, which is the volume of gas in between the two alternator pistons. The Centerplate is machined out of Type 304 stainless steel (UNS S30400, ASTM A240), as is all parts not in the thermodynamic section.

Seen in the Figure 3.13 pictures, this component has multiple sets of o-ring grooves and bolt circles in order to connect and seal with the various other parts. As in the Compliance flange, there are 0.125 inch radii to prevent flow separation [46] of the gas that oscillates in between the compression space and the bores that connect to either the TBT or the Inertance tube. The copper wire mesh that serves as a flow straightener and secondary heat exchanger, discussed in Section 3.3.3.1.3, are mounted in the ledge seen in Figure 3.13(f).

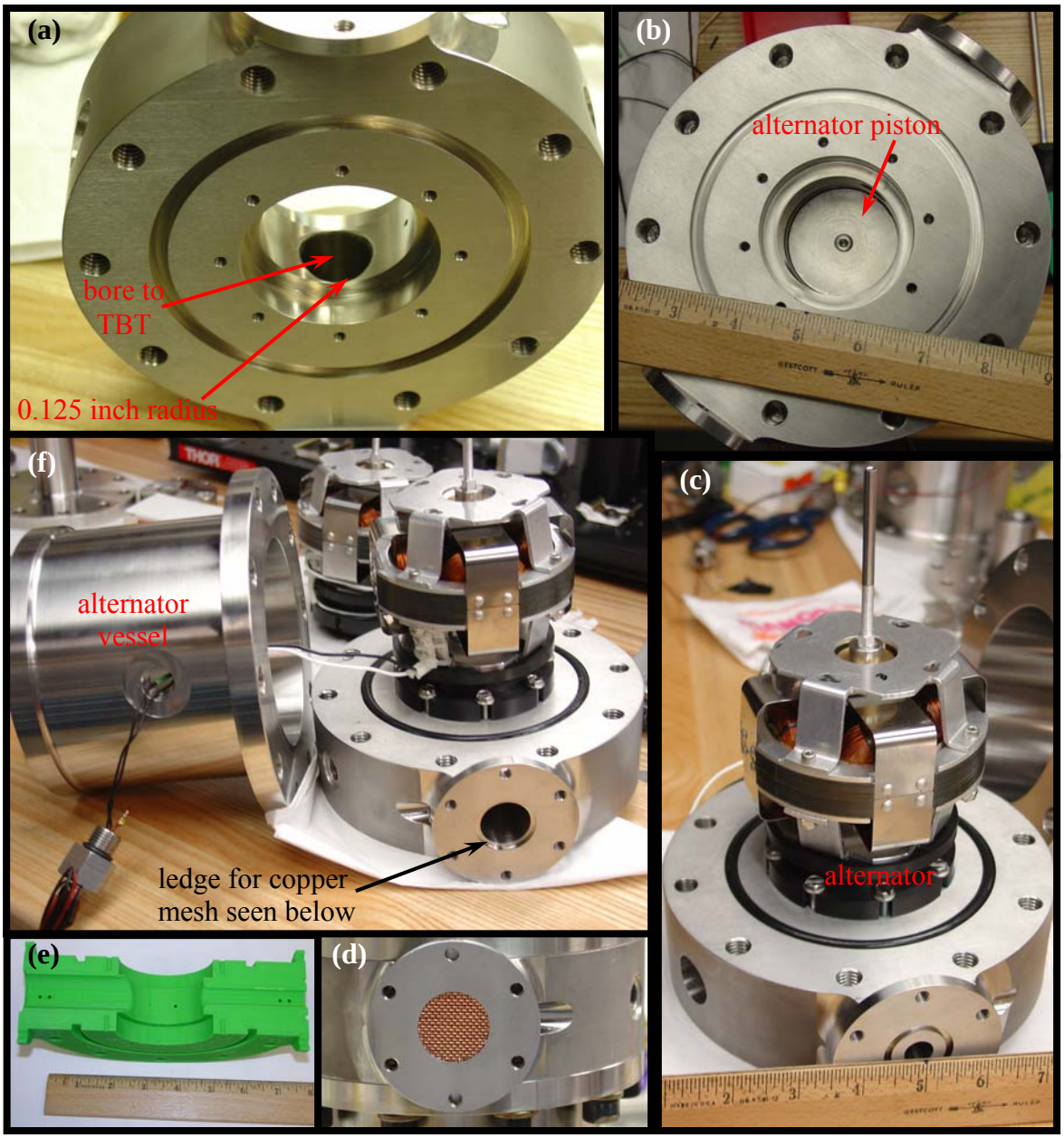

Figure 3.13: Centerplate. (a) view of the radius on the TBT sided bore, (b) view of the alternator piston looking through the compression space, (c) alternator mounted to Centerplate, (d) a few layers of 24 wires per inch copper mesh that serve as a TBT flow straightener and a secondary heat exchanger, (e) rapid prototype plastic model of ½ of the Centerplate, made to assist in design and manufacturing discussions and (f) mounted alternator wired to electrical feedthru and ready to be housed within the alternator vessel.

3.3.3.2.4 Alternator Vessel

During assembly the alternators are wired to electrical feedthrus, the Alternator Vessels are slid over top, bolted to the Centerplate and finally sealed off with basically a blind flange. Behind the alternators is approximately 37 in^3 of "back volume" that acts as compliance to the alternators' moving pistons. This volume, depicted in Figure 3.5(d), was determined by filling the Alternator Vessel with a known quantity of water and then subtracting out an approximation for the alternator's volume; obviously the great surface detail of the alternator prevents a perfect measurement of its volume. The same method was used to determine the surface area of the back volume. Both the volume and surface areas were initially guessed for use in the Appendix A TAPC DeltaE model.

3.3.3.2.5 Jet Pump

Situated in between the Ambient Heat Exchanger and the Compliance is a component known as the Jet Pump. This device, without moving, cleverly suppresses a type of parasitic streaming flow that would greatly inhibit the TAPC's heat to acoustic power efficiency through a convective heat leak away from the HHX.

All types of parasitic acoustic streaming are basically second-order "DC (direct current) flows" that are superimposed on the system's first-order "AC (alternating current) flow." If there is no streaming, each helium molecule within the TAPC will oscillate back and forth returning to its start position after every cycle. Yet when this superimposed DC streaming exists, the helium molecule will oscillate back and forth but this time it will not return to its start position, it will drift a certain distance in the direction of the streaming flow.

The jet pump is used to suppress a type of acoustic streaming, known as "Gedeon streaming" [47], which can be summed up as a net time-averaged DC mass flux away from the HHX and counterclockwise (Figure 3.5(a) orientation) around the loop that makes up the engine [15]. In fact, the looped acoustic network inherently encourages this

Gedeon Streaming [48]. The Jet Pump functions as an annular diffuser in that it reduces the flow's velocity in one direction of the oscillation, thus creating a time-averaged static pressure drop. The result of this pressure differential is a steady DC flow in the opposite direction as the Gedeon streaming which can effectively cancel it out.

The Jet Pump accomplishes this feat by subjecting the flow to different cross-sectional areas and dynamic pressure drops depending on the particular half of the acoustic cycle. The different pressure drops are achieved by subjecting the flow to dissimilar loss coefficients depending on the radii. When the ratio of the radius to the gap between the Jet Pump and the tapered wall, as shown in Figure 3.14(a), is greater than 15% [46], the dynamic pressure drop will be minimized. Thus the Jet Pump subjects the flow to sufficient radii in one direction and large loss coefficient sharp radii in the other direction. It is noted that current understanding assumes that these oscillatory flow losses can be computed by cycle averaging the losses based on steady "one-directional" flow [49]. Furthermore, the taper enables a cross-sectional area increase which forces a velocity decrease and thus smaller pressure drop in the one direction.

During an arbitrary first half of the cycle, which is depicted in Figure 3.14(b), the flow sees a low dissipation well-rounded entrance lip and small pressure drop because of the cross-sectional area increase (thus velocity decrease). Afterwards during the return stroke, the gas is subjected to sharp corners that have correspondingly big loss coefficients and a larger pressure drop because of the cross-sectional area decrease, the combination of which forces the flow to jet far into the open space above the Jet Pump [18]. The net effect is a time-averaged pressure drop across the Jet Pump which results in a net DC mass flow down and clockwise, in the Figure 3.5(a) orientation, around the loop canceling the counter-clockwise Gedeon streaming.

The necessary loss coefficients and consequent radial gaps between the Jet Pump and the corresponding tapered region to suppress the Gedeon streaming cannot be exactly calculated, hence it was necessary to make the gap and corresponding areas adjustable.

Therefore the Jet Pump is threaded into the Compliance flange to enable translational motion through the tapered region. However, this only enabled a small amount of radial area change, as can be seen in Figure 3.14(c), thus Jet Pumps with various outside diameters were machined and were easily interchanged between test runs. During operation, the Jet Pump will be adjusted until there is a linear temperature change between the hot and cold ends of the regenerator, signifying that the Gedeon parasitic streaming flow is suppressed [14].

The feature on the top of the Jet Pump is inserted into a mating hole in the center of the AHX to co-axially align it and also serve as a limit of upward translation. There are two radial o-rings in this Jet Pump seal because often when they are configured in this radial manner and required to slide, they might not provide optimal sealing. It is noted that these and every o-ring groove [50] in the TAPC was undersized (with achievable tolerances) in order to minimize a compliance volume that the empty part of the groove will form when the system is pressurized. This undersizing will minimize acoustic power dissipation in the o-ring grooves [18]. One final feature is the lip above the threads that limits downward motion and prevents the dangerous ability to unscrew the Jet Pump when the TAPC is pressurized.

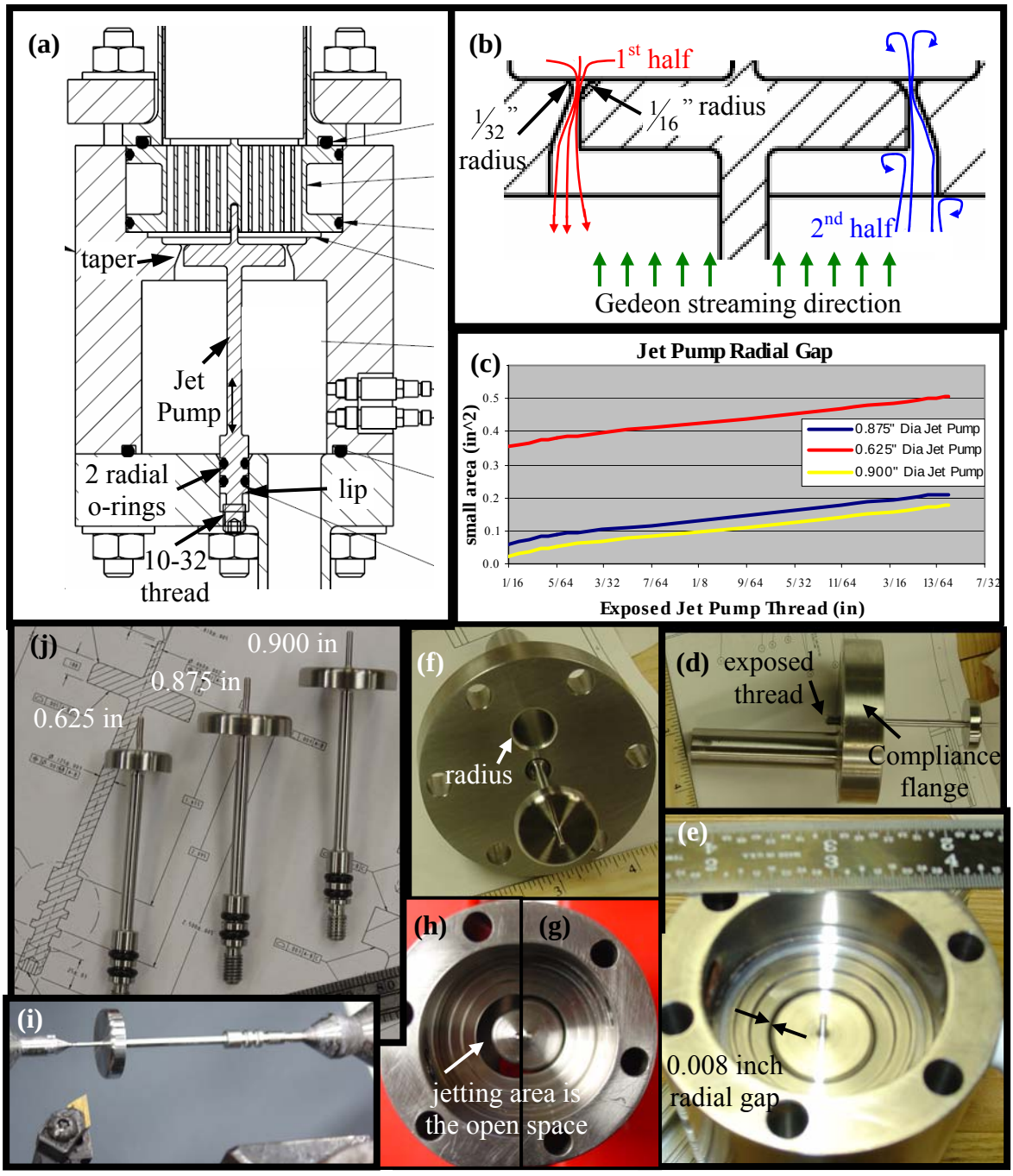

Figure 3.14: Jet Pump. (a) full assembly, (b) zoomed-in view of the tapered region depicting the 1st order acoustic velocity during the two halves of the acoustic cycle [51], (c) small jetting area was adjusted and determined by the amount of exposed Jet Pump thread, (d) exposed thread, (e) 0.900 inch diameter Jet Pump looking down from AHX side, (f) Inertance Tube inlet radius, (g) 0.875 inch and (h) 0.625 inch diameter Jet Pumps, (i) Jet Pump in lathe and (j) three different diameter Jet Pumps side by side.

CHAPTER 4

EXPERIMENT SET-UP

It was critical to make use of multiple sensors and measurement devices in order to shakedown, troubleshoot and quantify the performance of the Thermoacoustic Power Converter. Even more importantly, some of the sensors ensured safety by keeping the operating conditions within the design boundaries. Displaying the outputs of these sensors was not enough in most cases, a data acquisition system was necessary to record the data that would be later analyzed. Other devices were also needed to support operation by providing the required heat source and sink. The TAPC and these supporting devices is shown in the test facility photos of Figure 4.4.

4.1 Measurements

There are many important sensors that monitor a variety of quantities including temperature, pressure and alternator piston location. Figure 4.1 shows the location of each of these sensors.

4.1.1 Temperature

Located throughout the TAPC are Type-K thermocouples [52] that monitor the various temperatures. There are twenty total in the Thermodynamic Section alone. Five were spot welded along the outside wall at equally spaced distances along both the TBT and the Regenerator housing. The HHX has five thermocouples inserted into pre-drilled holes 0.125 inches from the upper gas surface boundary and another three were spot welded to the underside of this component at equally spaced distances between the TBT and REG. These eight thermocouples at various spots on the HHX verify that there are no hot spots due to the oscillating flow not accessing all of its internal area. The final

two Thermodynamic Section thermocouples monitor the chilling water flowing into and out of the AHX.

Imbedded in each alternator electrical feedthru [53], which seal to the side of the Alternator Vessels, are thermocouples that monitor the alternators' temperature. Also in the Acoustic Section are thermocouples attached to the outside of the Inertance Tube and Centerplate. Both of these should read ambient room temperatures, but if there is an acoustic streaming heat leak, these will read warmer temperatures.

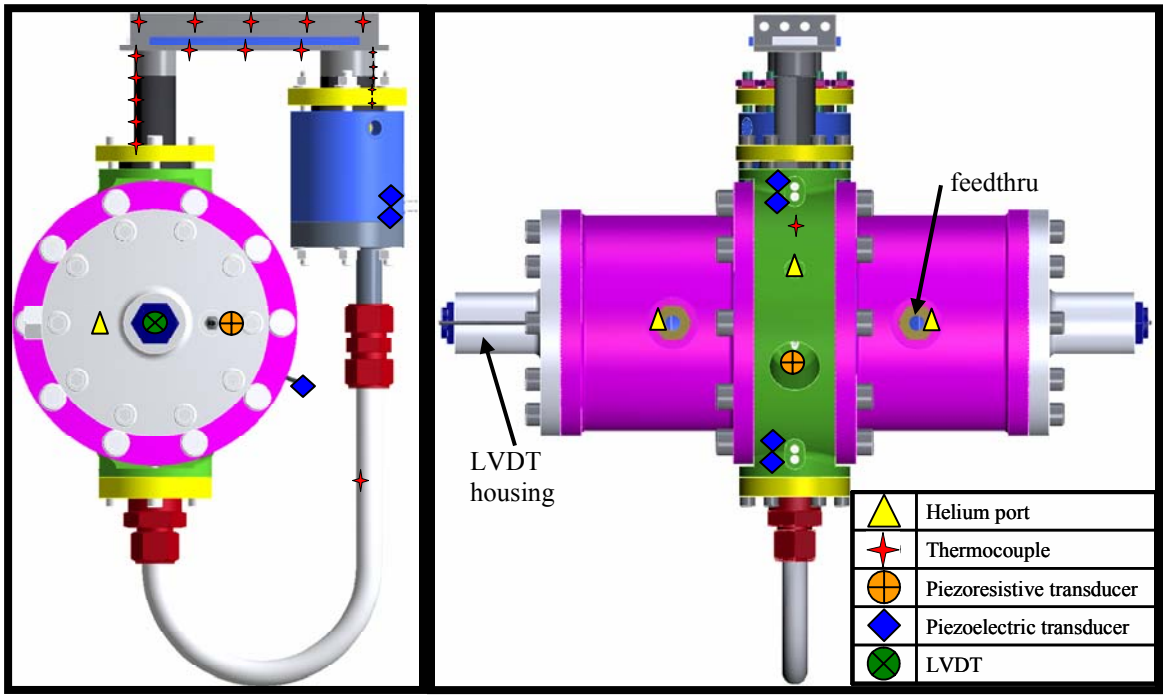

Figure 4.1: Sensor locations

4.1.2 Pressure

Located throughout the pressure vessel and pressure fill system are both static and dynamic pressure gauges. Some of these are critical to prevent inadvertent over pressurization while others are used to quantify the performance of the TAPC.

4.1.2.1 Static Pressure

4.1.2.1.1 Dial Gauges

There are dial gauges on the helium fill tank, the low-pressure side of the regulator [54] and a repetitive third [55] at the junction upstream of the three independent ports into the TAPC. The second two gauges listed ensure that the piezoresistive pressure transducers are outputting the correct helium pressure as the TAPC is being filled, providing added safety.

4.1.2.1.2 Piezoresistive Pressure Transducers

It is necessary to know the static mean pressure once the three inlet ports are shut during operation. Piezoresistive pressure transducers [56] were mounted on the two Alternator Vessel Rear Flanges and in the Centerplate. Three were necessary because the tight clearance gap between the two alternator pistons and their respective cylinder walls form an effective boundary. Thus the internal volume of the TAPC could be considered three separate entities, the two back volumes behind the alternators and the engine itself. It is noted that this type of transducer acts like a strain gauge and needs to be externally powered with a DC power supply [57].

4.1.2.2 Dynamic Pressure

4.1.2.2.1 Piezoelectric Pressure Transducers

The operating TAPC has a 100 Hz acoustic pressure oscillation on top of the mean static pressure. Specifically at a 10% acoustic pressure amplitude an arbitrary transducer will read 495 psig (45 psig added to the mean 450 psig) at one instant, then a half-cycle (0.005 seconds) later, the transducer will feel 405 psig. Piezoelectric transducers [58] were used because it was worried that the piezoresistive type would not be able to respond quick enough to capture the 100 Hz pressure oscillations. In fact, the

piezoelectric type of transducer can only respond to dynamic pressures changing with a frequency at least 0.5 Hz; it is insensitive to the mean internal pressure.

There are seven of these transducers inserted at different spots of the engine; one in the compression space between the alternators and pairs in the Compliance, near the TBT and after the Inertance tube. As described in Section 4.1.4.2, the intention of these pairs was to measure acoustic power, which proved to be unfeasible to implement.

4.1.3 Alternator Piston Location

It was crucial to monitor the location of the alternator's piston at all times in order to prevent alternator damage during potential over-stroke operations, piston drift and monitor the actual operating frequency and infer the acoustic power incident on the piston. Depicted in Figure 4.2, this measurement was accomplished by mounting a magnetic rod (core) to the back side of the alternators' respective pistons, such that it translates within a Linear Variable Differential Transducer (LVDT). The transducer, which is threaded into the Alternator Vessel Rear Flange, will then output a signal depending on where the core rod is located within it.

Limiting the back volume behind the alternators' was important to minimize a surface area to volume ratio dependent gas thermal hysteresis [15, 33]. The back volume is sized to provide the proper stiff compliance; which is constrained by the height of the alternator when the large open space of its complicated internals (around the copper coils and spring straps) is taken into consideration. Specifically the surface area of the Alternator Vessel and its Rear Flange is essentially an isothermal boundary; along this area there will be some thermal penetration depth between the isothermal boundary and the adiabatic open volume. So as the pressure swings in the essentially "wide open" back volume, the gas will heat and cool relative to the isothermal boundary and cause an irreversible acoustic power loss. In order to minimize this surface area and

corresponding volume, a special LVDT was purchased that could be threaded and sealed right to the pressure vessel wall [59], thus minimizing the effective back volume.

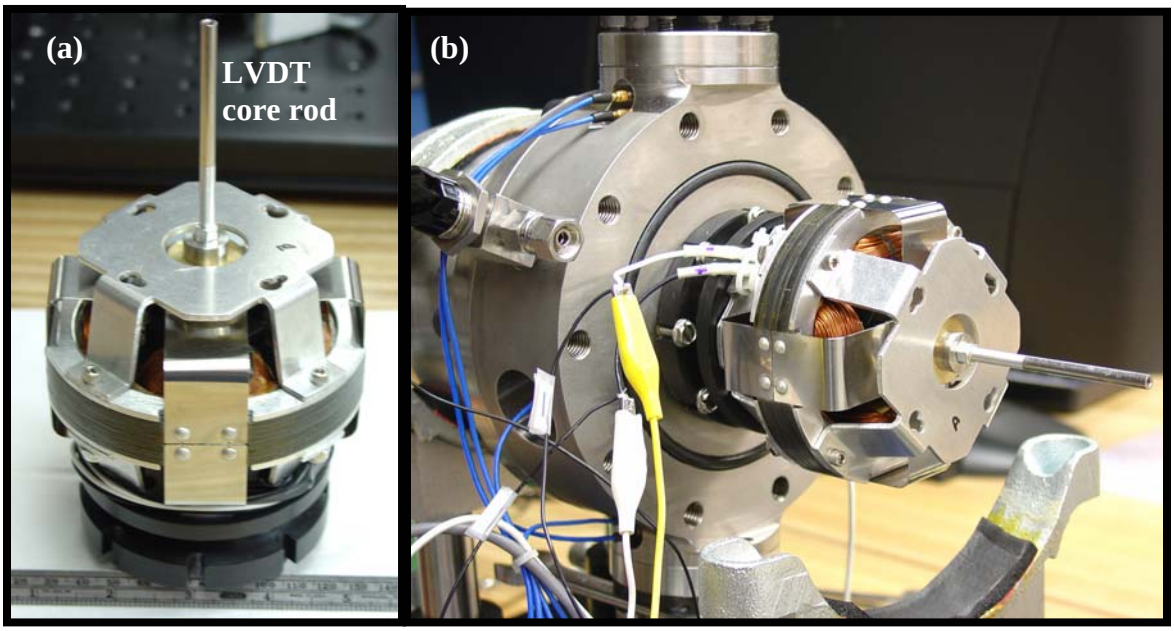

Figure 4.2: (a) LVDT core mounted to the alternator's piston. (b) Alternator and its core mounted to the Centerplate of the TAPC, prior to the Alternator Vessel being bolted on.

4.1.4 Power

In order to quantify the performance of the TAPC it was necessary to monitor the heat input, acoustic power and electric output. This data will explain the effectiveness of the two independent energy conversions.

4.1.4.1 Heat Input

As developed in Section 4.2.1, different heat sources were used. The output of the DC power supplies were fed through a digital multimeter [60] in order to monitor their output and be able to input a scaled signal into the data acquisition system. Even though the temperature controller heat source ensured a constant HHX temperature, it prevented an accurate heat input measurement because of its inherent duty cycle (Section 4.2.1.1).

4.1.4.2 Acoustic Power

The task of the TAPC work was to demonstrate an electrical output from only a heat source. Since the alternators were bought from a vendor, the vast majority of work involved the detail design of the engine. This reality resulted in a secondary objective of being able to quantify the engine's conversion of heat into acoustic power.

It is noted that the acoustical power normalized over a duct's cross-sectional area is known as acoustical intensity, I; for steady state fields it is defined as the time average (denoted by the over-bar) product of pressure and velocity [61]:

$$I = \frac{1}{\mathrm{T}}\int_0^{\mathrm{T}} p \cdot v dt = \overline{p(t) \cdot v(t)}\,. \tag{4.1}$$

This intensity only represents the central region of the duct because it doesn't take into account the boundary layer that exists along the wall. Acoustical power, E_2, can then be written as a function of Intensity in the following form:

$$E_2 = I \cdot A = p(t) \cdot U(t). \tag{4.2}$$

4.1.4.2.1 Two Pressure Sensor Method

When two pressure sensors are adjacent to each other, the average of the two signals can be used to obtain the pressure at their midway point while the velocity can be inferred by the phase difference between their respective signals [62]. This data can then be used to determine acoustic power through a new form of Equation 2.4 [18]:

$$E_2 = \frac{A}{2\omega\rho_m \Delta x}\left|p_{1a}\right|\left|p_{1b}\right|\cos(\phi_{ab}), \tag{4.3}$$

where a and b represent the two independent transducer signals and ϕ_{ab} is the phase angle between them. This two-sensor method is a well-established and proven technique [63] but is predicated on a few key assumptions [18,25,62,64]:

- The acoustic wave has a relatively low frequency.
- The duct is sufficiently long, straight, cylindrical and has rigid walls

- The duct's radius and distance between the two sensors is much less than the acoustic wavelength.
- Laminar boundary layer.
- The volumetric velocity can be confidently inferred.

Shown in Figure 4.1, there were three pairs of pieozoelectric pressure transducers mounted in various locations of the TAPC. The desire was to employ the two pressure sensor method of determining acoustic power at each of these locations and then map out their change in time. However, after the drawings were finalized and component manufacturing began, it was realized that this method for measuring acoustic power could not be used with any confidence because the velocity at each of the three locations could not be confidently inferred [25]. The reality is that flow turbulence certainly occurs at each of these locations and none of the internal ducts that make up the TAPC are "sufficiently long," that being said, the volumetric velocity cannot be "confidently inferred." The lack of experience in the application of thermoacoustics at the beginning of this project resulted in a futile attempt at measuring acoustic power.

4.1.4.2.2 Alternator Piston Motion Method

The volumetric velocity in the previous method had to be inferred, while it can be determined by the motion of the alternators' pistons. This method uses the cross-sectional area of the piston and its displacement amplitude, via the LVDT, in conjunction with a flush mounted pressure transducer in the compression space (volume in between the two alternator pistons). The resulting formulation for the acoustic power incident on an imaginary surface located in front of a single alternator piston is identical to Equation 2.4:

$$E_2 = \frac{1}{2}\left|p_{1c}\right|\left|U_{1p}\right|\cos\left(\phi_{pU}\right), \tag{4.4}$$

where p_{1c} is the magnitude of the pressure oscillation in the compression space, U_{1p} is the magnitude of the piston's volumetric velocity oscillation and ϕ_{pU}. As stated previously, this velocity is determined from the piston's displacement amplitude, ξ_{1p}, [25]:

$$\left|U_{1p}\right| = \omega \cdot A_p \cdot \left|\xi_{1p}\right|, \tag{4.5}$$

where ω is the angular operating frequency, A_p is the cross-sectional area of the piston.

Obviously the phase angle between the pressure and velocity signals, ϕ_{pU}, cannot be determined, yet it can be accurately inferred from the phase angle between the pressure and displacement amplitude. Thinking intuitively about the motion of the piston, it peaks in displacement when its velocity is zero, and conversely, it is moving quickest when it is at its zero-equilibrium position; in other words, there is a 90° phase shift between the peaks of the piston's sinusoidal displacement and velocity. Defining $\theta_{p\xi}$ as the phase angle, in radians, between the pressure and displacement amplitudes:

$$\phi_{pU} = \theta_{p\xi} + \frac{\pi}{2}. \tag{4.6}$$

The operating acoustic cycle time within the TAPC is 0.01 seconds, simply the inverse of 100Hz. So the time it takes for the piston to feel the acoustic pressure in the compression space and translate the full peak to peak displacement is around 0.005 seconds. Saying this, it is apparent that the phase measurements between the compression space pressure and piston displacement is very sensitive. In order to obtain such a minute and critical measurement, a Lock-In Amplifier with a 0.001° resolution was used [65]. This device "locks-in" to the compression space pressure signal as a reference, compares it to the piston's displacement signal (via the LVDT) and then outputs their difference in terms of magnitude and phase.

4.1.4.3 Electric Output

The alternators were run in parallel with a 250Ω rheostat [66] which served as the variable resistive load capable of dissipating the electrical power, Figure 4.3 shows this

circuit. Analog current and voltage meters and a power analyzer is used to monitor the electrical output.

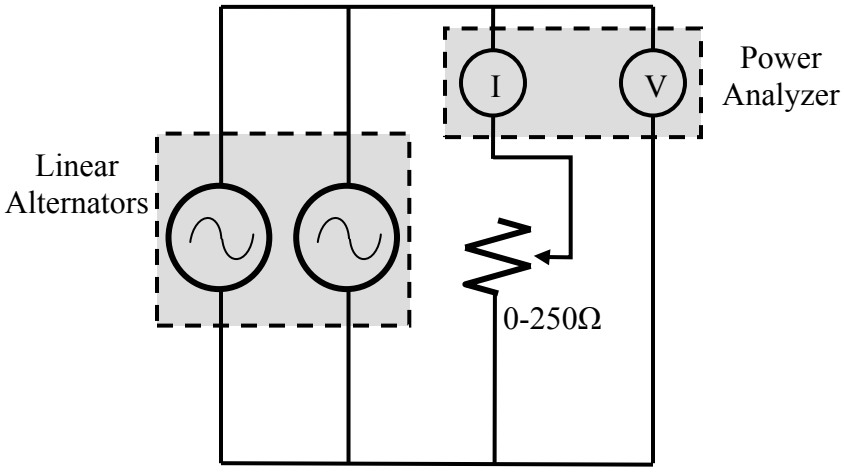

Figure 4.3: Load circuit for the TAPC. The power analyzer is wired in parallel with the resistive load to monitor voltage and in series between the alternators and rheostat in order to read the current through the load. It is noted that "less load" is synonymous with a higher load resistance because it means less current is going through the circuit and is effectively approaching an "open" condition. A lower rheostat value allows more current to flow with a limit of 0Ω causing a "closed circuit."

The single phase 100Hz TAPC electrical output is monitored with a power analyzer [67] that had one channel dedicated to the voltage across the resistive load and another channel that monitored the current through this rheostat. This device is capable of displaying the real time voltage, current, power produced in watts, and even the phase between these components.

4.2 Supporting Devices

Successful operation of the TAPC required a few supporting devices; namely a heat source, heat sink and a means of kick-starting operation. Figure 4.4 shows the test facility and these other devices during operation of the TAPC.

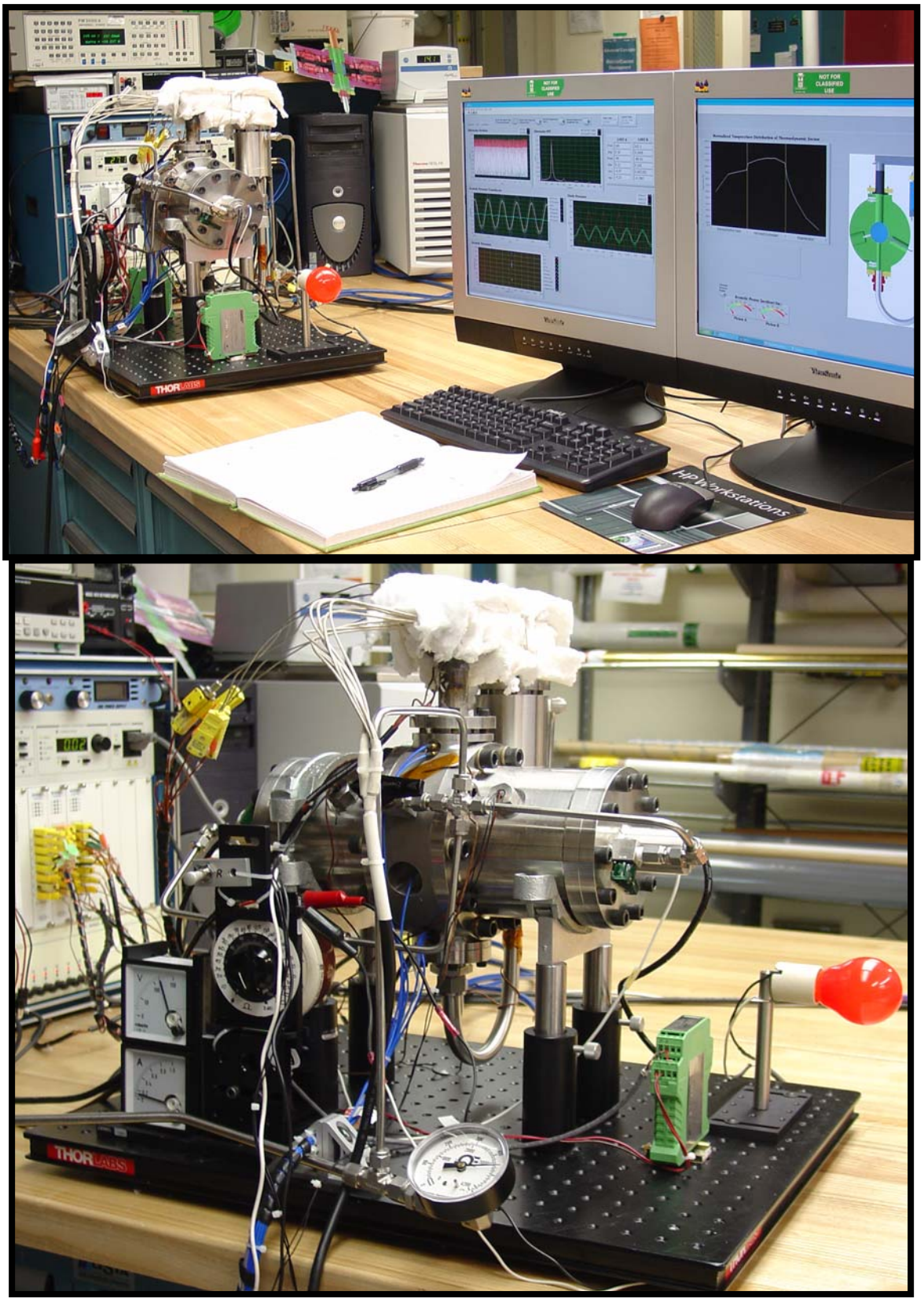

Figure 4.4: TAPC test facility during operation.

4.2.1 Heat Source

Depicted in Figure 3.8(d), the experimentally convenient cartridge heaters were used to input heat into the TAPC. These heaters were run in parallel and powered with either a Temperature Controller or a DC power supply. The objective of a particular test determined what power supply would be used. The Temperature Controller provided a very convenient way at keeping the hot end temperature constant, and the DC power supplies enabled easy efficiency calculations.

4.2.1.1 Temperature Controller

The Temperature Controller [68] uses a thermocouple as a feedback in order to keep the temperature constant at the spot of that reference thermocouple. It does this by turning the power to the cartridge heaters on and off in an attempt to keep that temperature constant at some set point. This device conveniently keeps the hot end temperature at some fixed value, but this on/off "duty cycle" and the fact that the power into the heaters is AC (at 230 volt 60 Hz out of the receptacle on the wall) makes the determination of the power into the TAPC very complicated. During the early stages of testing a "clamp-on" ammeter was put around the four cartridge heater input leads and fed into the data acquisition system. This amperage was a 60Hz signal at some duty cycle; the DAQ system averaged the RMS value of this signal over some period of time that effectively incorporated all of the on/off cycles. This average current value was then multiplied by the 230 volts out of the wall socket in order to get the power in. The ammeter proved very unreliable and this method was much more complicated then necessary.

4.2.1.2 DC Power Supply

In order to determine the power in and make accurate TAPC efficiency calculations, DC power supplies capable of powering the four cartridge heaters were

used. These sources inherently avoid both the necessity to calculate RMS amperage and that duty cycle. Two power supplies [69,70] were used in parallel because neither of the available sources were powerful enough to run the heaters during TAPC operation.

4.2.2 Heat Sink

The water jacket surrounding the AHX was kept cool (approximately 50°F) with a water chilling device [71] that pumped water through the AHX water ports and cooled it to a pre-programmed temperature.

4.2.3 Power Amplifier

It turns out that a means of kick-starting the operation of the TAPC is necessary in the current test set-up; this will be discussed in Chapter 5. This was accomplished by wiring the alternators in parallel to an AC power source [72] that could be programmed to supply any voltage, current and frequency.

4.3 Data Acquisition System

It is critical not only to monitor these sensors and devices in real time, but the data recorded would be later reduced to help in troubleshooting and quantifying the performance of the TAPC.

4.3.1 Hardware

The temperature, pressure and LVDT sensors supplies data to a single chassis [73] that compiles it and sends it along to a high speed data acquisition card [74] installed in the motherboard of a stand alone personal computer. Furthermore, the high speed transient data (piston motion and acoustic pressures) is put through a special module [75] that enables their acquisition with negligible skew in time. This module essentially phase-locks their signals before input to the DAQ card via the chassis.

4.3.2 Software

The data is then reduced, scaled, displayed and recorded with lab software [76] in a manner that supports both real-time control and post test analysis. Depicted in Figure 4.5 is a snapshot of the data displayed during operation of the TAPC.

Time data is shown in the *Alternator Position*, *Acoustic Pressure Transducers* and *Static Pressure* plots while the lab software goes further and performs real time Fast Fourier Transforms (FFT) to develop the *Alternator FFT* and *Acoustic Pressure* plots. This manipulation is critical because time data at such a high frequency conveys little information, albeit a great deal can be deduced from the amplitude and frequency components of the acoustic pressure and alternator motion (LVDT) data.

The array of data underneath the *LVDT A* and *LVDT B* refers to the motion of the Alternator A and B (arbitrary) pistons. Even though the amplitudes (in inches) are very similar for these two pistons (0.160 vs. 0.179), the zero equilibrium point of Alternator A has shifted 0.080 inches. This DC offset is confirmed by looking at the transient *Alternator Position* line in white for LVDT 3163 (Alternator A); an issue that will be discussed in Chapter 5.

The second monitor displays the temperature data and plots the important Thermodynamic Section over a normalized length in which the TBT makes up the temperatures from zero to one, the HHX is normalized from one to two and the REG data is plotted between two and three. The temperatures are plotted in this fashion because the profiles of the TBT and REG quickly display the existence of acoustic streaming, i.e. heat leaks away from the HHX. Ideally the TBT and the REG will be perfectly linear from about 100°F to whatever flat HHX temperature profile. Obvious in this snapshot is the existence of multiple types of acoustic streaming that will be discussed in Chapter 5.

The acoustic power incident on the two respective pistons (Section 4.1.4.2.2) is also displayed on the second monitor using the output from the Lock-In Amplifier discussed previously. However it was not displaying power data during this snapshot.

The lab program had many features that benefited real time analysis, but they weren't all used at once in order to prevent the program from slowing down. This was critical to prevent the pistons from over-stroking during transients where the load on the alternators was changed in an attempt to find a new maximum power point.

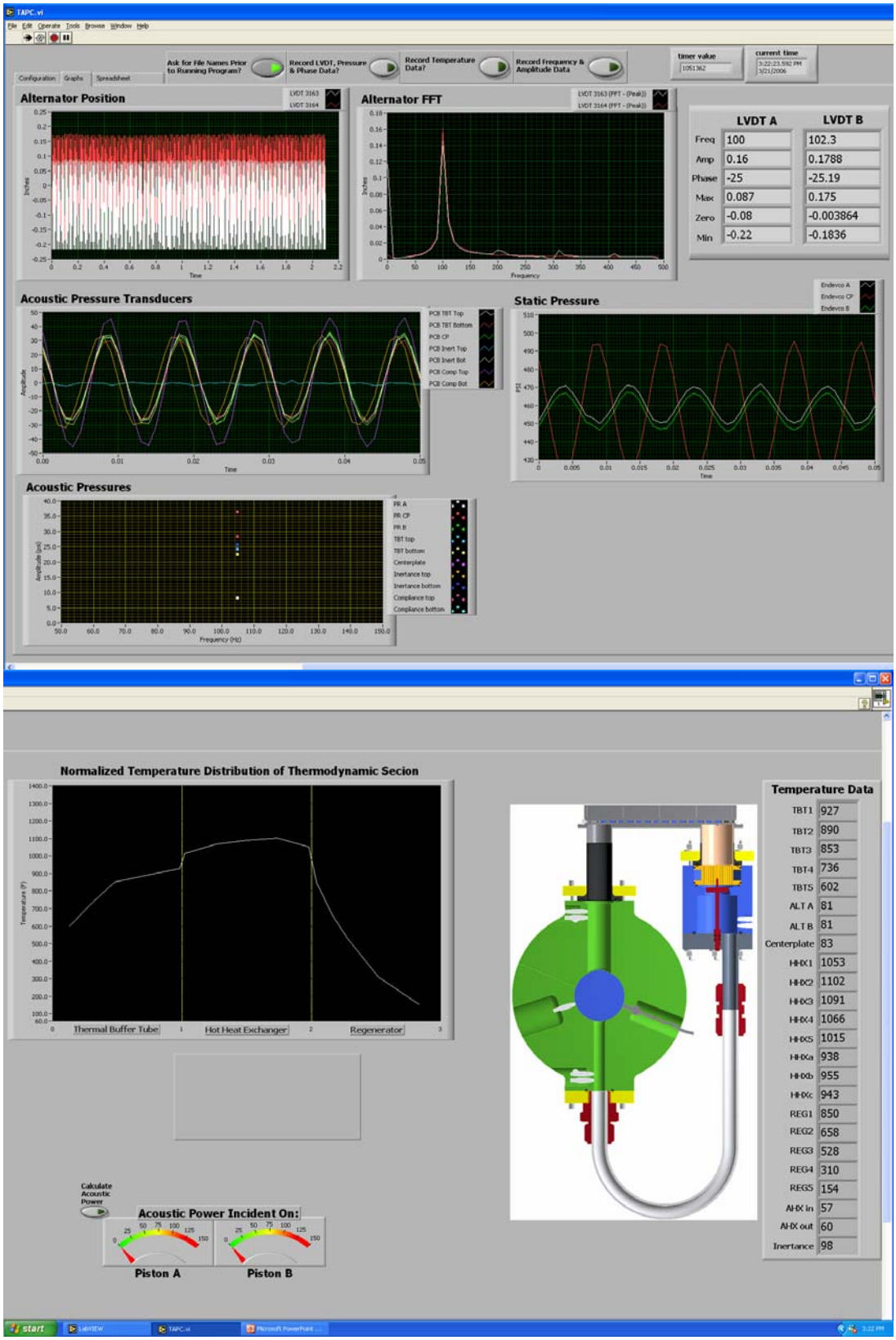

Figure 4.5: TAPC data display during operation.

CHAPTER 5

TESTING

Once the TAPC is pumped with helium to 450 psig and its three independent inlet ports are closed, the cartridge heaters can be powered up and brought to temperature. However, it turns out that these steps are the only remaining parts of the operating procedure known prior to the first test run. The reality is that the TAPC is an experiment and additionally, the second of its kind. Hence shakedown testing has taken a great deal of time as the result of multiple changes and test runs. Saying this, it is understood why the performance testing reported here is somewhat preliminary. Nevertheless, the knowledge of the TAPC system attained through the shakedown testing has been invaluable and the performance to date is very promising.

5.1 Initial Shakedown Testing

The heat-up was initiated after assembly had been completed, all leaky joints were found and sealed, the sensors were calibrated, the DAQ system was recording and displaying real time data, the Thermodynamic Section was insulated, the internal helium was pressurized to 450 psig, the rheostat was maxed out to provide a small load on the alternators and safety goggles were donned. It was anticipated that the TAPC would self start at a HHX temperature of about 750°F, based on the referenced Northrop Grumman/LANL thermoacoustic generator [15]. However, nothing happened even when the Temperature Controller was programmed to bring the HHX to 1350°F. The TAPC didn't turn on even when the Jet Pump was backed out all the way, two rheostats were

put in series to provide a larger load resistance, the ports were opened up and the mean pressure was decreased slightly. The first test run was terminated at this point.

Prior to the second heat-up, the alternators were put in-line with a 3-way toggle that could switch between a variable AC power source into the alternators, an open circuit condition and the rheostat resistive load necessary for TAPC operation, as shown in Figure 5.1. In effect the alternators could now switch between functioning as a pair of compressors as they were motored in phase with the AC power source and become operating alternators when switched in series with the resistive load during TAPC operation. The idea of the AC power source was to cycle the alternators near the 100 Hz DeltaE determined operating resonant frequency and monitor the "ring-down" (return to equilibrium zero position) of the pistons with use of their respective LVDT signals. Basically it was desired to know how many cycles it would take for the alternator pistons to come to rest after the circuit was switched from AC power input to an open circuit.

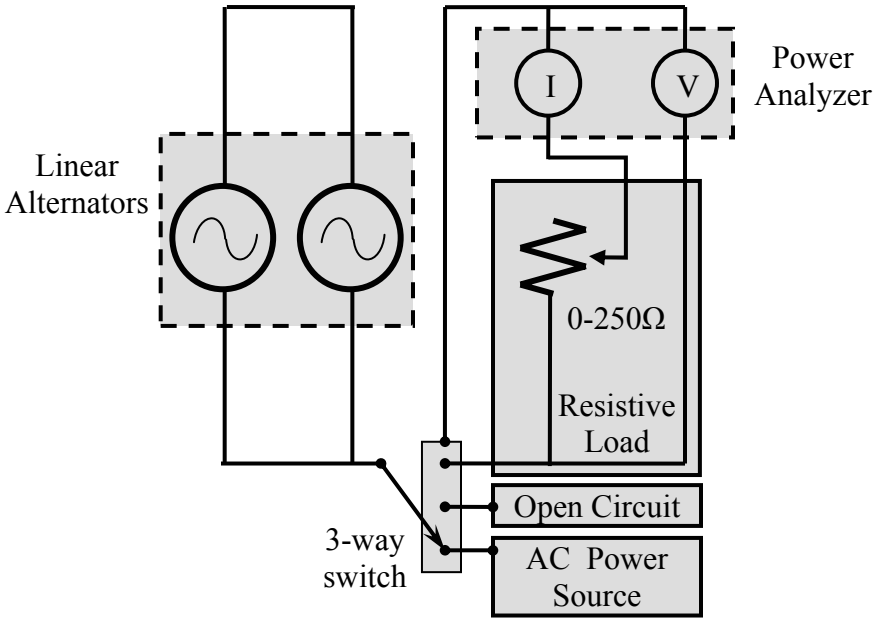

Figure 5.1: Updated TAPC circuit includes a 3-way switch.

The pistons function as a damped harmonic oscillator in which the quality factor of resonance, Q, is defined as a dimensionless version of the drag on the piston, D_p:

$$Q = \frac{\omega M_p}{D_p}, \tag{5.1}$$

where ω is the angular frequency and M_p is the mass of the piston. The quality factor controls the "sharpness" of a harmonic oscillator's resonance [18]; the greater the value, the less energy it takes for the alternators to be motored. Furthermore, as the gas in the TAPC is heated up, the quality factor should increase [77] and as a result, the alternator pistons should take longer to "ring-down" to zero.

The TAPC was heated up in increments during the second test run such that the power to motor the alternators with the AC power source could be recorded at various frequencies around the design 100 Hz. The peak-to-peak stroke of the pistons was recorded and normalized by this power input value and a Q factor was determined at each temperature increment with use of the following equation [26]:

$$Q = \frac{\omega_r}{\omega_2 - \omega_1}, \tag{5.2}$$

where ω_r is the angular resonant frequency that was determined with the Figure 5.2 plot and ω_1 and ω_2 are frequencies above and below this resonance, respectively. It was feared that the TAPC would never start up because it might require a temperature hotter than what could be safely applied. Figure 5.3 plots the inverse of Q for each of the tested temperatures and is effectively extrapolated to determine this hot end self-start temperature. Both of these plots were being formed during the test run and even though the resonant frequency in Figure 5.2 was increasingly more defined and "sharp," the linear trend in Figure 5.3 was quickly extrapolated to a self-starting temperature near 1700°F, well outside an operable range.

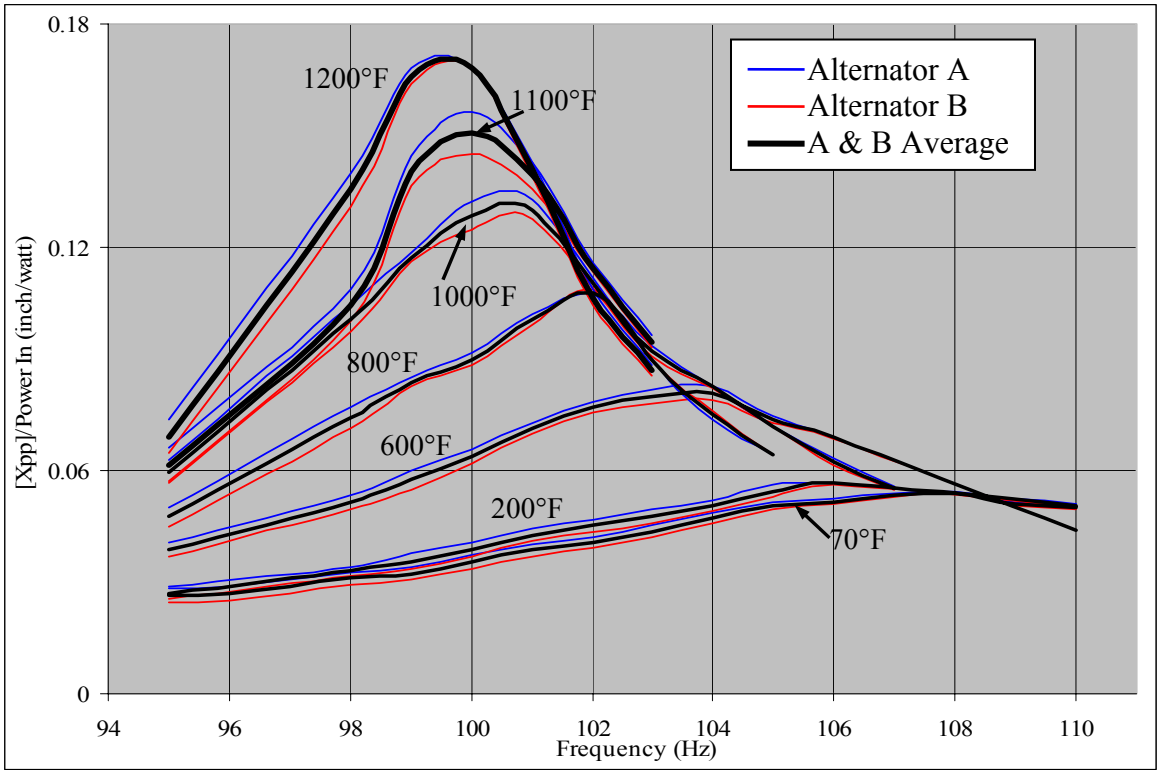

Figure 5.2: Alternator piston peak-to-peak stroke (normalized by input AC power) versus motoring frequency at various temperatures during shakedown Test #2. The resonance frequency becomes more defined as temperature is increased.

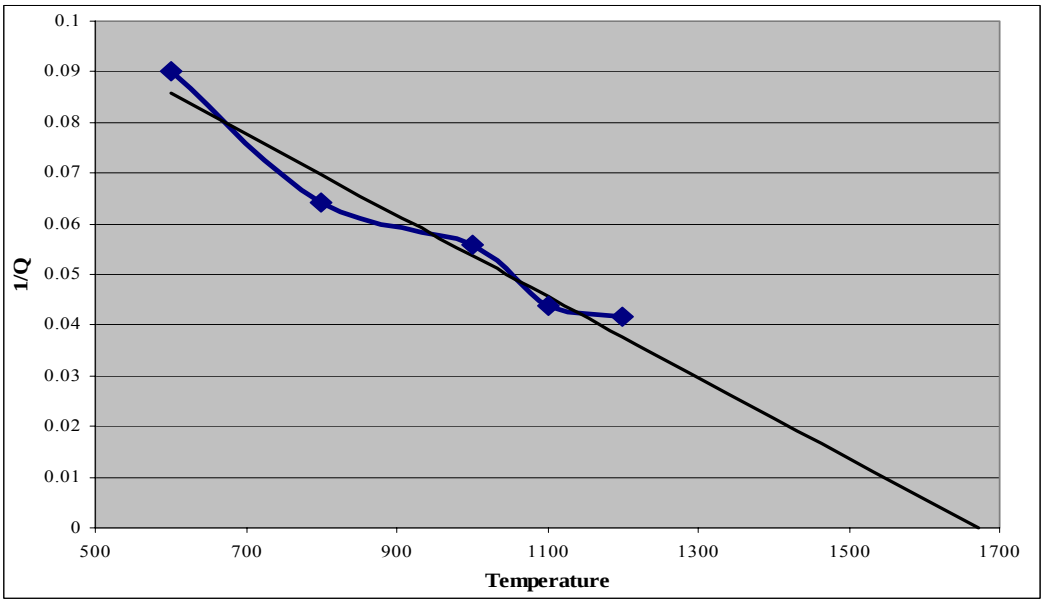

Figure 5.3: Quality factor inverse as a function of temperature. This factor is based on the average resonance plots in Figure 5.2.

During the heat-up of this test run at about 1140°F the current through the alternators became indecipherable as the AC power source readout was quickly changing by tenths of an amp. At this same time a small "beat tone" was hear and actually displayed by the LVDT signals. This tone is a simultaneous sounding of two slightly different frequencies [26]; it showed up in the LVDT signal versus time display as an oscillation superimposed on top of the 100 Hz drive frequency. The TAPC had begun to operate; it was resonating at a frequency slightly different then what the alternators were being driven at by the AC power source. The switch could now be flipped from the AC power-in mode to the resistive load to generate actual power.

The rheostat was still at a maximum value (during this test it was 300Ω) and the switch was flipped at which point the TAPC started to shake and the banging of the over-stroking pistons was heard. After only a second, the AC power source was again switched "on" in order to grab and drive the pistons at safe amplitude. It was immediately feared that the alternators were broken. This over-stroking was the result of an improper guess for the load resistance, in other words the thermoacoustic engine was producing excess power relative to what could be dissipated in the rheostat. Therefore the amplitude of the piston's motion quickly increased from what it had been during AC drive to what it wanted to do naturally with a 300 Ω load resistance. This value was greater than the maximum alternator ±0.250 inch stroke, hence the pistons bottomed out.

The alternators were again driven at that same frequency and amplitude for less than a minute and the same beat tone appeared. This time the switch was flipped to a resistive load of 100 Ω but the pistons came to rest because the load was too high. The alternators were again driven with the AC power source and the rheostat was turned to 300 Ω again, except this time when the load was switched in after the "beat tone" observation, the pistons came immediately to rest. The heat was turned off at this point because it was felt that the over-stroke occurrence caused permanent damage to the alternators.

The TAPC was partly disassembled, inspected and the alternators were again driven by AC power source with no difficulties, however there was some apparent damage. Noticeable divots were found on both alternator housings from where the pistons over-stroke and made rapid contacts (the alternators were cycling at 100 Hz during the over-stroke occurrence for about a half second, so the pistons hit their housings some fifty times) until the switch was flipped and they were pulled to a safe amplitude by the AC power source. Besides these divots, the only other noticeable issue was that the core rod attached to one of the pistons had been skewed and made rubbing contact with its LVDT, which was easily fixed.

Discussions about the prior test run led to the suggestion that maybe the pistons were sticking within their respective cylinders for a portion of their stroke [25]. The extremely small piston-cylinder clearance gap enables optimum efficiency but opens up the possibility of rubbing because if there is any skew of the cylinder's axis relative to the piston's axis, there will be friction between the two parts.

5.1.1 Lessons Learned - Rubbing Alternator Pistons

The TAPC DeltaE model is based on the tight clearance gap given from the alternator manufacturer. If there is any friction at all between a piston and its respective cylinder, the system will not start on its own given the original design parameters of heat input, cooling temperature, mean gas pressure, etc. This can also be extended by the fact that if the respective pistons respond differently (more or less rubbing); the ability to resonate correctly might be affected. This is because the resonating pistons are effectively a joint spring-mass oscillator in the eyes of the entire TAPC system. Hence they need to respond correctly in order for the thermoacoustic oscillation to start, ramp up in amplitude, be electrically constrained by the load on the alternators and display a sustained oscillation to make power.

This rubbing idea was actually confirmed in two manners. In the first test the TAPC was assembled but not pressurized and one at a time the alternators were wired to a DC power supply. Slowly current was increased and there was no piston motion in one of the alternators until a certain repeatable amperage was put through the alternator coils. Specifically one of the alternators required 150 milliamps of current before it moved, that is before it could overcome the friction between its piston and cylinder. The other alternator required a somewhat negligible 50 milliamps.

This notion was also tested in a different manner in which a pressure differential was applied to the two sides of the alternator's piston. It is much too difficult to apply a small enough pressure differential, with solely the gas plug valves, to see that initial friction in the same manner that the amperage test displayed. However, this test was able to demonstrate how the alternator pistons returned to their equilibrium (zero) position when forced in either direction by the applied pressure difference. The alternator that showed the large amount of initial friction also took a long time (~ten seconds) to return to its zero position after the pressure differential was allowed to equalize between the front and rear. However the other piston (LVDT A in the *Alternator Position* plot of Figure 4.5) would instantly come back to zero when the pressure on the two sides of the piston was allowed to equalize. This didn't mean friction or rubbing per say, but it did explicitly show that the two individual alternators respond differently, differently enough to possibly inhibit self-starting. It also supported the DC piston drift that was observed in that same *Alternator Position* plot in Figure 4.5.

The TAPC could now be readied for further testing under the reality that it would be necessary to "kick-start" the pistons through this initial static friction by using the AC power source. This idea is shown in Figure 5.4 where both power production and dissipation is plotted versus the engine's pressure amplitude squared (common dependent variable in thermoacoustics). Even the smallest amount of rubbing (static friction)

between a piston and its cylinder will prevent the engine - linear alternator system from ramping up in amplitude and achieving sustained oscillation [78].

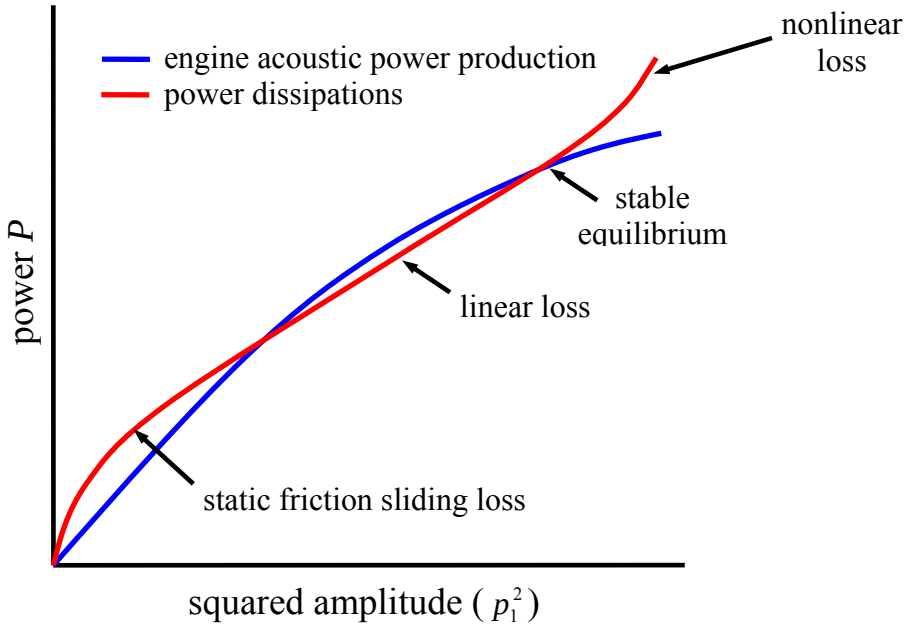

Figure 5.4: TAPC engine-linear alternator system stability. If there is sliding friction within the alternator, it will need to be kick-started [78].

5.2 Further Testing

During the following tests, the AC power source was switched inline to motor the alternators until those same beat tones were observed, at which point it was repeatedly attempted to switch to the rheostat and grab the alternators with a correct load resistance. However this was inherently difficult to do without knowing the load that the alternators wanted to see.

Shown in Figure 5.5, the power produced by the linear alternator is directly related to the acoustic pressure amplitude squared (p_1^2), it does not cross the engine's power production line, which would be the existence of a naturally stabile equilibrium point. The TAPC is only stable when the power dissipations (both useful and non-useful) exactly add up to what is produced by the engine. Thus the "thermoacoustic engine –

linear alternator under resistive load" system hovers the line between exponential growth and decay in order to sustain oscillation and produce power.

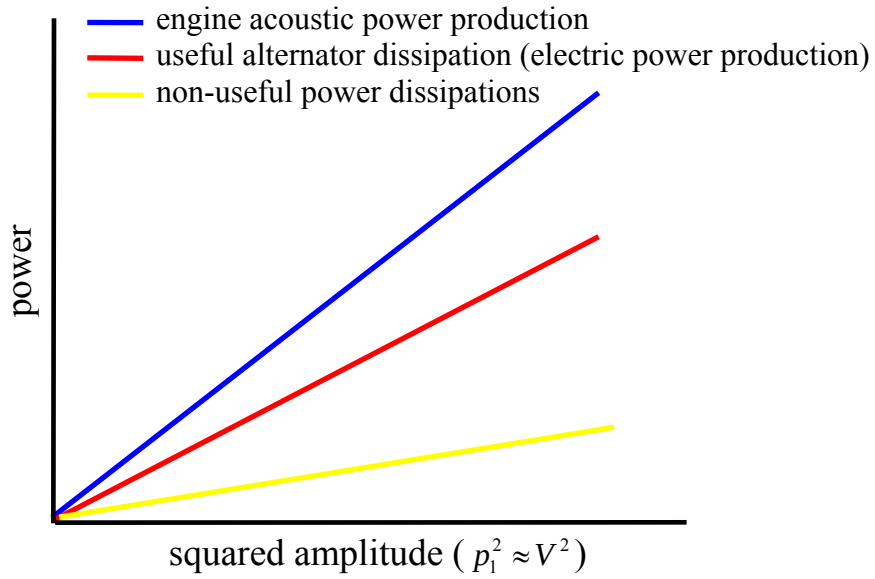

Figure 5.5: TAPC system stability. Useful power production and un-useful power dissipations are plotted as a function of the pressure or voltage amplitude squared. The linear alternator under a resistive load is naturally unstable [78].

It took about eight attempts over three different heat-up test runs before oscillation was sustained for more than a few seconds, ironically it was known after the first few of these attempts that the alternators wanted to see a 250 Ω resistance. However, after a few failed attempts at switching back and forth between the AC power source and rheostat, the beat tones (clue that the TAPC is operating) would not appear anymore. When this happened, the TAPC was allowed to cool before more attempts at producing that beat tone and grabbing the moving alternators with the 250 Ω load was attempted. Something else was happening that prevented those beat tones after a few failed attempts and ultimately prohibited sustained oscillation.

After five minutes or so of motoring, enough hot gas had been forced down to the pistons to cause them to expand and drag. At which point the pistons could still be

motored and forced to move with the AC power supply but they dragged enough to prevent the TAPC from operating and displaying those beat tones. So if the motoring had lasted for more than about five minutes, no further attempts at switching to the rheostat and achieving sustained TAPC operation could be made. This is why only a few attempts at grabbing the pistons with the load could be tried during each test run even when the correct load resistance was known.

Once this was considered, a thermocouple was placed right on the Centerplate to monitor the temperature closest to the pistons and the alternators weren't motored until the hot end reached 1200°F. At this point the TAPC was switched to the 250 Ω resistance and sustained oscillation on the very first attempt, albeit it only ran for five minutes, power was produced (~36 watts).

5.2.1 Lessons Learned - Acoustic Streaming

Even when oscillation was sustained and power was produced, it only lasted for a few minutes during the first few test runs; basically the length of time that the alternators could be motored in those previous tests. Even though the alternators weren't being motored anymore, they were still moving the same amount under the engine's acoustic power, thus the hot gas was still finding its way to the pistons and causing the alternators to heat up and cease. This is the DC parasitic streaming heat flow, presented in Section 3.3.3.2.5, that the Jet Pump is meant to partly cancel. Previously this component had been thought of as a device to prevent efficiency loss through from DC heat leaks, its ability to keep the hot gas away from the pistons, and thus prevent alternator ceasing, was not really considered until now.

5.2.1.1 Gedeon Streaming

The 0.875 inch diameter Jet Pump had been installed and in its fully open position at the time, that is it enabled a "large jetting area." Obviously from the heat leak issue,

the jetting area had to be decreased in order to cause a larger pressure drop across the Jet Pump region which results in an increased DC flow in the direction countering the Gedeon streaming towards the alternators. The Jet Pump was positioned in its "smallest jetting area" adjustment and on the subsequent test it ran for three minutes longer than the best of the previous test runs. This was in the direction of goodness but obviously not ideal yet.

The TAPC was disassembled and a larger diameter Jet Pump (0.900 inch) was installed and positioned to the smallest jetting area possible, plotted in Figure 3.14(c). Again in the first test, the run time increased again from about six minutes to sixteen minutes. The question at this point was whether or not the Gedeon streaming heat leak was the only culprit for ceasing the pistons after only sixteen minutes of run time? Fortunately the existence of this mass flux (M_2) can be easily checked by observing the temperature profiles of the Regenerator, as shown in Figure 5.6. Even with various hot end (HHX) temperatures, the profiles of the Regenerator become increasingly linear with smaller jetting areas, i.e. a greater DC flow is produced in the direction opposite to the Gedeon streaming. Thus the linearity of the Regenerator temperature profile is directly related to the existence of this type of streaming.

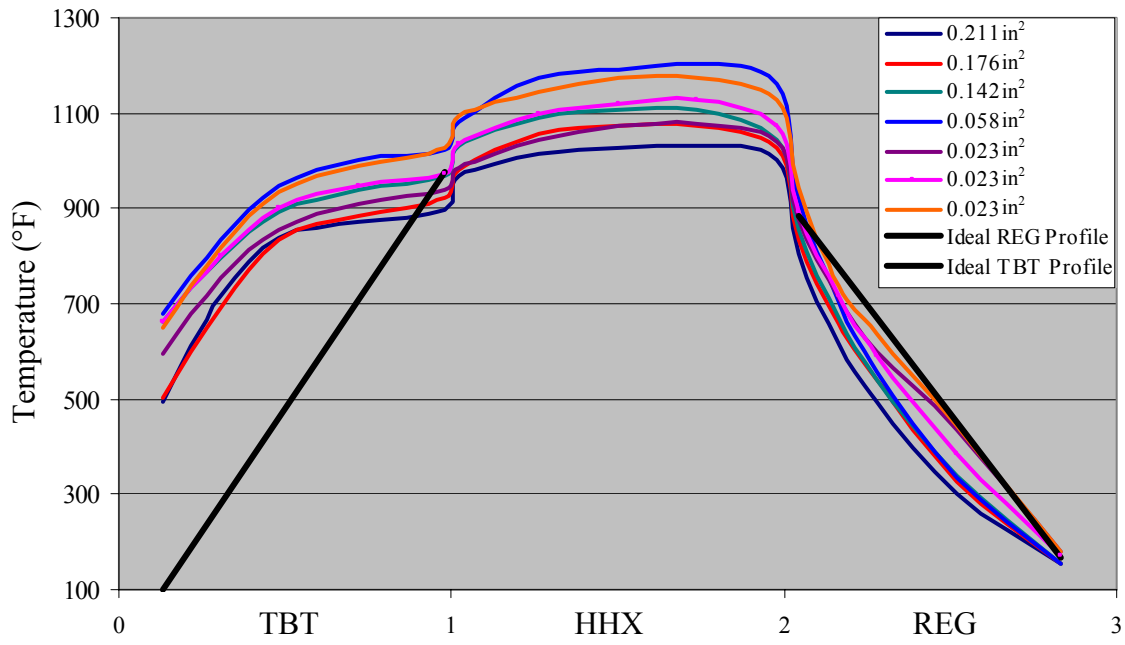

Figure 5.6: Temperature distributions over the normalized thermodynamic section for various Jet Pump positions. Each line is a different test run and small jetting area, which are given in the legend. The black lines are the ideal temperature profiles between the respective hot and cold ends of the Thermal Buffer Tube and Regenerator [15].

The linear temperature profile implies that the temperature at the axial midpoint of the Regenerator is equal to its average temperature (between the hot and cold ends) and if this occurs, then there is no Gedeon Streaming, the heat leak is effectively cancelled [13]. Figure 5.7 plots these differences (normalized by the temperature span) for the various jet pump positions tested. Every data point, regardless of jetting area, is negative because each axial midpoint (at 2½) temperature is less than the corresponding average temperature; this is due to a flux of cold gas entering the cold end of the regenerator. As the jetting area decreases, the temperatures in the Regenerator are approaching a linear profile. Unfortunately a new Jet Pump with a larger diameter is necessary to decrease this jetting area in order to follow this trend towards a point in which the Gedeon streaming is cancelled. That is longer run times should be achieved

when this time-averaged mass flux down and away from the TBT becomes zero and as a result the linear alternators' pistons remain cooler.

Figure 5.7 quantifies these different Regenerator temperature profiles as a function of jetting area. The difference between the midpoint and average temperatures for each test are normalized by their respective hot to cold end temperature span (ΔT). This rids the dependence on the various hot and cold end temperatures seen in Figure 5.6). It is noted that during each test these temperature profiles drifted up as the result of the midpoint temperatures increasing. The data points shown are the average temperature profiles for the duration of each test. Shown is a promising trend towards a point when the midpoint and average temperatures equal, that is when the time-averaged mass flow is effectively canceled.

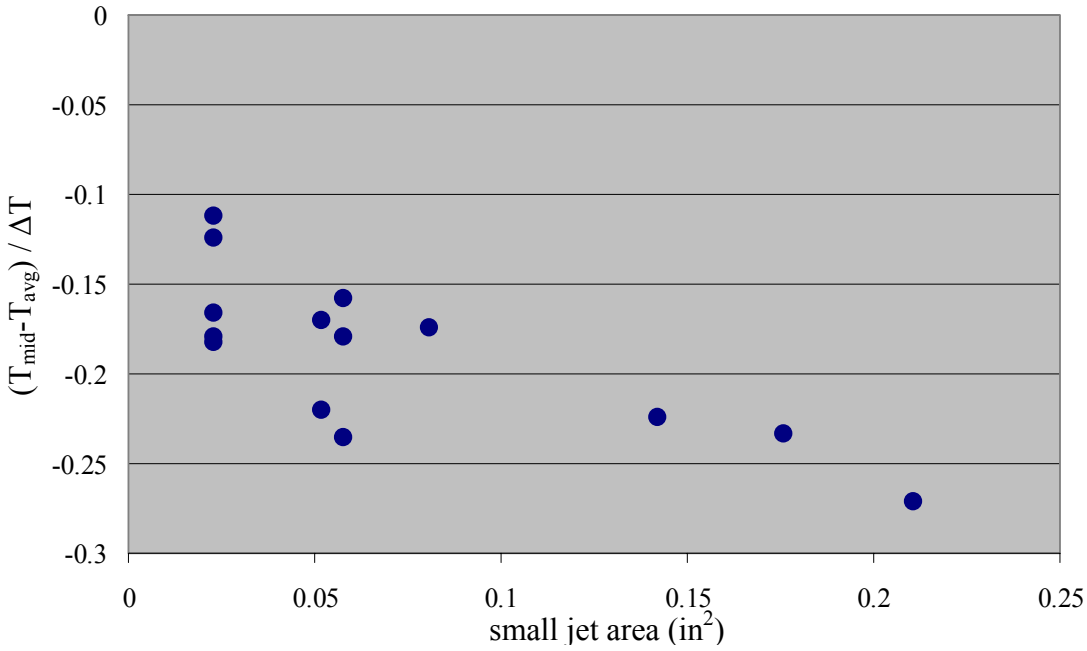

Figure 5.7: Regenerator temperature profile vs. the small end jetting area.

5.2.1.2 Boundary-layer TBT Streaming

Obvious in Figure 5.6, the temperature profiles along the TBT are drastically skewed and probably play a key factor in the heating and eventual ceasing of the alternator pistons. As the Gedeon streaming is suppressed, another type of acoustic streaming will become more apparent, that is a boundary-layer driven streaming in the Thermal Buffer Tube [79]. When Gedeon streaming is reduced, the net mass flow through the tube approaches zero but a radial dependent (over the cross-section of the TBT) mass-flux density is driven by viscous and thermal boundary layer occurrences at the tube's internal walls [18]. This streaming results in another DC heat leak away from the HHX and towards the alternators. Figure 5.8 shows the DC path of the boundary-layer TBT streaming and how heat leaks down the walls of the tube and towards the alternators.

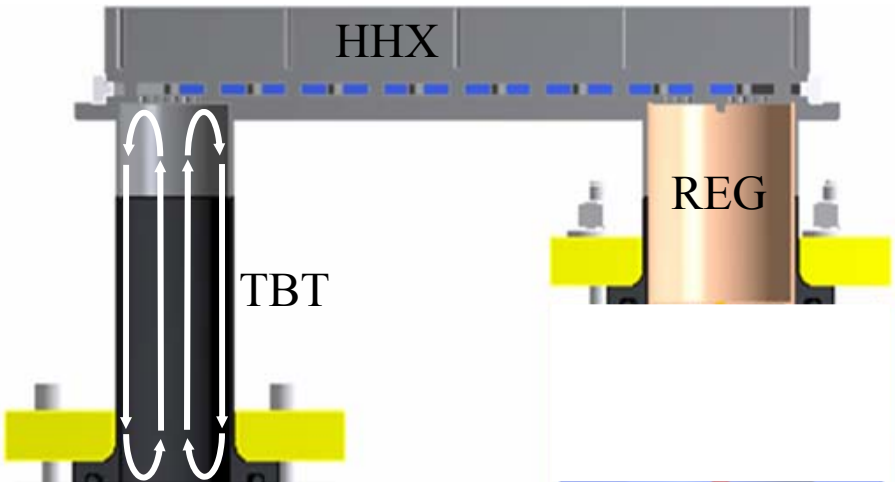

Figure 5.8: Boundary-layer TBT streaming causes a DC "annular convection roll" [13]. The radial mass-flux causes a DC enthalpy stream downward towards the alternators near the walls and upward in the middle.

5.2.1.3 Jet-Driven Streaming

Another culprit of the odd TBT temperature profiles and the eventual over-heating of the alternators is probably jet-driven streaming, which is the direct result of not having any flow straighteners at the intersection between the HHX and TBT. There are

56 0.062 inch diameter holes at this intersection and they are most likely causing the gas to jet as it flows into the TBT. This abrupt small to large diameter transition drives time-averaged-convection within the tube [80]. The spreading angle of the high speed flow that is coming into the TBT is roughly 10° [18], which actually extends through the whole TBT (remember from Section 3.3.3.1.3 that the TBT was unfortunately constrained to be only two "gas-displacement amplitudes" in length), as is shown in Figure 5.9.

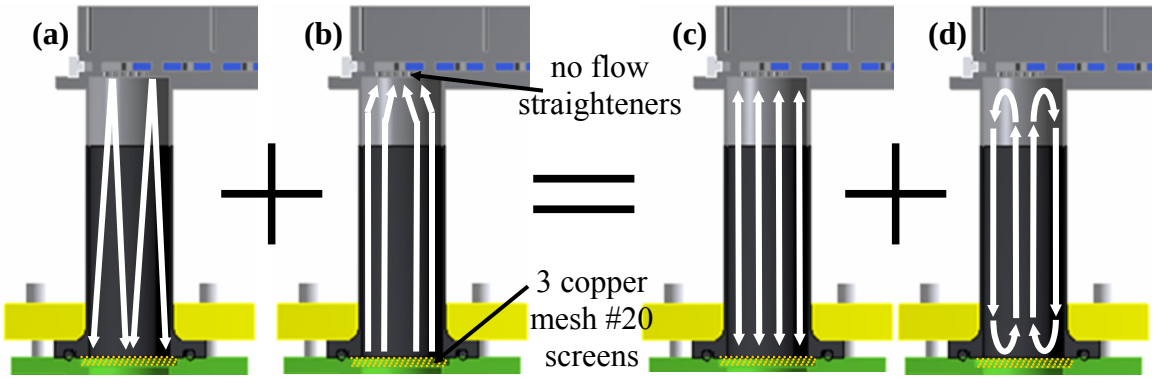

Figure 5.9: Jet-driven streaming in the TBT as described in Reference [18]. There is a flow straightener at the bottom entrance, but no straightener at the top bordering the HHX. (a) 10° spread angle of the jets leaving the HHX. (b) Broadly distributed flow profile leaving the copper mesh flow straightener screens at the interface to the Centerplate. The superposition of these profiles result in a (c) normal oscillating "plug" flow and a (d) "convection roll" like the boundary-layer driven streaming.

5.3 Performance Testing To Date

These DC heat leaks are most likely the reason why operation has not lasted longer than thirty minutes. Thus maximum power points, as a function of load resistance, have not been found to date. Eventually during steady and lasting test runs the maximum power points will be found as a function of alternator stroke. Nevertheless, the performance to date has still been very promising in terms of achieving the original goals of 100 watts and 20% efficiency.

The optimal power produced so far is 70 watts at 16.8% system efficiency (η_T). This efficiency is based on a "control volume" that only includes the TAPC system itself, in other words, the heat losses to the surroundings because of poor insulation are subtracted out. This lost heat was determined by testing how much power it took to keep the HHX at a constant 1250°F for a half-hour without kick-starting and operating the TAPC, incidentally a value of 200 watts was attained. It is then assumed that this heat lost to atmosphere remains constant during TAPC operation. Increasing the "control volume" to the room, which is simply taking the amount of power used to heat the cartridge heaters divided by the amount of power produced, results in a "hard efficiency" of 11.5%.

When the 70 watt value was achieved, the engine portion of the generator was producing 110 watts of acoustic power while the heaters were drawing 614 watts of electricity from the wall outlet. Assuming this is the heat input and subtracting out the 200 watt heat leak, the engine's efficiency (η_e) is determined to be 26.3%, a value that can be directly compared to the Carnot thermodynamic limit:

$$\eta_{Carnot} = \frac{T_{Hot} - T_{Cold}}{T_{Hot}} = \frac{950K - 320K}{950K} = 0.66, \tag{5.3}$$

where the temperatures are the hot and cold faces of the Regenerator in Kelvin. The engine's thermodynamic efficiency is 40% of the Carnot efficiency. It is noted that the exact temperatures of the hot and cold faces of the Regenerator are not exactly known, but the above is a good approximation.

5.3.1 70 Watt Test Runs

The 70 watt value is repeatedly achieved by bringing the HHX metal temperature to 1250°F prior to kick-starting; incidentally, this is probably near the temperature necessary to achieve the 1200°F internal gas temperature that the TAPC was designed

around. However, this increased initial temperature limits the test run to about twelve minutes every time, see Figure 5.10. The longer test runs (almost twenty minutes) have all occurred when the HHX was initially brought to only 1150°F, which supports the alternator piston expansion hypothesis. However, this decreased initial temperature also diminishes the initial peak power to no more than 50 watts.

Figure 5.10 also shows how quickly the initial power produced at the time of kick-starting reduces because of the alternator pistons expanding, dragging and requiring more acoustic power to translate them. The alternator peak stroke plots are also shown in Figure 5.10 in order to support this assessment. Electric power production is immediately decreasing because the piston stroke and velocity is diminishing as a result of the increased friction between the pistons' outside and the cylinders' inside respective diameters. At a constant frequency, a larger the piston stroke results in the alternator's magnet translating quicker through its copper coil and more induced voltage.

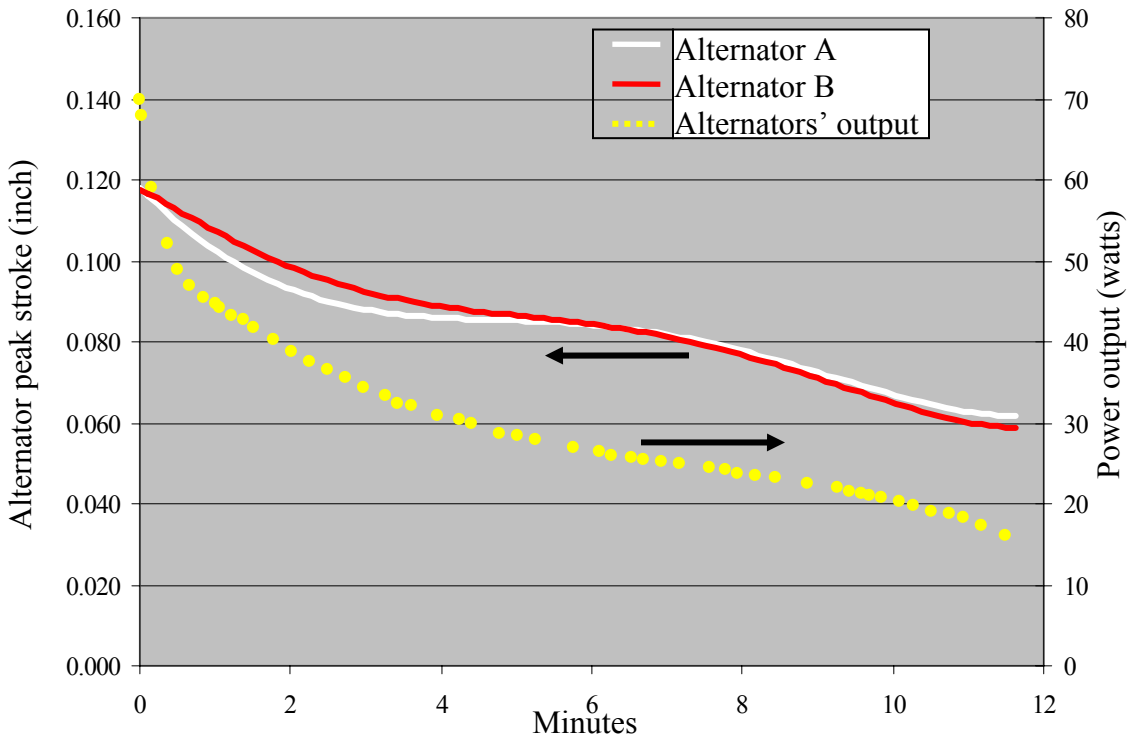

Figure 5.10: Alternator stroke and power output during a 70 watt test run. The crossing point between the two alternator stroke plots is the result of inaccuracies in the data.

Figure 5.11 shows the acoustic pressure felt in the compression space (volume in between the two alternators) by the TAPC during this same 70 watt test run. The acoustic pressure is shown to drop during the course of the test run, which incidentally follows the piston expanding assessment. The increased drag prohibits the joint engine from maintaining the same amplification of acoustic power that it produces before the piston expands. This feedbacks into the oscillating system and prevents the same pressure wave from being produced.

It might be wondered how expansion can happen so quickly (matter of seconds) when the piston and cylinder have some significant thermal mass. Before kick-starting these two components are at about 80°F, but as soon as the pistons start moving, the hot HHX helium finds its way down to the alternators. This gas is presumed to be about

300°F, so immediately the piston and cylinder expand enough to add to the static friction already in between them and effectively start to close that tight radial clearance gap.

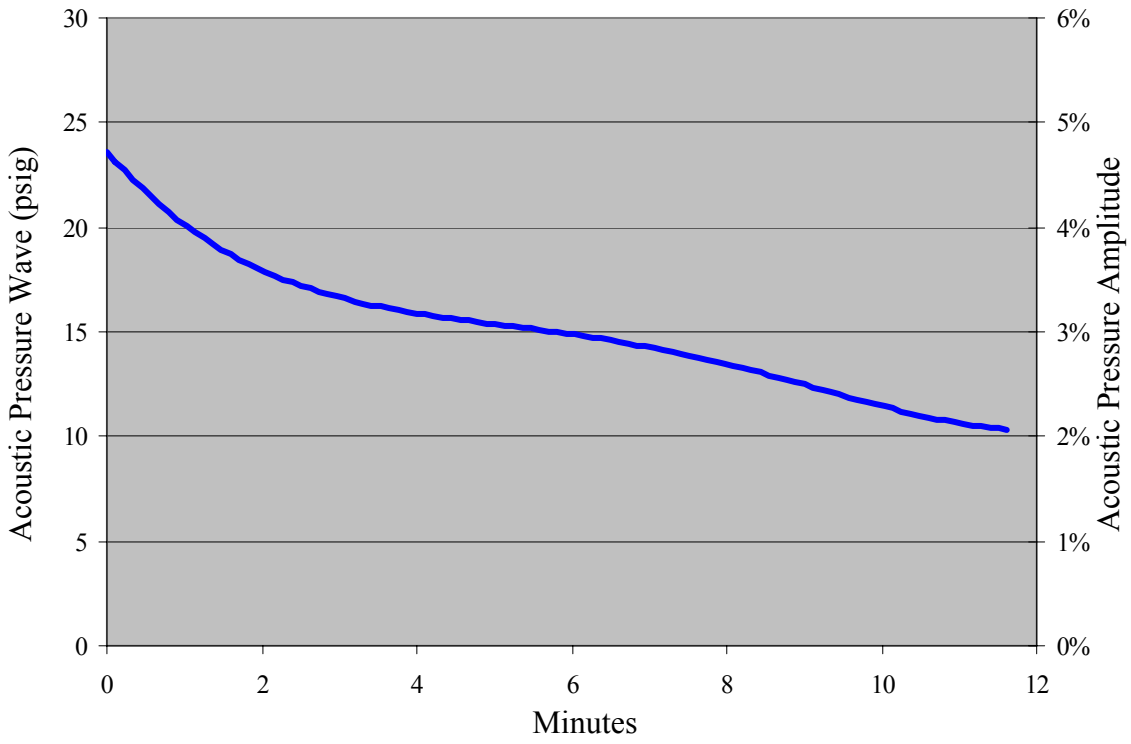

Figure 5.11: Acoustic pressure during a 70 watt test run

CHAPTER 6

CONCLUSIONS

This thesis enabled a chronological journey through all facets of the design process, including initial research, computational design, structural analysis, manufacturing, testing and troubleshooting of a thermoacoustic generator. The result is the second ever known integration of a thermoacoustic-Stirling engine with an electro-acoustic transducer that produces electricity from solely a heat input. The 70 watts output power value achieved to date actually out produces the 57 watt maximum attained by that first Northrop Grumman and Los Alamos National Lab "proof of principle" test that this work references. The other performance objective was 20% system efficiency and the TAPC has already achieved 16.8%. In terms of the "hard" efficiency (power produced divided by heater input), which doesn't take into account heat losses because of inadequate insulation, a value of 11.4% has been attained. The reference work achieved 17.8%.

The TAPC performance values to date have not achieved the original design goals; nevertheless, the statistics are still very promising. Testing in conjunction with past work and literature has pinpointed a few areas of concern. The first area is that of the rubbing alternator pistons that not only need to be kick-started, but also limit acoustic power to electric output efficiency and ultimately the power production. The second area involves the multiple DC heat leaks that are preventing continued operation and optimal alternator stroke which ultimately limits the AC electric power produced. However, it is stated with much confidence that a few relatively simple changes will facilitate the reaching and probable surpassing of the original objectives.

6.1 Recommended Work

Stated previously, the areas of concern are the rubbing pistons and the DC heat leaks. Fortunately though, these issues should be resolved relatively easily. The planned improvements include a new Jet Pump, a secondary ambient heat exchanger, Thermal Buffer Tube inlet flow straighteners, a new pair of alternators and some special thermocouple feedthrus.

6.1.1 Larger Jet Pump

The primary culprit for causing the alternators to cease is probably DC mass streaming that carries heat away from the TBT and to the compression space in between the two alternators. The Jet Pump can effectively cancel this DC flow, however test data has shown that a smaller jetting area is required in the TAPC. This will be easily accomplished by having a Jet Pump made with a larger diameter and an increased radius. In fact the Jet Pump will be sized to plug the tapered hole. Thus bottoming it out and then just opening it up ever so slightly will ensure an absolute minimum jetting area, from there the optimal point can be determined by adjusting for a linear temperature profile from the hot to cold face of the Regenerator.

6.1.2 Secondary Ambient Heat Exchanger

In order to test the idea that the Alternators were overheating, a wet cloth was wrapped around the TBT before testing and water was sprayed on it during actual operation. These simple actions actually increased the run time of the TAPC by a few minutes, which showed the necessity for a secondary ambient heat exchanger at the interface between the TBT and the Centerplate.

Currently a stack of three copper mesh screens serve as the only heat exchanger component at this interface. In order to address this, a square copper flange like component is being designed that will wedge in between the TBT loose type flange and

the Centerplate. Drilled through this component will be four pathways perpendicular to the bolt circle holes. One corner will serve as a chilled water inlet, another as the outlet and the remaining two will be plugged. The result will be a copper flange that fits around the TBT lap, with a water path in from one side and out the other. This cooled component will then conduct heat out of both the bottom of the TBT and the top of the Centerplate.

6.1.3 Flow Straighteners

One of the issues that is allowing the alternator pistons to see more heat than they can handle is that of jet driven streaming in the TBT. Typically flow straighteners should be used in a TBT whenever a jet reaches two gas displacement amplitudes or more into it [18]. Ironically this is the exact length of the TBT in the TAPC. In order to address this, a couple mesh #20 stainless steel screens will be spot welded to the HHX at the interface to the TBT.

6.1.4 New Alternators

The alternators currently installed in the TAPC were damaged during the initial shakedown testing as they have over-stroke on numerous occasions. Even though they have been very robust, their performance has definitely decreased over time. One alternator drags too much and probably can be blamed for the system not being able to self-start. While the other has a relatively large clearance gap, and its equilibrium point actually drifts inward $1/8^{th}$ of an inch during testing. In other words, it has the same peak-to-peak stroke as the other alternator, but cycles around a skewed zero point. Fortunately the linear alternators used in this work are a cheap off the shelf component, thus brand new alternators have been ordered and will be used during further performance testing.

6.1.5 Internal Thermocouples

So far every temperature acquired is only an exterior metal temperature, which can be used to monitor for safety measures, yet it isn't accurate enough to truly understand the performance of the TAPC. The biggest "bug" learnt during shakedown testing has been the supposed over-heating of the alternator pistons. However, the temperature inside has only been a guess based on the Centerplate's 140°F and Inertance Tube's 90°F exterior temperatures when the system shuts down. Besides in the compression space, internal temperatures of the HHX and TBT will further help diagnostics. In order to get away from this guessing of internal gas temperatures, a special thermocouple feedthru has been designed. This component will seal to the piezoelectric pressure transducer ports, which at the current testing stage serve no purpose.

APPENDIX A

DELTAE INPUT/OUTPUT FILE

```
TITLE     TAPC
!->TAPC
!Created@16:39:59 13-Mar-06 with DeltaE Vers. 5.3b5 for the IBM/PC-Compatible
!--------------------------------  0 --------------------------------
 BEGIN      the setup
  3.1000E+06 a Mean P    Pa          102.41    A Freq.  G(  0b)     P
  102.41     b Freq.     Hz      G   323.86    B T-beg  G(  0c)     P
  323.86     c T-beg     K       G   3.2537E+05 C  |p|   G(  0d)     P
  3.2537E+05 d  |p|      Pa      G   2.9526E+08 D Re(Zb) G(  1a)     P
  0.0000  e Ph(p)     deg             2.2871E+07 E Im(Zb) G(  1b)     P
  0.0000  f  |U|     m^3/s            1.5460E-05 F AreaF  G(  2d)     P
  0.0000  g Ph(U)     deg             -235.16    G HeatIn G(  8e)     P
                                       493.46    H HeatIn G( 17e)     P
                                      5.6796E+09 I Re(Zb) G( 37a)     P
                                      -1.2879E+08 J Im(Zb) G( 37b)     P
 helium     Gas type                 0.7676  K  |I|   G( 42h)     P
 ideal      Solid type               -95.906   L Ph(I)  G( 42i)     P
!--------------------------------  1 --------------------------------
 TBRANCH    Split to thermodynamic sections
  2.9526E+08 a Re(Zb) Pa-s/m^3   G  3.2537E+05 A |p|       Pa
  2.2871E+07 b Im(Zb) Pa-s/m^3   G  0.0000  B Ph(p)     deg
                                      1.0987E-03 C |U|     m^3/s
                                      -4.4293  D Ph(U)     deg
                                      178.21    E Hdot      W
 helium     Gas type                 178.21    F Edot      W
 ideal      Solid type               -178.21    G Edot_T    W
!--------------------------------  2 --------------------------------
 CONE       Jet pump
  1.5485E-04 a AreaI     m^2         3.2500E+05 A |p|       Pa
  0.1396  b PerimI     m             -4.1541E-02 B Ph(p)     deg
  4.7752E-03 c Length     m          1.0988E-03 C |U|     m^3/s
  1.5460E-05 d AreaF     m^2     G   -5.2721  D Ph(U)     deg
  0.1396  e PerimF     m             177.81    E Hdot      W
  5.0000E-04 f Srough                177.81    F Edot      W
 helium     Gas type                 -0.4023  G HeatIn    W
 stainless  Solid type
!--------------------------------  3 --------------------------------
 RPNTARGET  Calc JP minor loss resistor
  1.0000  a Target          (t)          4.4955E+06 A RPNval
  2 rho * 3 / pi / 2C * 2d / 2d / 3a *
```

```
!---------------------------------  4 ---------------------------------
 IMPEDANCE  JP minor loss resistor
 sameas   3A a Re(Zs) Pa-s/m^3        3.2008E+05 A |p|       Pa
 0.0000  b Im(Zs) Pa-s/m^3            3.9067E-02 B Ph(p)     deg
                                      1.0988E-03 C |U|     m^3/s
                                      -5.2721  D Ph(U)     deg
                                      175.09    E Hdot      W
 helium     Gas type                  175.09    F Edot      W
 ideal      Solid type                -2.7137  G HeatIn     W
!---------------------------------  5 ---------------------------------
 RPNTARGET  dp20 generated by the JP
  0.9000  a Target          (t)       2618.7     A RPNval
  rho 2C * 2C * 2d / 2d / 8 / 5a *
!---------------------------------  6 ---------------------------------
 COMPLIANCE Jet pump gap
  1.7418E-03 a SurfAr    m^2         3.2008E+05 A |p|       Pa
  1.2569E-06 b Volum     m^3         3.9067E-02 B Ph(p)     deg
                                      1.1012E-03 C |U|     m^3/s
                                      -7.8846  D Ph(U)     deg
                                      174.56    E Hdot      W
 helium     Gas type                  174.56    F Edot      W
 stainless  Solid type                -0.5313  G HeatIn     W
!---------------------------------  7 ---------------------------------
 RPNTARGET  Xpp in main ambient HX
 0.0000  a Target          (t)       0.7148  A RPNval
  2 U1 mag * w / 8a / 8b / 8c /
!---------------------------------  8 ---------------------------------
 TX         Main ambient HX
  7.9173E-04 a Area      m^2         3.1997E+05 A |p|       Pa
  0.3175  b GasA/A                   -8.8095E-03 B Ph(p)     deg
  1.9050E-02 c Length     m          1.1305E-03 C |U|     m^3/s
  7.9375E-04 d radius     m          -18.844   D Ph(U)     deg
  -235.16    e HeatIn     W      G   -60.598   E Hdot      W
  300.00     f Est-T      K   =  8H? 171.18    F Edot      W
 helium     Gas type                  -235.16    G Heat      W
 copper     Solid type                300.00    H MetalT     K
!---------------------------------  9 ---------------------------------
 STKDUCT    Ambient gap
 sameas   8a a Area      m^2         3.1997E+05 A |p|       Pa
  9.9746E-02 b Perim      m          -9.9537E-03 B Ph(p)     deg
  1.5875E-03 c Length     m          1.1475E-03 C |U|     m^3/s
    1.0000  d WallA     m^2          -21.231   D Ph(U)     deg
                                      -60.598   E Hdot      W
                                      171.13    F Edot      W
                                      323.86    G T-beg      K
 helium     Gas type                  323.88    H T-end      K
```

```
 stainless  Solid type                    -4.8253E-02 I StkEdt     W
!---------------------------------- 10 ----------------------------------
 STKSCREEN  regenerator
 sameas   8a a Area      m^2              2.9532E+05 A |p|       Pa
  0.7460  b VolPor                        4.7547  B Ph(p)     deg
  3.8100E-02 c Length     m               4.3954E-03 C |U|     m^3/s
  3.3500E-05 d   r_H      m               -50.621   D Ph(U)     deg
  0.2500  e KsFrac                        -60.598   E Hdot      W
                                          368.77    F Edot      W
                                          323.88    G T-beg     K
 helium     Gas type                     875.00    H T-end     K
 stainless  Solid type                   197.64    I StkEdt     W
!---------------------------------- 11 ----------------------------------
 RPNTARGET  regen hot end temp
  875.00    a Target         = 11A?      875.00    A RPNval
  10H
!---------------------------------- 12 ----------------------------------
 RPNTARGET  a = dp20 ignorage factor; A = tau factor in dp20 req
   3.0000  a Target           (t)         23.530   A RPNval
  10H 10G / 2.68 ^ 1 - 10H 10G / 1 - / 12a *
!---------------------------------- 13 ----------------------------------
 RPNTARGET  a = mu_cold; A = dp20 req
 sameas   5A a Target         = 13A?     2618.7     A RPNval
  6 2.1e-5 * 10c * 2.68 / 10a / 10d / 10d / 0a / 12A * 9F *
!---------------------------------- 14 ----------------------------------
 STKDUCT    Hot end gap
 sameas   8a a Area      m^2              2.9531E+05 A |p|       Pa
 9.9700E-02 b Perim      m               4.7536  B Ph(p)     deg
 1.5800E-03 c Length     m               4.4335E-03 C |U|     m^3/s
 1.0000  d WallA     m^2                 -50.971   D Ph(U)     deg
                                         -60.598   E Hdot      W
                                         368.67    F Edot      W
                                         875.00    G T-beg     K
 helium     Gas type                     875.03    H T-end     K
 stainless  Solid type                   -9.6718E-02 I StkEdt     W
!---------------------------------- 15 ----------------------------------
 STKDUCT    Holes thru bottom plate over regen
  2.3700E-04 a Area      m^2             2.9527E+05 A |p|       Pa
  0.5980  b Perim      m                 4.7520  B Ph(p)     deg
  1.5800E-03 c Length     m              4.4465E-03 C |U|     m^3/s
  1.0000  d WallA     m^2                -51.133   D Ph(U)     deg
                                         -60.598   E Hdot      W
                                         368.17    F Edot      W
                                         875.03    G T-beg     K
 helium     Gas type                     875.04    H T-end     K
 stainless  Solid type                   -0.4994  I StkEdt     W
```

```
!---------------------------------- 16 ----------------------------------
 RPNTARGET  Xpp in HHX / HHX length
  0.0000  a Target          (t)             0.9030  A RPNval
  2 U1 mag * w / 17a / 17b / 17c /
!---------------------------------- 17 ----------------------------------
 PX        Flat plate hot HX (area and r_h can be modified to suit)
  1.2100E-04 a Area      m^2              2.8867E+05 A |p|       Pa
  0.8300  b VolPor                        3.9394  B Ph(p)     deg
  0.1524  c Length     m                  4.9142E-03 C |U|     m^3/s
  3.6900E-03 d   r_H      m               -54.833   D Ph(U)     deg
  493.46    e HeatIn     W      G         432.86    E Hdot      W
  24.000    f f_con                      367.72    F Edot      W
  1.0000  g f_exp                        493.46    G Heat      W
  6.0000  h h_con                        1097.3     H MetalT     K
  1.0000  i h_exp           (t)
  925.00    j Est-T      K
 helium     Gas type
 nickel     Solid type
!---------------------------------- 18 ----------------------------------
 STKDUCT    Holes thru bottom plate over TBT
  2.3700E-04 a Area      m^2              2.8862E+05 A |p|       Pa
  0.5980  b Perim      m                  3.9381  B Ph(p)     deg
  1.5800E-03 c Length     m               4.9275E-03 C |U|     m^3/s
  1.0000  d WallA      m^2                -54.968   D Ph(U)     deg
                                          432.86    E Hdot      W
                                          367.24    F Edot      W
                                          875.04    G T-beg      K
 helium     Gas type                     875.00    H T-end      K
 stainless  Solid type                   -0.4836  I StkEdt     W
!---------------------------------- 19 ----------------------------------
 STKDUCT    Thermal buffer tube
  5.0700E-04 a Area      m^2     S= -2 2.8723E+05 A |p|       Pa
  7.9689E-02 b Perim      m    Fn( 19a)  3.8017  B Ph(p)     deg
  7.6200E-02 c Length     m               6.1075E-03 C |U|     m^3/s
  6.6500E-05 d WallA      m^2             -61.381   D Ph(U)     deg
                                          432.86    E Hdot      W
                                          368.16    F Edot      W
                                          875.00    G T-beg      K
 helium     Gas type                     323.86    H T-end      K
 stainless  Solid type                   0.9176  I StkEdt     W
!---------------------------------- 20 ----------------------------------
 RPNTARGET  Xpp in TBT / TBT length
  0.0000  a Target          (t)             2.0351  A RPNval
  19C 19C + 2 / 2 * w / 19a / 19c / -1 ^
!---------------------------------- 21 ----------------------------------
 RPNTARGET  Fix TBT ambient end temperature
```

```
 sameas   0c a Target         = 21A?    323.86    A RPNval
  19H
!---------------------------------- 22 ----------------------------------
 TX        Dummy HX to close the thermodynamic section (heat to alt)
 sameas   8a a Area      m^2              2.8723E+05 A |p|       Pa
  1.0000  b GasA/A                        3.8015  B Ph(p)     deg
  1.0000E-04 c Length     m               6.1102E-03 C |U|     m^3/s
  1.0000E-03 d radius     m               -61.395   D Ph(U)     deg
  0.0000  e HeatIn     W                  368.12    E Hdot      W
  300.00    f Est-T      K      (t)       368.12    F Edot      W
 helium     Gas type                     -64.742   G Heat      W
 ideal      Solid type                   -43.401   H MetalT     K
!---------------------------------- 23 ----------------------------------
 DUCT       Bore to compression space
  4.4500E-04 a Area      m^2     S= -2 2.8435E+05 A |p|       Pa
  7.4733E-02 b Perim      m    Fn( 23a) 3.5651  B Ph(p)     deg
  6.9850E-02 c Length     m               7.1340E-03 C |U|     m^3/s
  5.0000E-04 d Srough                     -65.238   D Ph(U)     deg
                                          366.74    E Hdot      W
 helium     Gas type                     366.74    F Edot      W
 stainless  Solid type                   -1.3739  G HeatIn    W
!---------------------------------- 24 ----------------------------------
 RPNTARGET  Calc minor loss R
  1.2000  a Target          (t)           4.2274E+04 A RPNval
  2 rho * 3 / pi / 23C * 23a / 23a / 24a *
!---------------------------------- 25 ----------------------------------
 IMPEDANCE  Minor loss resistor
 sameas  24A a Re(Zs) Pa-s/m^3           2.8424E+05 A |p|       Pa
 0.0000  b Im(Zs) Pa-s/m^3               3.6217  B Ph(p)     deg
                                         7.1340E-03 C |U|     m^3/s
                                         -65.238   D Ph(U)     deg
                                         365.67    E Hdot      W
 helium     Gas type                     365.67    F Edot      W
 ideal      Solid type                   -1.0758  G HeatIn    W
!---------------------------------- 26 ----------------------------------
 SOFTEND    End of thermodynamic section
    0.0000  a Re(z)          (t)         2.8424E+05 A |p|       Pa
    0.0000  b Im(z)          (t)         3.6217  B Ph(p)     deg
                                         7.1340E-03 C |U|     m^3/s
                                         -65.238   D Ph(U)     deg
                                         365.67    E Hdot      W
                                         365.67    F Edot      W
                                         1.3105  G Re(z)
 helium     Gas type                     3.3891  H Im(z)
 ideal      Solid type                   323.86    I   T       K
!---------------------------------- 27 ----------------------------------
```

```
COMPLIANCE Space above JP
 1.3478E-03 a SurfAr    m^2          3.2537E+05 A |p|      Pa
 1.7234E-06 b Volum     m^3          0.0000  B Ph(p)     deg
                                     1.0981E-03 C |U|     m^3/s
                                     179.22    D Ph(U)     deg
                                     -178.63    E Hdot      W
 helium     Gas type                 -178.63    F Edot      W
 stainless  Solid type               -0.4248  G HeatIn    W
!---------------------------------- 28 ----------------------------------
 COMPLIANCE compliance tank
 7.4600E-03 a SurfAr    m^2          3.2537E+05 A |p|      Pa
 4.9420E-05 b Volum     m^3          0.0000  B Ph(p)     deg
                                     2.2777E-03 C |U|     m^3/s
                                     -119.24    D Ph(U)     deg
                                     -180.99    E Hdot      W
 helium     Gas type                 -180.99    F Edot      W
 stainless  Solid type               -2.3512  G HeatIn    W
!---------------------------------- 29 ----------------------------------
 DUCT       Inertance line
 1.0680E-04 a Area      m^2     S= -2 2.8926E+05 A |p|      Pa
 3.6643E-02 b Perim     m    Fn( 29a) 3.0553  B Ph(p)     deg
 0.4500  c Length     m              4.0467E-03 C |U|     m^3/s
 5.0000E-04 d Srough                 -106.01    D Ph(U)     deg
                                     -191.14    E Hdot      W
 helium     Gas type                 -191.14    F Edot      W
 stainless  Solid type               -10.159   G HeatIn    W
!---------------------------------- 30 ----------------------------------
 DUCT       Bore to the compression space
 1.5610E-04 a Area      m^2          2.8395E+05 A |p|      Pa
 4.4300E-02 b Perim     m             3.4407  B Ph(p)     deg
 6.9850E-02 c Length     m           4.4262E-03 C |U|     m^3/s
 5.0000E-04 d Srough                 -104.41    D Ph(U)     deg
                                     -192.63    E Hdot      W
 helium     Gas type                 -192.63    F Edot      W
 stainless  Solid type               -1.4856  G HeatIn    W
!---------------------------------- 31 ----------------------------------
 RPNTARGET  Calc minor loss R
 1.2000  a Target          (t)          2.1315E+05 A RPNval
 2 rho * 3 / pi / 30C * 30a / 30a / 31a *
!---------------------------------- 32 ----------------------------------
 IMPEDANCE  Minor loss resistor
 sameas  31A a Re(Zs) Pa-s/m^3       2.8424E+05 A |p|      Pa
    0.0000  b Im(Zs) Pa-s/m^3        3.6217  B Ph(p)     deg
                                     4.4262E-03 C |U|     m^3/s
                                     -104.41    D Ph(U)     deg
                                     -194.72    E Hdot      W
```

```
 helium     Gas type                    -194.72    F Edot      W
 ideal      Solid type                  -2.0880  G HeatIn    W
!-------------------------------- 33 --------------------------------
 UNION      rejoin in the two branches in the alternator
  26.000   a TendSg                     2.8424E+05 A |p|       Pa
  2.8424E+05 b |p|End    Pa    = 33A?3.6217  B Ph(p)     deg
  3.6217  c Ph(p)E    deg   = 33B?      1.0929E-02 C |U|     m^3/s
                                       -80.059   D Ph(U)     deg
                                       170.95    E Hdot      W
 helium     Gas type                    170.95    F Edot      W
 ideal      Solid type                  323.86    G End-T     K
!-------------------------------- 34 --------------------------------
 COMPLIANCE Compression space
  8.8400E-03 a SurfAr    m^2          2.8424E+05 A |p|       Pa
  6.0800E-05 b Volum     m^3          3.6217  B Ph(p)     deg
                                       1.3069E-02 C |U|     m^3/s
                                       -81.163   D Ph(U)     deg
                                       168.82    E Hdot      W
 helium     Gas type                    168.82    F Edot      W
 stainless  Solid type                  -2.1262  G HeatIn    W
!-------------------------------- 35 --------------------------------
 RPNTARGET  Calculate local Z
 0.0000  a Target          (t)          4.3318E+07 A RPNval
                                       3.9537E+06 B RPNval
  2 p1 * U1 / real 2 p1 * U1 / imag
!-------------------------------- 36 --------------------------------
 BRANCH     branch to mirror image alternator 1/2
 sameas  35B a Re(Zb) Pa-s/m^3       2.8424E+05 A |p|       Pa
 sameas  35A b Im(Zb) Pa-s/m^3       3.6217  B Ph(p)     deg
                                       6.5345E-03 C |U|     m^3/s
                                       -81.163   D Ph(U)     deg
                                       84.412   E Hdot      W
 helium     Gas type                    84.412   F Edot      W
 ideal      Solid type                  84.412   G Edot_B    W
!-------------------------------- 37 --------------------------------
 TBRANCH    Split to seal leakage path
  5.6796E+09 a Re(Zb) Pa-s/m^3   G 2.8424E+05 A |p|       Pa
 -1.2879E+08 b Im(Zb) Pa-s/m^3   G 3.6217  B Ph(p)     deg
                                       5.0033E-05 C |U|     m^3/s
                                       4.9208  D Ph(U)     deg
                                       7.1088  E Hdot      W
 helium     Gas type                    7.1088  F Edot      W
 ideal      Solid type                  77.303   G Edot_T    W
!-------------------------------- 38 --------------------------------
 RPNTARGET  piston seal gap
  1.5000E-05 a Target          (t)        0.0000  A RPNval
```

```
 0
!-------------------------------- 39 --------------------------------
 RPNTARGET  Seal length and seal R
  1.5875E-02 a Target          (t)        7.4226E+09 A RPNval
  6 39a * 38a 3 ^ / pi 42a * sqrt / mu *
!-------------------------------- 40 --------------------------------
 IMPEDANCE  Seal resistance
 sameas  39A a Re(Zs) Pa-s/m^3       8.7444E+04 A |p|      Pa
 0.0000  b Im(Zs) Pa-s/m^3           -170.85    B Ph(p)    deg
                                     5.0033E-05 C |U|    m^3/s
                                     4.9208  D Ph(U)    deg
                                     -2.1816  E Hdot     W
 helium     Gas type                 -2.1816  F Edot     W
 stainless  Solid type               -9.2904  G HeatIn   W
!-------------------------------- 41 --------------------------------
 SOFTEND    end of seal leakage
    0.0000  a Re(z)          (t)     8.7444E+04 A |p|      Pa
    0.0000  b Im(z)          (t)     -170.85    B Ph(p)    deg
                                     5.0033E-05 C |U|    m^3/s
                                     4.9208  D Ph(U)    deg
                                     -2.1816  E Hdot     W
                                     -2.1816  F Edot     W
                                     -3157.8    G Re(z)
 helium     Gas type                 -233.34    H Im(z)
 ideal      Solid type               323.86   I  T      K
!-------------------------------- 42 --------------------------------
 IESPEAKER  CFIC D102
  2.0300E-03 a Area      m^2         8.7444E+04 A |p|      Pa
  7.8000  b   R      ohms            -170.85    B Ph(p)    deg
  8.4000E-02 c L         H           6.5310E-03 C |U|    m^3/s
  52.300   d BLprod   T-m            -81.622   D Ph(U)    deg
  0.4480  e   M      kg              3.8312  E Hdot     W
  3.3000E+04 f   K      N/m          3.8312  F Edot     W
  2.0000  g   Rm   N-s/m             -60.289   G WorkIn   W
  0.7676  h  |I|     A        G      157.08    H Volts    V
  -95.906   i Ph(I)   deg       G    0.7676  I Amps     A
                                     180.00    J Ph(Ze)   deg
                                     3.7137E+05 K  |Px|    Pa
 helium     Gas type                 -175.08    L Ph(Px)   deg
 stainless  Solid type               -13.183   M HeatIn   W
!-------------------------------- 43 --------------------------------
 RPNTARGET  Force electrical load resistive
  180.00    a Target         = 43A?    180.00    A RPNval
  42J
!-------------------------------- 44 --------------------------------
 RPNTARGET  piston peak stroke
```

```
 5.0000E-03 a Target          = 44A?   5.0000E-03 A RPNval
 42C 42a / w /
!---------------------------------- 45 ----------------------------------
 UNION      rejoin seal leakage path
 41.000   a TendSg                     8.7444E+04 A |p|       Pa
 8.7444E+04 b |p|End    Pa    = 45A? -170.85    B Ph(p)     deg
 -170.85    c Ph(p)E    deg   = 45B?   6.5342E-03 C |U|     m^3/s
                                      -81.184   D Ph(U)     deg
                                      1.6496  E Hdot      W
 helium     Gas type                  1.6496  F Edot      W
 ideal      Solid type                323.86    G End-T     K
!---------------------------------- 46 ----------------------------------
 COMPLIANCE back volume
  7.2457E-02 a SurfAr    m^2          8.7444E+04 A |p|       Pa
  6.0000E-04 b Volum     m^3          -170.85    B Ph(p)     deg
                                      3.7532E-09 C |U|     m^3/s
                                      -151.49    D Ph(U)     deg
                                      1.5482E-04 E Hdot      W
 helium     Gas type                  1.5482E-04 F Edot      W
 stainless  Solid type                -1.6494  G HeatIn    W
!---------------------------------- 47 ----------------------------------
 HARDEND    stop
 0.0000  a R(1/z)         = 47G?      8.7444E+04 A |p|       Pa
 0.0000  b I(1/z)         = 47H?      -170.85    B Ph(p)     deg
                                      3.7532E-09 C |U|     m^3/s
                                      -151.49    D Ph(U)     deg
                                      1.5482E-04 E Hdot      W
                                      1.5482E-04 F Edot      W
                                      2.7269E-09 G R(1/z)
 helium     Gas type                  9.5824E-10 H I(1/z)
 stainless  Solid type                323.86    I   T       K
!---------------------------------- 48 ----------------------------------
 RPNTARGET  Efficiency estimate
  0.0000  a Target           (t)      0.2444  A RPNval
  42G -2 * 17G /
! The restart information below was generated by a previous run
! You may wish to delete this information before starting a run
! where you will (interactively) specify a different iteration
! mode.  Edit this table only if you really know your model!
guessz    0b 0c 0d 1a 1b 2d 8e 17e 37a 37b 42h 42i
xprecn  -1.8896E-03 -2.1903E-03     4.7484   3374.8       416.79    -2.7357E-10 -2.9525E-
04 -1.6172E-03  2.5691E+04 -3777.5      2.3085E-05 -2.5920E-04
hilite    48A
targs     8f 11a 13a 21a 33b 33c 43a 44a 45b 45c 47a 47b
SPECIALS    3  19 -2  23 -2  29 -2
```

APPENDIX B

PRESSURE VESSEL ANALYSIS

The Thermoacoustic Power Converter's operating gas is Grade 5.0 helium at a maximum pressure and temperature (location dependent) of 500 psig and 1200°F respectively. This test section is designed to be consistent with the ASME Boiler and Pressure Vessel Code [4]. The following analysis uses this code to develop the basis for a pressure vessel safety test and further determines the pressure withstanding capability of every TAPC component.

B.1 Materials

The majority of the TAPC's pressure vessel will be at ambient temperatures during operation, yet the Hot Heat Exchanger is brought to 1200°F with cartridge heaters in order to heat the gas internal to it. Therefore this heat exchanger and its adjacent components of the Thermodynamic Section are made out of a material that can withstand this temperature without losing the required strength at the 500 psig maximum internal pressure. The material chosen is a nickel based alloy, Inconel 625.

Reference [4] specifies two grades of this material (Table B.1), with Grade 2 having the better strength at the high temperature condition. Grade 2 can be achieved by heat treating and solution annealing the Grade 1 version. This was accomplished by heating a Grade 1 piece to 2000°F for four hours and subsequently rapidly cooled (forced convection with a fan). Tensile and bend tests (based on specified test and qualification standards [81]) were performed on welded coupons of the Grade 1 and the Grade 2 Inconel (Figure B.1). Table B.2 summarizes the average yield strengths, ultimate tensile

strengths and elongations for the Inconel 625 tensile test samples before and after the solution annealing heat treatment.

Table B.1: Allowable stresses of the materials that make up the TAPC [4]

Material	UNS No.	Grade/ Type	Spec. No.	Allowable Stress (ksi) 120°F	Allowable Stress (ksi) 1200°F	Minimum Tensile Strength (ksi)	Minimum Yield Strength (ksi)
Inconel	N06625	1	SB-446	34.3	13.2	110	50
Inconel	N06625	2	SB-446	26.7	19.3	100	40
Stainless Steel	S30400	304	SA-479	20.0	-	75	30
Stainless Steel (Bolts)	S30400	B8	SA-320	25.0	-	125	100
Copper	C10200	-	SB-187	5.0	-	28	8
Alloy Steel (Bolts)	G41400	4140 (A574)	SA-574	35.0	-	180	140

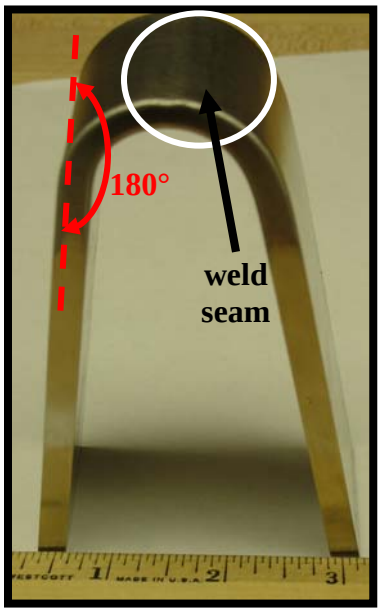

Figure B.1: Post bend test sample. Multiple 180° bend tests were performed in accordance with and qualified per Reference [81] on welded samples of the Grade 2 Inconel. Both sides of the weld saw strain by bending different samples in each of the two directions.

Table B.2: Inconel 625 pre and post heat treatment tensile data (at room temp)

Condition	0.2% Yield (ksi)	UTS (ksi)	Elongation (%)
Grade 1	74.0	120.9	63.5
Grade 2	97.4	116.0	75.0

The components in the Acoustic Section of the TAPC, Figure 3.5(b), are not subjected to the hot temperature; values at or below 120°F are expected, thus these parts can be made out of Type 304 stainless steel. Oxygen-free copper was chosen for the material of the ambient heat exchanger (Section 3.3.3.1.4) in order to promote thermal conductivity. Finally, high strength Alloy 4140 fasteners were chosen for the flange bolts. These materials, with their respective Reference [4] allowable stresses, are also summarized in Table B.1

B.2 Hydrostatic Pressure Test

The TAPC pressure vessel was hydrostatically tested per UG-99 of Reference [4] after the assembly. As described in the reference, the test pressure shall be equal to at least 1.3 times the maximum allowable working pressure multiplied by the ratio of the allowable stress at the hydrostatic test pressure to the design pressure. It is noted that the lowest allowable stress ratio is used when more than one material make up the pressure vessel. Hence the allowable stress of stainless steel, rather than Inconel 625, is used in this calculation for the design stress because it results in a lower ratio.

B.2.1 Hydrostatic test pressure calculation

P_{design} = design pressure
P_{test} = hydrostatic test pressure
S_{design} = allowable stress in stainless steel design temperature
S_{test} = allowable stress in stainless steel at test temperature
W = total bolt load

$$P_{design} := 500\frac{lb}{in^2} \qquad S_{design} := 20.0 \cdot 10^3 \frac{lb}{in^2} \qquad S_{test} := 20.0 \cdot 10^3 \frac{lb}{in^2}$$

$$P_{test} := 1.3 \cdot 500\frac{lb}{in^2} \cdot \frac{S_{design}}{S_{test}} \qquad P_{test} = 650\frac{lb}{in^2}$$

This calculation defines a hydrostatic test pressure of at least 650 psig.

The pressure vessel can safely maintain the minimum of the maximum pressures determined in the Section B.4 Analysis. These values are summarized below in Table B.3 and the limiting maximum pressure is highlighted. In summary, Reference [4] requires a hydrostatic test pressure of 650 psig, while the pressure vessel can actually maintain a 911 psig maximum. Nevertheless, a hydrostatic test of 750 psig (1½ times the 500 psig design pressure) was performed as an extra safety confirmation.

Safety was the reason why a hydrostatic pressure test, rather than pneumatic, was used because if failure occurred there would be some water leakage rather than parts being blown off the vessel. Figure B.2 shows the TAPC ready for this 750 psig hydrostatic test. During this pressure withstanding confirmation, all of the sensor ports were plugged, it was then filled with water through the large LVDT hole, afterwards this hole was plugged and it was then pumped with water to 750 psig through the Centerplate helium port. The test procedure required that it remain at or above this pressure for ten minutes without failure, which it did with no problem. It is noted that leakage through the sealed sensor ports during testing was allowed as long as water was constantly replaced to maintain the 750 psig target.

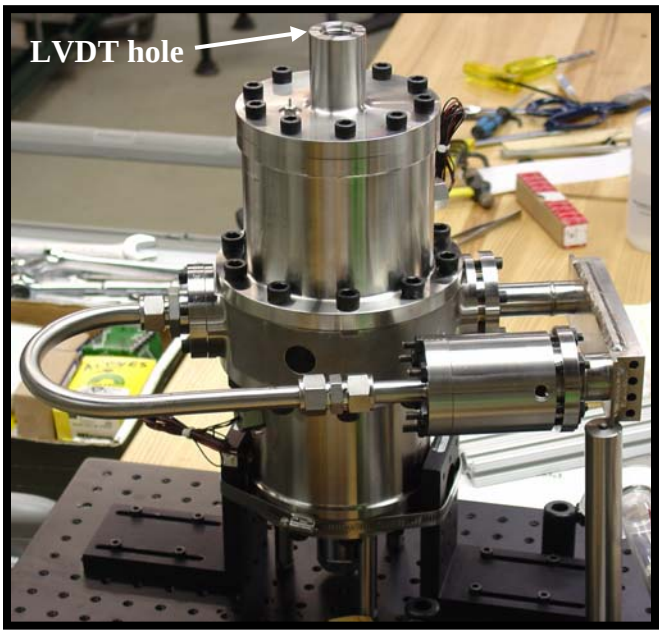

Figure B.2: TAPC assembled, secured and ready for the hydrostatic pressure test. It was mounted in this position in order to utilize the large LVDT entry hole for filling with water.

Table B.3: Maximum pressure by calculation

Calculation Section	Maximum Pressure (psig)
B.4.2 Stayed plate thickness	2,959
B.4.3 Hot Heat Exchanger plug fillet welds	17,540
B.4.4 Thermal Buffer Tube wall	2,080
B.4.4 Regenerator tube wall	1,548
B.4.5 Thermal Buffer Tube loose type lap joint flange	2,485
B.4.5 Regenerator loose type lap joint flange	2,000
B.4.6 Ambient Heat Exchanger wall thickness	3,061
B.4.6 Ambient Heat Exchanger water jacket shell	10,100
B.4.7 Compliance volume shell thickness	8,386
B.4.7 Compliance flange	3,250
B.4.8 Inertance Tube wall thickness	4,662
B.4.9 Centerplate flange assembly	1,440
B.4.9 Centerplate bores	6,986
B.4.10 Alternator Vessel flange	1,000
B.4.10 Alternator Vessel wall thickness	4,710
B.4.10 Alternator Vessel rear blind flange	911

B.3 Pressure Containment

B.3.1 Fill System

Prior to charging the TAPC to its mean operating pressure of 450 psig, it must be initially evacuated; a few evacuations and charging cycles will be performed in order to ensure helium purity in the TAPC. The molecule of helium is extremely small and can find its way out of the smallest of cracks resulting from imperfect face seals between the flanges or Swagelok fittings. In order to locate these leakage points a Helium Leak Detector [82] was used with much success.

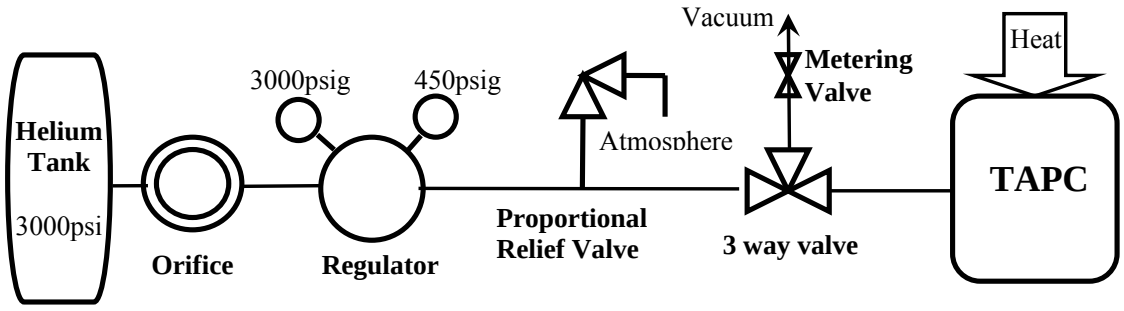

Figure B.3: TAPC fill system schematic

Table B.4: Fill system components

Helium Tank	Grade 5.0 Helium [83]
Orifice	O'Keefe - 0.010 inch diameter [84]
Regulator	Harris Model #25-500C-580 [54]
Proportional Relief Valve	Swagelok R4 Series [31]
3-way Switching Valve	Swagelok Model #SS-41XS1 [31]
Metering Valve	Swagelok SS-4MG-MH [31]

B.3.2 TAPC System

Under normal operating conditions the addition of heat causes acoustic pressure waves at ±45 psig on top of the 450 psig mean pressure. Controlling the heat into the TAPC is of the utmost importance for the following two reasons, in order of significance:

1. The increased temperature of the hot component (Inconel 625 Hot Heat Exchanger) reduces its ability to withstand the internal pressure. This is apparent when looking at the Allowable Stresses of Inconel 625 at Increased Temperatures (Table B.5).
2. Increased heat input will cause the internal pressure to increase.

Table B.5: Allowable Stress in Inconel 625 Grade 2 [4]

Temperature (°F)	1050	1100	1150	1200	1250	1300	1350	1400	1450	1500	1550	1600
Allowable Stress (ksi)	19.4	19.4	19.3	19.3	15.0	11.6	8.5	6.7	4.9	3.8	2.6	1.9

Figure B.4 shows schematically how heat enters the TAPC system. The temperature controller [85] is convenient for general testing because it automatically keeps the hot end at any desired temperature based on the feedback of a reference thermocouple. However it works by employing a duty cycle (on and off periods) to an AC power input, which is real inconvenient when performing efficiency tests. Hence for this purpose a dc power supply [69,70] was employed in order to easily determine the heat input to the cartridge heaters and into the TAPC.

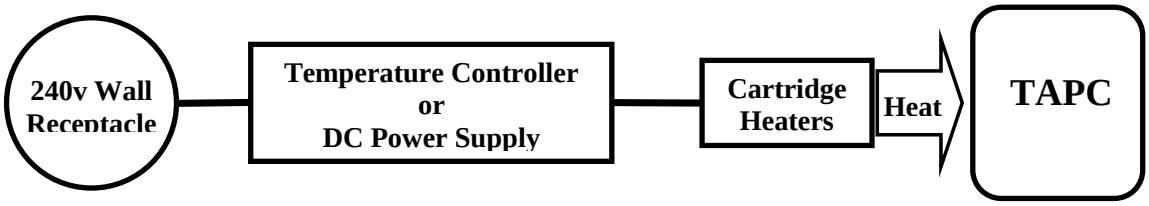

Figure B.4: TAPC heat input control system

B.4 Pressure Vessel Analysis

The following analysis is formatted with the modular design scheme in mind, where each component is analyzed for qualification during the operational design

conditions and the hydrostatic test pressure (Section B.2). Components are labeled in Figure 3.3.

B.4.1 Hot Heat Exchanger stay cross-sectional area

Square stays with 0.090 inch sides were machined into a block of inconel to prevent the thin bottom HHX plates (see the cross-sectional views of the HHX shown in Figure B.5) from bowing outward during internal pressurization, as described in Section 3.3.3.1.1. The minimum cross-sectional area of these integral stays and the load that they can support is based on UG-50 (Dimensions of Staybolts) in Reference [4]. The load supported by the stays is the product of the area that they support (flow volume between plates minus the total footprint of the stays, i.e. the "open area") and the maximum allowable working pressure. This load divided by the total stay area and then multiplied by a safety factor of 1.1 (UG-50(a) [4]) can then be compared to the allowable stress value of the material at temperature. Note that the following analysis is conservative because the "plugs" that are welded in the slots of the HHX (Calculation 3) will further prevent outward bowing, yet this fact is ignored.

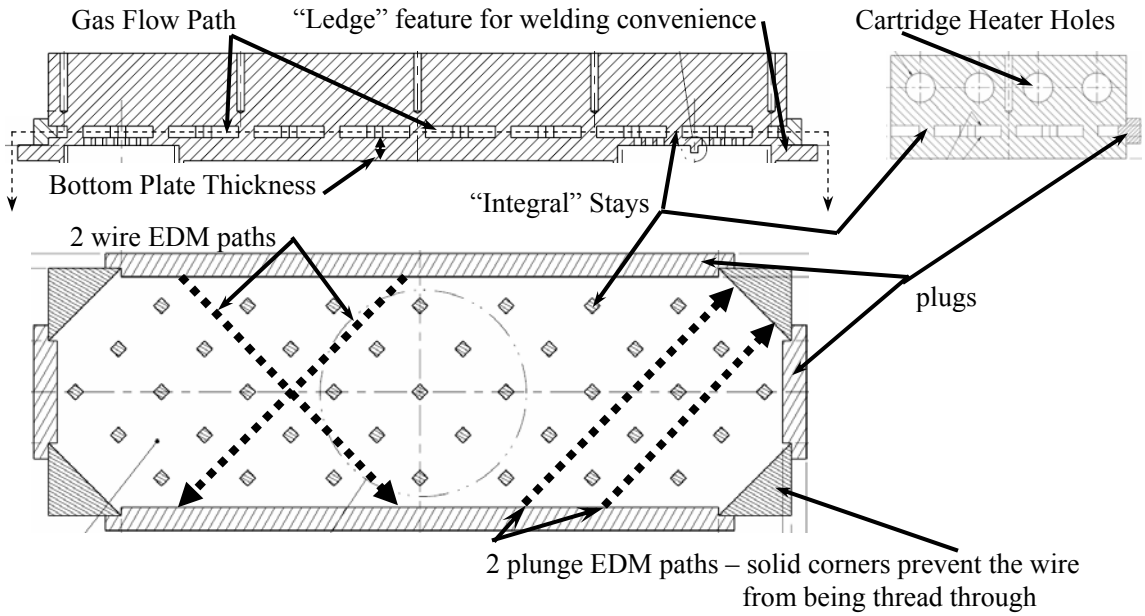

Figure B.5: Hot Heat Exchanger cross-sectional views

n = number of stays
A_{stay} = cross-sectional area of one stay
A_{open} = total open area (not occupied by a stay)
A = total area between plates
s = required allowable stress value based on calculation
Load = open area multiplied by internal pressure
P = internal design pressure
$_{hdyro}$ = conditions during hydrostatic pressure qualification testing

$$n := 39 \quad A_{stay} := (0.090in)^2 \quad A := (4.826 \cdot in \cdot 2 \cdot in) + 2 \cdot \left[1.08 \cdot in \cdot .587 \cdot in + 2 \cdot \left(\frac{1}{2} \cdot .587 \cdot in \cdot 0.46 \cdot in \right) \right]$$

$$A_{open} := A - n \cdot A_{stay}$$

Design Condition Stress

$$P := 500 \cdot \frac{lb}{in^2} \quad Load := A_{open} \cdot P$$

$$s := \frac{Load}{n \cdot A_{stay}} \cdot 1.1$$

$$s = 1.94 \times 10^4 \frac{lb}{in^2} \sim S_{500F} := 19.3 \cdot 10^3 \frac{lb}{in^2}$$

Hydrostatic Test Condition Stress

$$P_{hydro} := 750 \cdot \frac{lb}{in^2} \quad Load_{hydro} := A_{open} \cdot P_{hydro}$$

$$s_{hydro} := \frac{Load_{hydro}}{n \cdot A_{stay}} \cdot 1.1$$

$$s_{hydro} = 2.91 \times 10^4 \frac{lb}{in^2} \sim S_{80F} := 26.7 \cdot 10^3 \frac{lb}{in^2}$$

The stress values of the stay material during hot operation and pressure qualification testing are approximately equal to their respective temperature dependent Reference [4] allowable stresses and summarized in Table B.5. Therefore the stay geometry can sufficiently handle the applied pressures.

B.4.2 Stayed plate thickness

t = thickness of bottom plate (thinner and more limiting than top plate)
P = internal design pressure
S = maximum allowable stress value in tension at temperature (1200°F)
p = maximum pitch, the greatest distance between any set of parallel straight lines (either horizontal, vertical or inclined) passing through the centers of staybolts in adjacent rows
C = 2.1 for stays screwed through plates not over 7/16 inches thick. This is the most conservative value in the reference; however these "integral" stays will perform much better than the staybolt that this value is based upon.

$$P := 500psi \quad S := 19.3\,10^3 psi \quad p := 0.6958in \quad C := 2.1$$

$$t := p \cdot \sqrt{\frac{P}{S \cdot C}} \quad t = 0.077\,in \quad t_{actual} := 0.188in \quad P_{max} := \frac{t_{actual}^2 \cdot S \cdot C}{p^2} \quad \boxed{P_{max} = 2.959 \times 10^3 psi}$$

The actual thickness is greater than the required minimum thickness, allowing an internal design pressure up to the calculated maximum pressure of 2959 psig.

B.4.3 Hot Heat Exchanger plug fillet welds

The machining process that resulted in the integral stays leaves a slot on all four sides of the HHX. Plates of the same material will be fillet welded to the HHX in order to cover these slots (Figure B.5). The welds that join the "long" and "short" plates with their respective slots are analyzed per Reference [4] UW-18 (Fillet Welds) and are analyzed below.

t = nominal thickness of plate covering slot (UW-13)
p = perimeter
a = area
l = weld leg = t (Figure UW-13.1.b)
r = weld root = L*√2
w = weld area = p*r
E= joint efficiency = 55% (conservative)
A = allowable load on fillet
P = internal pressure
S = allowable stress on material at temperature
F = force applied on plate from internal pressure
$_l$ = long
$_s$ = short

$t := 0.12\,in \qquad l := t \qquad S := 19.3 \cdot 10^3 \frac{lb}{in^2} \qquad r := \sqrt{2} \cdot l \qquad E := 0.55 \qquad P := 500 \frac{lb}{in^2}$

Long Plate Case:

$p_l := 2 \cdot (5.080 \cdot in + 0.214 \cdot in)$

$w_l := p_l \cdot r \qquad w_l = 1.797\,in^2$

$A_l := w_l \cdot S \cdot E \qquad A_l = 1.907 \times 10^4\,lb$

$a_l := (5.080 \cdot in) \cdot (0.214 \cdot in)$

$F_l := P \cdot a_l \qquad F_l = 543.56\,lb \quad < A_l$

$P_{l\_max} := \frac{A_l}{a_l} \qquad P_{l\_max} = 1.754 \times 10^4 \frac{lb}{in^2}$

Short Plate Case:

$p_s := 2 \cdot (1.080\,in + 0.214\,in)$

$w_s := p_s \cdot r \qquad w_s = 0.439\,in^2$

$A_s := w_s \cdot S \cdot E \qquad A_s = 4.662 \times 10^3\,lb$

$a_s := (1.080\,in) \cdot (0.214 \cdot in)$

$F_s := P \cdot a_s \qquad F_s = 115.56\,lb \quad < A_s$

$P_{s\_max} := \frac{A_s}{a_s} \qquad P_{s\_max} = 2.017 \times 10^4 \frac{lb}{in^2}$

In both the long and short plate cases, the force applied to the plate (F) is less than the respective allowable loads on the fillet (A). Therefore the fillet welds sufficiently handle the internal design and hydrostatic test pressures.

B.4.4 Regenerator and Thermal Buffer Tube wall

The HHX has two tube-like features that will be circumferentially welded to a pair of lap joint stub ends (machined out of the same Inconel 625 material), shown in Figure B.6. Once welded, these portions make up the Thermal Buffer Tube and Regenerator. It is noted that after the following analysis and prior to the hydrostatic pressure test these circumferential welds, and the fillet welds from Section B.4.3, were examined with a "dye penetrate." This substance is rubbed on the welds and will change color at the spots where it can seep into a pore, i.e. a weld inconsistency.

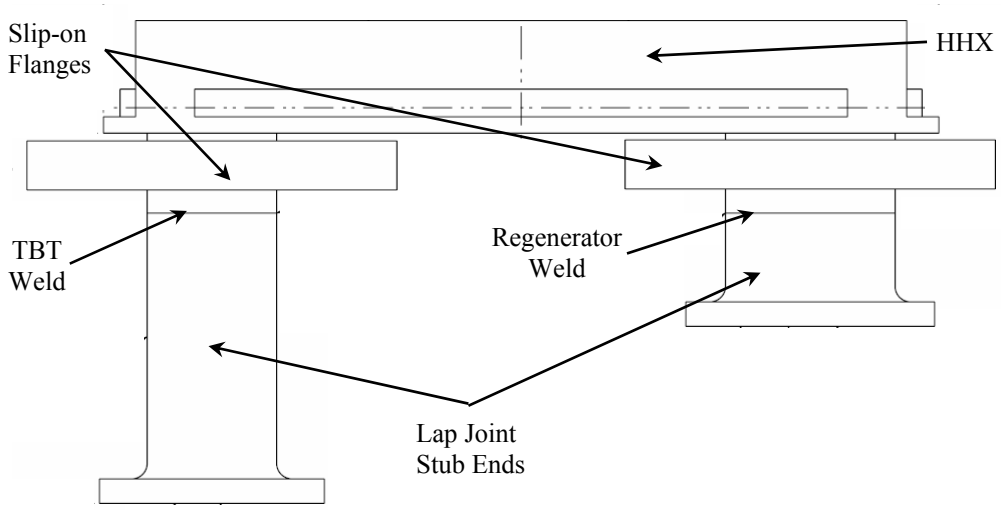

Figure B.6: Thermal Buffer Tube and Regenerator

Based on UG-27(d) (Thickness of Shells under Internal Pressure – Longitudinal Stress) in Reference [4]:

t = minimum thickness of shell
P = internal design pressure
r = inside radius of shell

S = maximum allowable stress value at 1200°F in the HHX
E = joint efficiency for weld (Table UW-12 [4])

$P := 500psi \quad S := 19.3\,10^{3}psi \quad E := 0.70$ (No Radiographic Examination)

$r_{tbt} := \frac{\frac{15}{16}in}{2} \quad t_{tbt} := \frac{P \cdot r_{tbt}}{2S \cdot E + 0.4P}$

$r_{reg} := \frac{1.25in}{2} \quad t_{reg} := \frac{P \cdot r_{reg}}{2S \cdot E + 0.4P}$

$t_{tbt} = 8.61 \times 10^{-3}\,in \quad < \quad t_{tbt\_actual} := 0.035in$

$t_{reg} = 0.011\,in \quad < \quad t_{reg\_actual} := 0.035in$

$P_{tbt\_max} := \frac{2 \cdot S \cdot E \cdot t_{tbt\_actual}}{r_{tbt} - 0.4t_{tbt\_actual}}$

$P_{reg\_max} := \frac{2 \cdot S \cdot E \cdot t_{reg\_actual}}{r_{reg} - 0.4t_{reg\_actual}}$

$P_{tbt\_max} = 2.08 \times 10^{3}\,psi$

$P_{reg\_max} = 1.548 \times 10^{3}\,psi$

This calculation confirms the integrity of the tube wall for both the thermal buffer tube and regenerator and calculates the maximum possible pressure. Note that the allowable stress value used is for Grade 2 Inconel 625 at 1200°F; this is conservative because the temperature at the welded joints will be substantially less than this value. However, the amount by which is not exactly known, so the conservative value is used.

B.4.5 Thermal Buffer Tube and Regenerator lap joint loose type flanges

Both the TBT and Regenerator are connected to the rest of the TAPC with a lap joint slip-on flange (Figure B.6). The analysis of this type of flange is found in Appendix 2 (Rules for Bolted Flange Connections) of Reference [4]. The first calculation in this section is for the TBT flange and the second is for the Regenerator flange.

A = outside diameter of flange
A_b = cross-sectional area of bolts using root diameter
A_m = total required cross-sectional area of bolts at thread root under operating stress
B = inside flange diameter
b = effective joint-contact-surface seating
C = bolt-circle diameter
d = root diameter of ¼-20 bolt
G = diameter at location of gasket load reaction
H = total hydrostatic end force
H_D = hydrostatic end force on area inside flange
H_p = total joint – contact surface compression load (= 0lb for o-rings)
H_T = difference between H and H_D
h_D, h_G, h_T = moment arms to respective loads

ID_o = inside diameter of O-ring
K_f = ratio of outside flange diameter to inside diameter = A/B
M_o = total moment acting on the flange under operating conditions
M_G = moment based on gasket seating
M_0 = the greater moment between M_o and M_G
m = gasket factor = 0 for O-rings (self energizing per Appendix 2 - Table 2-5.1)
N = number of bolt holes in the flange
P = internal design pressure of hydrostatic proof test (per UG-100)
S_b = allowable bolt stress (Type 304 Stainless Steel – 18CR-8Ni) at 200°F
S_f = allowable design stress for the material of the flange at design temperature
S_H = calculated longitudinal stress in hub
S_R = calculated radial stress in flange
S_T = calculated tangential stress in flange
t = flange thickness
W = flange design bolt load under operation
w = width of O-ring
Y = factor involving K

Internal Pressure:

$$P := 500 \frac{lb}{in^2}$$

Material Constants:

$$S_b := 25 \cdot 10^3 \frac{lb}{in^2} \qquad S_f := 26.7 \cdot 10^3 \frac{lb}{in^2}$$

Geometry and Calculation Constants:

$A := 2.73in$ $B := 1.047in$ $C := 2.312in$ $N := 6$ $d := 0.1905in$ $w := 0.070in$ $ID_o := 1.176in$

$$K_f := \frac{A}{B} \quad t := \frac{3}{8}in \quad A_b := N \cdot \left[\pi \cdot \left(\frac{d}{2}\right)^2\right] \quad G := ID_o + 2\left(\frac{w}{2}\right) \quad H := 0.785 \cdot G^2 \cdot P \quad m := 0$$

$$H_p := 0lb \text{ for o-rings} \quad W := H + H_p \quad A_m := \frac{W}{S_b} \quad Y := \frac{1}{K_f - 1} \cdot \left(0.66845 + 5.71690 \cdot \frac{K_f^2}{K_f^2 - 1} \log(K_f)\right)$$

For Lap Type Flanges (Table 2-6):

$$h_D := \frac{C - B}{2} \quad h_T := \frac{C - G}{2} \quad h_G := h_T \quad H_D := 0.785 \cdot B^2 \cdot P \quad H_T := H - H_D \quad H_G := W - H$$

$$M_o := H_D \cdot h_D + H_T \cdot h_T + H_G \cdot h_G \qquad M_G := W \cdot \frac{C - G}{2}$$

Per Appendix 2-5 (a) (1):

$M_o = 30.633\,lb\,ft$ > $M_G = 27.066\,lb\,ft$ --> $M_0 := M_o$

Per Appendix 2-7 (b):

$$S_T := \frac{Y \cdot M_0}{t^2 \cdot B} \qquad S_R := 0 \frac{lb}{in^2} \qquad S_H := 0 \frac{lb}{in^2}$$

Per Appendix 2-8 (a) (1):

$$S_H = 0 \frac{lb}{in^2} < 1.5 \cdot S_f = 4.005 \times 10^4 \frac{lb}{in^2}$$

Per Appendix 2-8 (a) (2):

$$S_R = 0 \frac{lb}{in^2} < S_f = 2.67 \times 10^4 \frac{lb}{in^2}$$

Per Apperndix 2-8 (a) (3):

$$S_T = 5.371 \times 10^3 \frac{lb}{in^2} < S_f = 2.67 \times 10^4 \frac{lb}{in^2}$$

$$P_{max} := 2485 \frac{lb}{in^2}$$

Per Appendix 2-8 (a) (4):

$$\frac{S_H + S_R}{2} = 0 \frac{lb}{in^2} \qquad \frac{S_H + S_T}{2} = 2.686 \times 10^3 \frac{lb}{in^2} < S_f = 2.67 \times 10^4 \frac{lb}{in^2}$$

Per Appendix 2-5 (c) (3) - Required Bolt Loads

$$A_m = 0.024\,in^2 < A_b = 0.171\,in^2$$

Thus the bolts can sufficiently maintain the internal pressure.

Appendix 2-8 (c) provides a qualification for when the lap is subjected to shear as the result of gasket location, however in this assembly, the usage of an o-ring prevents any lap shear (same holds in the Regenerator Flange calculation below). Every condition in this calculation is met and the corresponding maximum pressure is determined by iterating until the tangential stress is equal to the allow stress in condition (a)(3); a value of 2,485 psig is found for the TBT flange.

Internal Pressure:

$$P := 500 \frac{lb}{in^2}$$

Material Constants:

$$S_b := 25 \cdot 10^3 \frac{lb}{in^2} \qquad S_f := 26.7 \cdot 10^3 \frac{lb}{in^2}$$

Geometry and Calculation Constants:

$A := 2.73in$ $B := 1.360in$ $C := 2.312in$ $N := 6$ $d := 0.1905in$ $w := 0.070in$ $ID_o := 1.489in$

$$K_f := \frac{A}{B} \quad t := \frac{3}{8}in \quad A_b := N \cdot \left[\pi \cdot \left(\frac{d}{2}\right)^2\right] \quad G := ID_o + 2\left(\frac{w}{2}\right) \quad H := 0.785 \cdot G^2 \cdot P \quad m := 0$$

$$H_p := 0lb \text{ for o-rings} \quad W := H + H_p \quad A_m := \frac{W}{S_b} \quad Y := \frac{1}{K_f - 1} \cdot \left(0.66845 + 5.71690 \cdot \frac{K_f^2}{K_f^2 - 1} \log(K_f)\right)$$

For Lap Type Flanges (Table 2-6):

$$h_D := \frac{C - B}{2} \quad h_T := \frac{C - G}{2} \quad h_G := h_T \quad H_D := 0.785 \cdot B^2 \cdot P \quad H_T := H - H_D \quad H_G := W - H$$

$$M_o := H_D \cdot h_D + H_T \cdot h_T + H_G \cdot h_G \qquad M_G := W \cdot \frac{C - G}{2}$$

Per Appendix 2-5 (a) (1):

$M_o = 35.95\,lb\,ft$ > $M_G = 29.931\,lb\,ft$ --> $M_0 := M_o$ $\quad S_T := \frac{Y \cdot M_0}{t^2 \cdot B}$ $\quad S_R := 0\frac{lb}{in^2}$ $\quad S_H := 0\frac{lb}{in^2}$

Per Appendix 2-7 (b):

Per Appendix 2-8 (a) (1):

$$S_H = 0\frac{lb}{in^2} < 1.5 \cdot S_f = 4.005 \times 10^4 \frac{lb}{in^2}$$

Per Appendix 2-8 (a) (2):

$$S_R = 0\frac{lb}{in^2} < S_f = 2.67 \times 10^4 \frac{lb}{in^2}$$

Per Apperndix 2-8 (a) (3):

$$S_T = 6.65 \times 10^3 \frac{lb}{in^2} < S_f = 2.67 \times 10^4 \frac{lb}{in^2}$$

$$P_{max} := 2000 \frac{lb}{in^2}$$

Per Appendix 2-8 (a) (4):

$$\frac{S_H + S_R}{2} = 0\frac{lb}{in^2} \qquad \frac{S_H + S_T}{2} = 3.325 \times 10^3 \frac{lb}{in^2} < S_f = 2.67 \times 10^4 \frac{lb}{in^2}$$

Per Appendix 2-5 (c) (3) - Required Bolt Loads

$A_m = 0.038\,in^2$ < $A_b = 0.171\,in^2$ Thus the bolts can sufficiently maintain the internal pressure.

The calculated tangential stress is less than the allowable design stress for a flange made out of Grade 2 Inconel 625 and this Regenerator lap joint flange can correspondingly maintain a maximum pressure of 2,000 psig.

B.4.6 Ambient Heat Exchanger wall thickness

The ambient heat exchanger (AHX) is a copper rod with holes bored through it for the pressurized helium gas to oscillate. The following calculation verifies the wall thickness shown in Figure B.7, which serves as the mean pressure boundary and is based

on Part UG-27 of Reference [4]. The wall thicknesses (ligaments) between all internal tube features are the same 0.030 inch value; however the critical dimension is the outside wall thickness because this is the separation between the high pressure gas and the low pressure water, i.e. the mean pressure boundary.

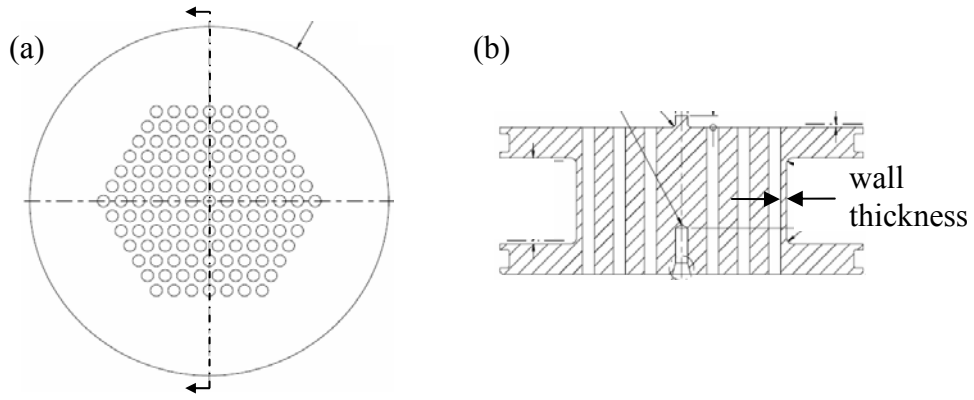

Figure B.7: Ambient Heat Exchanger drawing. (a) top view and (b) cross-section.

P = design pressure
t = wall thickness
r = internal radius of a single tube
S = allowable stress value of copper

$$P := 500 \frac{lb}{in^2} \qquad r := \frac{0.062}{2} in \qquad S := 5.0 \cdot 10^3 \frac{lb}{in^2}$$

$$t := \frac{P \cdot r}{S - 0.6 \cdot P} \qquad t = 3.298 \times 10^{-3} \, in$$

$$t_{actual} := 0.030 in \qquad P_{max} := \frac{S \cdot t_{actual}}{r + 0.6 \cdot t_{actual}} \qquad \boxed{P_{max} = 3.061 \times 10^3 \frac{lb}{in^2}}$$

This calculation proves that the outside wall thickness of the AHX can withstand a maximum pressure of 3061 psig.

Surrounding the AHX is a “jacket” of water at approximately 20psig; the following calculation confirms that the stainless steel shell that the AHX and water jacket reside within can maintain the water pressure. However it is noted that the following

radius ignores the fact that the water jacket volume is mostly filled with the copper component analyzed in the previous calculation. Thus the following calculation, based on UG-27 (c) (1), is conservative.

P = water pressure ≈ 20 psig
t = wall thickness
r = internal radius of water region
S = allowable stress of stainless steel at the water's operating temperature

$$P := 20\,\frac{lb}{in^2} \qquad r := 0.800\,in \qquad S := 20 \cdot 10^3\,\frac{lb}{in^2}$$

$$t := \frac{P \cdot r}{S - 0.6 \cdot P} \qquad t = 8.005 \times 10^{-4}\,in$$

$$t_{actual} := 0.580\,in \qquad P_{max\_H2O} := \frac{S \cdot t_{actual}}{r + 0.6 \cdot t_{actual}} \qquad \boxed{P_{max\_H2O} = 1.01 \times 10^4\,\frac{lb}{in^2}}$$

This calculation proves that the shell thickness can maintain a water pressure up to 10,100 psig.

B.4.7 Compliance volume

Shown in Figure B.8, the following calculation confirms that the shell thickness of the compliance volume is capable of maintaining the internal pressure; it is based on the Circumferential Stress analysis of UG-27 (c) (1) in Reference [4].

P = design pressure
t = required wall thickness based on P
r = internal radius of compliance volume
S = allowable stress value of the Type 304 stainless steel

$$P := 500\,\frac{lb}{in^2} \qquad r := 0.800\,in \qquad S := 16.7 \cdot 10^3\,\frac{lb}{in^2}$$

$$t := \frac{P \cdot r}{S - 0.6 \cdot P} \qquad t = 0.024\ in$$

$$t_{actual} := 0.575\,in \qquad P_{max} := \frac{S \cdot t_{actual}}{r + 0.6 \cdot t_{actual}} \qquad \boxed{P_{max} = 8.386 \times 10^3\,\frac{lb}{in^2}}$$

The compliance volume's shell can maintain a maximum internal pressure of 8,386 psig.

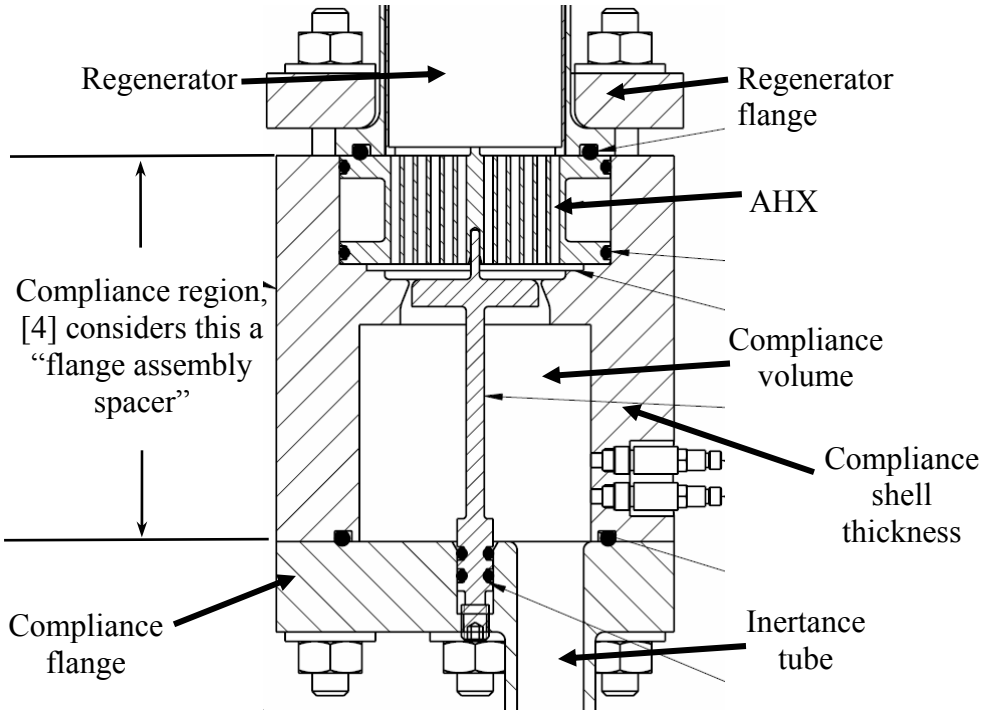

Figure B.8: Compliance

The bottom of the compliance volume is capped with a flange that is used to transition to the inertance tube. In order to analyze this flange, the Regenerator Flange (2nd calculation of Section B.4.5), Compliance region (which is considered a spacer here) and this Compliance flange are looked at as one assembly. Appendix Y [4] classifies this flange pair as a "Class 3 Assembly with a spacer" (Fig.Y-5.1.1.b [4]) because the opening in the reducing Compliance flange is less than one-half of the bolt circle diameter. This assembly is further characterized as "Category 1" because the flange in question (Compliance) is integral to the nozzle neck (Inertance Tube). Throughout the following calculation the subscripts "I" and "II" denote the "non-reducing" Regenerator flange and "reducing" Compliance flange, respectively.

A = outside diameter of flange
A_b = cross-sectional area of bolts at root diameter
A_m = total required cross-sectional area of bolts at thread root under operating stress=W_{m1}/S_b
a = shape factor
B = inside diameter of reducing flange = ID of inertance tube

B_1 = inside diameter of flange + g_1
b = effective joint-contact-surface seating width
C = bolt-circle diameter
C_1, C_2, C_2, C_4 = factors
D = bolt hole diameter
d = root diameter of fastener (¼-20 bolt)
E = modulus of elasticity of flange material (I - Inconel 625, II - 304 Stainless)
E_1 = factor = $E*t^3$
F_I = factor dependent on category and class of flange assembly
G = diameter at location of gasket load reaction = mean o-ring diameter
g_0 = thickness of hub at small end
g_1 = thickness of hub at back of flange
H_D = hydrostatic end force on area inside flange
H_G = gasket load due to seating pressure, plus axial force generated by self-sealing gasket
H_T = difference between total hydrostatic end force and end force on area inside of flange
h = hub length
h_D = radial distance from the bolt circle to the circle on which H_D acts
h_G = radial distance from the gasket load reaction to the bolt circle
h_0 = factor = $[B*g_0]^{½}$
h_c = radial distance from bolt circle to flange-flange tangential contact
h_T = radial distance from the bolt circle to the circle on which H_T acts
ID_o = o-ring inside diameter
J_S = factor
K_f = ratio of outside flange diameter to inside diameter = A/B
l = calculated strain length of bolt
M_p = moment due to H_D, H_T, and H_G
m = gasket factor = 0 for O-rings (self energizing per Appendix 2 - Table 2-5.1)
n = number of bolt holes in the flange
P = internal design pressure
r = radial distance form bolt circle to hub intersection
r_B = factor
r_{EI} = elasticity factor = flange elasticity modulus divided by bolt elasticity modulus.
S_a = allowable stress in threaded rod at atmospheric temperature
S_b = allowable stress in threaded rod at design temperature
S_f = allowable design stress for flange (II) material at design temperature
S_T = calculated tangential stress in flange
t = "reducing" (Compliance) flange thickness
t_s = thickness of spacer in between compliance and regenerator flanges
W = flange design bolt load under operation
w = width of O-ring = b
X = factor
Y = factor involving K
β = shape factor for full face metal-to-metal contact

Internal Pressure

$$P := 500\frac{lb}{in^2}$$

Flange and Bolt Geometry

$A := 2.730in \quad C := 2.312in \quad g_0 := 0.083in \quad n := 6 \quad h_C := 0.219in \quad d := 0.1905in \quad m := 0 \quad d_B := 0.25in \quad B := 0.459in$

$D := 0.290in \quad g_1 := g_0 \quad G := 1.85in \quad t_I := 0.38in \quad t_{II} := 0.625in \quad t_s := 2.668in \quad l := t_I + t_{II} + t_s + \frac{1}{2}\cdot d_B \cdot 2$

for Flange II:

$$B_1 := B + g_0 \quad R_0 := \frac{C - B}{2} - g_1 \quad h_D := R_0 + 0.5g_1 \quad h_G := \frac{C - G}{2} \quad h_T := \frac{R_0 + g_1 + h_G}{2} \quad A_b := n\cdot\left[\pi\cdot\left(\frac{d}{2}\right)^2\right]$$

Material Values

$$E_I := 27.1\cdot 10^6\frac{lb}{in^2} \qquad E_{II} := 27.5\cdot 10^6\frac{lb}{in^2} \qquad S_{f\_I} := 26.7\cdot 10^3\frac{lb}{in^2} \qquad S_{f\_II} := 20.0\cdot 10^3\frac{lb}{in^2}$$

$$E_{bolt} := 28.5\cdot 10^6\frac{lb}{in^2} \qquad S_b := 25\cdot 10^4\frac{lb}{in^2} \qquad r_{E\_I} := \frac{E_I}{E_{bolt}} \qquad r_{E\_II} := \frac{E_{II}}{E_{bolt}}$$

Forces and Factors

$$\beta := \frac{C + B_1}{2B_1} \quad a := \frac{A + C}{2B_1} \quad AR := \frac{n\cdot D}{\pi C} \quad f := 1 \quad H := 0.785\cdot G^2\cdot P \quad H_p := 0lb \quad H_D := 0.785\cdot B^2\cdot P$$

$$H_T := H - H_D \quad W := H + H_p \quad H_G := W - H \quad M_P := H_D\cdot h_D + H_T\cdot h_T + H_G\cdot h_G \quad M_s := 0$$

$$r_B := \frac{1}{n}\left(\frac{4}{\sqrt{1 - AR^2}}\operatorname{atan}\left(\sqrt{\frac{1 + AR}{1 - AR}}\right) - \pi - 2AR\right) \quad J_S := \frac{1}{B_1}\left(\frac{2h_D}{\beta} + \frac{h_C}{a}\right) + \pi\cdot r_B \quad X := \frac{E_{II}\cdot(t_{II})^3}{E_{II}\cdot t_{II}^3 + E_{II}\cdot t_{II}^3}$$

(Fig. 2-7.2) (Fig. 2-7.3)

$F := 0.908920 \quad V := 0.550103 \qquad F_I := g_0^2\cdot\frac{\left(\sqrt{B\cdot g_0} + F\cdot t_{II}\right)}{V} \quad J_P := \frac{1}{B_1}\left(\frac{h_D}{\beta} + \frac{h_C}{a}\right) + \pi\cdot r_B$

$$C_1 := \frac{-\left(0.748 - 1.567J_S\cdot\log\left(\frac{A}{B_1}\right)\right)}{\left(1 + 1.3J_S\right)} \qquad C_2 := \frac{\left[\frac{\pi}{32}\left(P\cdot B_1^3\right) - 1.3J_P\cdot M_P\right]}{1 + 1.3J_S}$$

$$C_3 := \frac{-\left(0.575 - 1.206J_S\cdot\log\left(\frac{A}{B_1}\right)\right)}{J_S + \frac{t_{II}^3}{F_I}} \qquad C_4 := \frac{-J_P\cdot M_P}{J_S + \frac{t_{II}^3}{F_I}} \qquad Z := \frac{\left(\frac{A}{B}\right)^2 + 1}{\left(\frac{A}{B}\right)^2 - 1}$$

Rigid Body Rotation of Flanges

$$\theta_I := \frac{X\cdot(C_4 - C_2)}{1.206\cdot\log\left(\frac{A}{B}\right) - X\cdot C_3 - (1 - X)\cdot C_1}\cdot\frac{1}{E_I\cdot(t_I)^3} \qquad \theta_{II} := -E_{II}\cdot t_{II}^3\cdot\theta_I\cdot\left(\frac{E_{II}\cdot t_{II}^3}{E_{II}\cdot t_{II}^3}\right)\cdot\frac{1}{E_{II}\cdot t_{II}^3}$$

Total Flange Moment at Diameter B $_1$

$$M_{SI} := C_3\cdot\left(E_I\cdot t_I^3\cdot\theta_I\right) + C_4$$

$$M_{SII} := C_1\cdot\left(E_{II}\cdot t_I^3\cdot\theta_{II}\right) + C_2$$

Unbalanced Flange Moment at Diameter B $_1$

$$M_{uI} := 1.2068\left(E_I\cdot t_I^3\cdot\theta_I\right)\cdot\log\left(\frac{A}{B_1}\right)$$

$$M_{uII} := 1.2068\left(E_{II}\cdot t_{II}^3\cdot\theta_{II}\right)\cdot\log\left(\frac{A}{B_1}\right)$$

Balanced Flange Moment at Diameter B $_1$

$M_{bI} := M_{SI} - M_{uI}$

$M_{bII} := M_{SII} - M_{uII}$

$H_C := \frac{M_P + M_{bI}}{h_C}$ $\quad W_{m1} := H + H_G + H_C$

Slope of Flange at Diameter B $_1$

$$\theta_{BI} := \left[\frac{5.46}{\pi \cdot t_I^{\,3}} \cdot \left(J_S \cdot M_{bI} + J_P \cdot M_P\right) + E_{II} \cdot t_I^{\,3} \cdot \frac{\theta_I}{t_I^{\,3}}\right] \cdot \left(\frac{1}{E_I}\right)$$

$$\theta_{BII} := \left[-1.337 \cdot \left(M_{SII} - \pi \cdot P \cdot \frac{B_1^{\,3}}{32}\right) \cdot \frac{1}{t_{II}^{\,3}}\right] \cdot \left(\frac{1}{E_{II}}\right)$$

Operating Bolt Stress:

Per Y-7 (a): $\sigma_b <$ S_b

$\sigma_b := \frac{W_{m1}}{A_b}$ $\quad \sigma_b = 2.503 \times 10^4 \frac{lb}{in^2} < S_b = 2.5 \times 10^5 \frac{lb}{in^2}$

Design Prestress in Bolts:

$$S_i := \sigma_b - \frac{1.159 \cdot h_C^{\,2} \cdot \left(M_P + M_{bI}\right)}{2(1 - X)\, a \cdot t_I^{\,3} \cdot l \cdot r_{E\_II} \cdot B_1} \qquad S_i = 2.496 \times 10^4 \frac{lb}{in^2}$$

Flange II (reducing flange) Stresses:

Longitudinal Hub Stress

$$S_{HII} := \frac{\sqrt{B_1 \cdot g_0} \cdot E_{II} \cdot \theta_{BII} \cdot f}{0.91 \cdot \left(\frac{g_1}{g_0}\right)^2 \cdot B_1 \cdot V}$$

Per Y-7 (c): S $_H$ < 1.5*S $_f$

$S_{HII} = 1.443 \times 10^3 \frac{lb}{in^2} < 1.5S_{f\_II} = 3 \times 10^4 \frac{lb}{in^2}$

Radial Stresses

@ Bolt Circle:

$$S_{RBCII} := \frac{6 \cdot \left(M_P + M_{SII}\right)}{t_{II}^{\,2}\left(\pi \cdot C - n \cdot D\right)}$$

@ B $_1$:

$$S_{RBII} := \frac{6 \cdot M_{SII}}{\pi B_1 \cdot t_{II}^{\,2}}$$

Per Y-7 (c): S $_R$ < S $_f$

$S_{RBCII} = 1.317 \times 10^3 \frac{lb}{in^2}$

$S_{RBII} = -2.97 \times 10^3 \frac{lb}{in^2} < S_{f\_II} = 2 \times 10^4 \frac{lb}{in^2}$

$S_{RCII} = 3.087 \times 10^3 \frac{lb}{in^2}$

@ center of Flange II :

$$S_{RCII} := \frac{0.3094 \cdot P \cdot B_1^{\,2}}{t_{II}^{\,2}} - 6 \cdot \frac{M_{SII}}{\pi \cdot B_1 \cdot t_{II}^{\,2}}$$

Tangential Stresses

@ B $_1$:

$$S_{TBII} := \frac{t_{II} \cdot E_{II} \cdot \theta_{BII}}{B_1} - \frac{1.8 \cdot M_{SII}}{\pi \cdot B_1 \cdot t_{II}^{\,2}}$$

@ center of Flange II :

$S_{TCII} := S_{RCII}$

Per Y-7 (d): S $_T$ < S $_f$

$S_{TBII} = 3.02 \times 10^3 \frac{lb}{in^2}$

$S_{TCII} = 3.087 \times 10^3 \frac{lb}{in^2} < S_{f\_II} = 2 \times 10^4 \frac{lb}{in^2}$

Per Y-7 (e): (S $_H$+S$_R$)/2 and (S $_H$+S$_T$)/2 < S $_f$

$\frac{S_{HII} + S_{RBCII}}{2} = 1.38 \times 10^3 \frac{lb}{in^2}$

$\frac{S_{HII} + S_{RBII}}{2} = -763.579 \frac{lb}{in^2}$

$\frac{S_{HII} + S_{RCII}}{2} = 2.265 \times 10^3 \frac{lb}{in^2} < S_{f\_II} = 2 \times 10^4 \frac{lb}{in^2}$

$\frac{S_{HII} + S_{TBII}}{2} = 2.231 \times 10^3 \frac{lb}{in^2}$

$\frac{S_{HII} + S_{TCII}}{2} = 2.265 \times 10^3 \frac{lb}{in^2}$

Per Y-7 (f): S $_R$ and S $_T$ < S $_f$:

$S_{RCII} = 3.087 \times 10^3 \frac{lb}{in^2} < S_{f\_II} = 2 \times 10^4 \frac{lb}{in^2}$

$S_{TCII} = 3.087 \times 10^3 \frac{lb}{in^2}$

$P_{max} := 3250psi$

The previous calculation proves that this flange assembly can sufficiently maintain the required design pressure. Furthermore, iterating the pressure determined that the limiting values are the radial and tangential stresses at the center of Flange II. These stresses equal their respective allowable values (S_f), based on material and temperature ([4] Part D – Table 1B), at a pressure of 3250psig, which is therefore the maximum pressure that the Regenerator loose type flange – Compliance region spacer – Compliance flange assembly can withstand.

B.4.8 Inertance tube wall thickness

The seamless stainless steel inertance tube is connected at both ends with stock Swagelok® fittings and its wall thickness is analyzed in the following calculation based on UG-27 (1) of Reference [4].

P = hydrostatic proof test pressure
t = wall thickness
r = internal radius of tube
S = allowable stress value of the Type 304 stainless steel

$$P := 500 \frac{lb}{in^2} \qquad r := 0.2475\,in \qquad S := 16.7 \cdot 10^3 \frac{lb}{in^2}$$

$$t := \frac{P \cdot r}{S - 0.6 \cdot P} \qquad t = 7.546 \times 10^{-3}\,in$$

$$t_{actual} := 0.083\,in \qquad P_{max} := \frac{S \cdot t_{actual}}{r + 0.6 \cdot t_{actual}} \qquad P_{max} = 4.662 \times 10^3 \frac{lb}{in^2}$$

This calculation proves that the inertance tube can maintain internal pressures up to 4,662 psig.

B.4.9 Centerplate

The inertance tube is connected to the Centerplate with a Swagelok fitting screwed into a flange. The pressure rating of the Swagelok connector is shown in Table B.6 while the flange that is bolted to the Centerplate is analyzed in the following calculation.

Dimensionally, the holes through each of the mating components (centerplate and Centerplate flange in Figure B.9) are the same, as are the contact surfaces (ignoring the o-ring groove). Hence this assembly is considered Class 1 (for identical flange pairs) and Category 1 (for integral flanges). The variables for this calculation (Appendix Y [4]) are omitted below because they are the same is in the Compliance flange above (B.4.7).

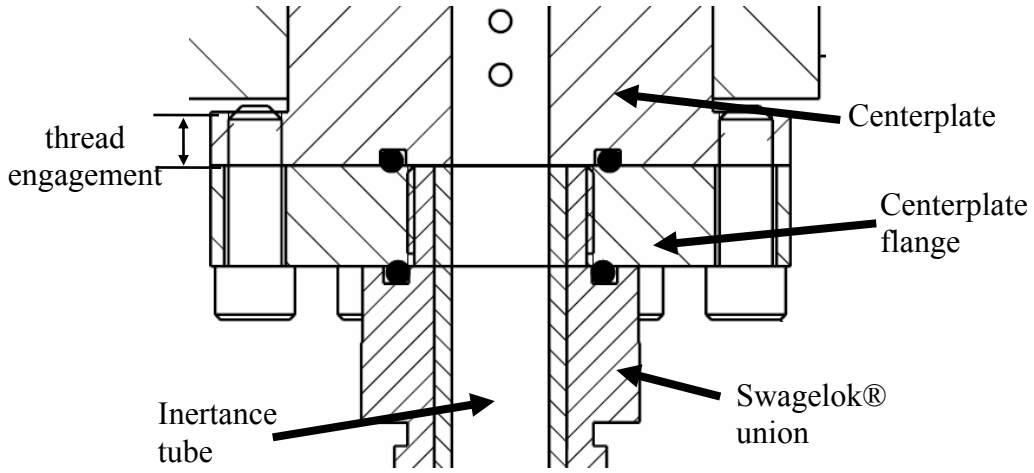

Figure B.9: Centerplate flange assembly cross-section

Internal Design Pressure

$$P := 500\frac{lb}{in^2}$$

Flange and Bolt Geometry

$A := 2.730in \quad C := 2.312in \quad g_0 := 0in \quad n := 6 \quad h_C := 0.200in \quad d := 0.1905in$

$B := 0.495in \quad D := 0.290in \quad g_1 := g_0 \quad G := 1.027in \quad t_I := 0.5in \quad t_{II} := 0.5in \quad A_b := n \cdot \left[\pi \cdot \left(\frac{d}{2}\right)^2\right]$

$d_B := 0.25in \quad m := 0 \quad t := t_I$

$$R_0 := \frac{C - B}{2} - g_1 \quad h_D := R_0 + 0.5g_1 \quad h_G := \frac{C - G}{2} \quad h_T := \frac{R_0 + g_1 + h_G}{2} \quad l := t_I + t_{II} + \frac{1}{2} \cdot d_B \cdot 2$$

Material Values

$$E := 27.5 \cdot 10^6\frac{lb}{in^2} \quad E_{bolt} := 18.5 \cdot 10^6\frac{lb}{in^2} \quad r_E := \frac{E}{E_{bolt}} \quad S_f := 25.0 \cdot 10^3\frac{lb}{in^2} \quad S_b := 35 \cdot 10^3\frac{lb}{in^2}$$

Calculation Forces and Factors

$$\beta := \frac{C + B}{2B} \quad a := \frac{A + C}{2B} \quad AR := \frac{n \cdot D}{\pi C} \quad f := 1 \quad H := 0.785 \cdot G^2 \cdot P \quad H_p := 0lb \quad H_D := 0.785 \cdot B^2 \cdot$$

$$H_T := H - H_D \quad W := H + H_p \quad H_G := W - H \quad M_P := H_D \cdot h_D + H_T \cdot h_T + H_G \cdot h_G \quad M_s := 0$$

$$r_B := \frac{1}{n}\left(\frac{4}{\sqrt{1 - AR^2}}\operatorname{atan}\left(\sqrt{\frac{1 + AR}{1 - AR}}\right) - \pi - 2AR\right) \quad J_S := \frac{1}{B}\left(\frac{2h_D}{\beta} + \frac{h_C}{a}\right) + \pi \cdot r_B \quad J_P := \frac{1}{B}\left(\frac{h_D}{\beta} + \frac{h_C}{a}\right)$$

$$C_1 := \frac{-\left(0.748 - 1.567 J_S \cdot \log\left(\frac{A}{B}\right)\right)}{\left(1 + 1.3 J_S\right)} \qquad C_2 := \frac{\left[\frac{\pi}{32}\left(P \cdot B^3\right) - 1.3 J_P \cdot M_P\right]}{1 + 1.3 J_S} \qquad C_3 := 0 \qquad C_4 := 0\,lb \cdot ft$$

$$Z := \frac{\left(\frac{A}{B}\right)^2 + 1}{\left(\frac{A}{B}\right)^2 - 1}$$ (Fig. 2-7.2) (Fig. 2-7.3)

$F := 0.908920 \quad V := 0.550103 \quad F_I := g_0^{\,2} \cdot \frac{\left(\sqrt{B \cdot g_0} + F \cdot t_I\right)}{V}$

Flange moment due to flange-hub interaction

$$M_S := \frac{-J_P \cdot F_I \cdot M_P}{t^3 + J_S \cdot F_I} \qquad M_S = 0\,ft \cdot lb$$

Slope of flange at ID

$$\theta_B := \frac{5.46}{\pi \cdot t^3}\left(J_S \cdot M_S + J_P \cdot M_P\right) \cdot \frac{1}{E}$$

Contact force between flanges at h_c

$$H_C := \frac{M_P + M_S}{h_C}$$

Bolt load at operating conditions

$$W_{m1} := H + H_G + H_C$$

Radial flange stress at inside diameter

$$S_{R\_ID} := -\left(\frac{2 \cdot F \cdot t}{\sqrt{B \cdot g_0} + F \cdot t} + 6\right) \cdot \frac{M_S}{\pi \cdot B \cdot t^2}$$

Radial flange stress at bolt circle

$$S_{R\_BC} := 6 \cdot \frac{\left(M_P + M_S\right)}{t^2 \cdot \left(\pi \cdot C - n \cdot D\right)}$$

Tangential stress at inside diameter

$$S_T := \frac{t \cdot E \cdot \theta_B}{B} + \left(\frac{2 \cdot F \cdot t \cdot Z}{\sqrt{B \cdot g_0} + F \cdot t} - 1.8\right) \cdot \frac{M_S}{\pi \cdot B \cdot t^2}$$

Longitudinal hub stress

$$S_H := \frac{\sqrt{B \cdot g_0} \cdot E \cdot \theta_B \cdot f}{0.91 \cdot \left(\frac{g_1}{g_0}\right)^2 \cdot B \cdot V}$$

Operating Bolt Stress:

Per Y-7 (a): $\sigma_b < S_b$

$$\sigma_b := \frac{W_{m1}}{A_b} \qquad \sigma_b = 1.218 \times 10^4 \frac{lb}{in^2} < S_b = 3.5 \times 10^4 \frac{lb}{in^2}$$

Design Prestress in Bolts

$$S_i := \sigma_b - \frac{1.159 \cdot h_C^{\,2} \cdot \left(M_P + M_S\right)}{a \cdot t^3 \cdot l \cdot r_E \cdot B} \qquad S_i = 1.215 \times 10^4 \frac{lb}{in^2}$$

Flange Design Stress Conditions:

$$S_{R\_BC} = 1.451 \times 10^3 \frac{lb}{in^2} \quad S_H = 0 \frac{lb}{in^2} \quad S_{R\_ID} = 0 \frac{lb}{in^2} \quad S_T = 3.685 \times 10^3 \frac{lb}{in^2} < S_f = 2.5 \times 10^4 \frac{lb}{in^2}$$

Highlighted in the previous calculation, all of the Appendix Y [4] conditions are met for the design pressure. Furthermore, the bolt stresses are determined to be the limiting factor and a corresponding maximum pressure of this assembly was found to be 1440 psig by iterating the pressure until the operating bolt stress equaled the allowable stress value.

The compression space and the adjacent bores through the centerplate to the TBT and Inertance tube are analyzed as a "thick cylindrical shell" per Appendix 1 of Reference [4].

P = hydrostatic proof test pressure
t = wall thickness
r = internal radius of tube
S = allowable stress value of Type 304 stainless steel
Z, z = factors

$$P := 500\,\frac{lb}{in^2} \qquad S := 20 \cdot 10^3\,\frac{lb}{in^2} \qquad Z := \frac{S + P}{S - P}$$

Lower (Inertance) Bore:

$r_{lower} := 0.495\,in$

$t_{lower} := r_{lower} \cdot \left(\sqrt{Z} - 1\right)$

$t_{lower} = 0.013\ in$

$t_{lower\_actual} := 1.118\,in$

$z_{lower} := \left(\frac{r_{lower} + t_{lower\_actual}}{r_{lower}}\right)^2$

$P_{lower\_max} := S \cdot \left(\frac{z_{lower} - 1}{z_{lower} + 1}\right)$

$P_{lower\_max} = 1.656 \times 10^4\,\frac{lb}{in^2}$

Middle (Compression Space) Bore:

$r_{middle} := 1.000\,in$

$t_{middle} := r_{middle} \cdot \left(\sqrt{Z} - 1\right)$

$t_{middle} = 0.025\ in$

$t_{middle\_actual} := 0.440\,in$

$z_{middle} := \left(\frac{r_{middle} + t_{middle\_actual}}{r_{middle}}\right)^2$

$P_{middle\_max} := S \cdot \left(\frac{z_{middle} - 1}{z_{middle} + 1}\right)$

$P_{middle\_max} = 6.986 \times 10^3\,\frac{lb}{in^2}$

Upper (TBT) Bore:

$r_{upper} := \frac{15}{16}\,in$

$t_{upper} := r_{upper} \cdot \left(\sqrt{Z} - 1\right)$

$t_{upper} = 0.024\ in$

$t_{upper\_actual} := t_{lower\_actual}$

$z_{upper} := \left(\frac{r_{upper} + t_{upper\_actual}}{r_{upper}}\right)^2$

$P_{upper\_max} := S \cdot \left(\frac{z_{upper} - 1}{z_{upper} + 1}\right)$

$P_{upper\_max} = 1.311 \times 10^4\,\frac{lb}{in^2}$

The actual lower and upper thicknesses used in the above calculation are based on the geometry at the thinnest wall portion of each bore and the actual middle thickness is based on a pressure transducer's countersunk seating surface along the middle bore, both conservative values. The corresponding maximum pressure for the center plate bores, based on the middle Compression Space bore is 6,986 psig.

The thread engagement length for the flange assemblies on either side of the Centerplate (TBT loose type flange and the Centerplate flange) are analyzed below. Both of these assemblies have identical bolt circles and geometries.

S_b = Allowable stress of bolt material at design temperature (ASTM A574)
S = Allowable stress of tapped material (stainless steel) at design temperature
D = nominal bolt diameter
L = length of thread engagement

$$S_S := 35 \cdot 10^3 \frac{lb}{in^2} \quad S := 20 \cdot 10^3 \frac{lb}{in^2} \quad D := 0.250\,in \quad L := 0.75 \cdot D \cdot \frac{S_S}{S} \quad L = 0.328\ in$$

The actual thread engagement is 0.380 inches which is greater than the required length of 0.328 inches.

B.4.10 Alternator Vessel

The two alternator vessels are geometrically the same and will be bolted to the Centerplate as depicted in Figure B.10. There is flange face contact outside of the bolt circle in this situation (as in the Compliance flange calculation of B.4.7); therefore the following calculation is also based on Appendix Y of Reference [4].

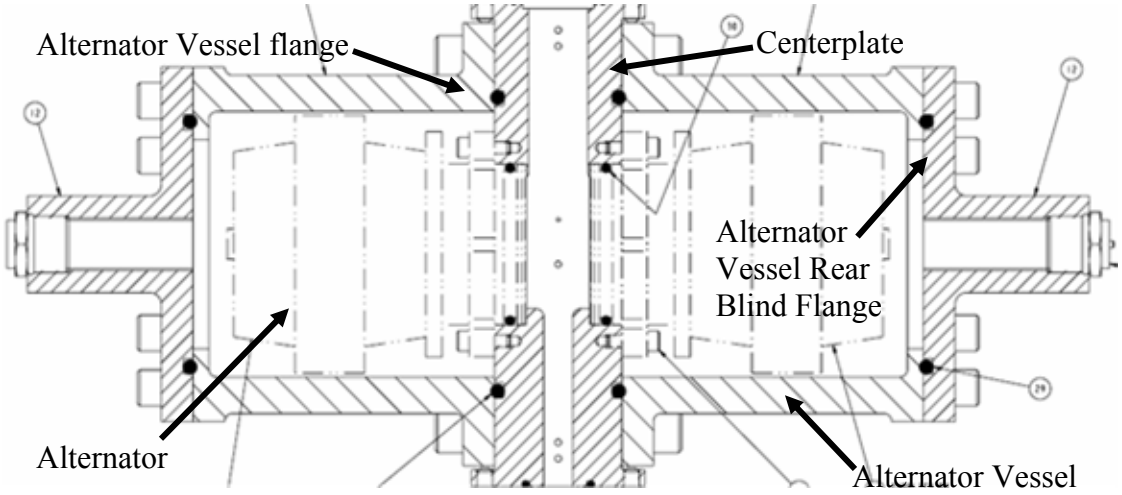

Figure B.10: TAPC cross-section through Alternator Vessels

Firstly, the alternator vessel flange is considered the "non-reducing" flange (denoted with a subscript I) and the centerplate is the "reducing" flange (subscript II). Next the flange assembly is characterized per Y-5. The inside diameter of the reducing flange is less than one-half of the bolt circle, therefore this assembly is a "Class 3" assembly per Y.5-1 (c). Furthermore, the non-reducing flange is an "integral flange" per Figure 2-4 of Appendix 2 [4], qualifying it as a "Category 1" flange.

A = outside diameter of flange
A_b = cross-sectional area of bolts using root diameter
A_m = total required cross-sectional area of bolts at thread root under operating stress
B = inside flange diameter
B_1 = B (if $B<20g_1$)
b = effective joint-contact-surface seating
C = bolt-circle diameter
d = factor
D = root diameter of 7/16-14 bolt
e = factor
f = hub stress correction factor (fig. 2-7.6)
G = diameter at location of gasket load reaction
g_1 = thickness of hub at back of flange
H = total hydrostatic end force
h_C = radial distance from bolt circle to flange-flange tangential contact
H_C = contact force between mating flanges
H_D = hydrostatic end force on area inside flange
H_p = total joint – contact surface compression load = 0lb (for o-rings)
H_T = difference between H and H_D
h_D, h_G, h_T = moment arms to respective loads
ID_o = inside diameter of O-ring
K_f = ratio of outside flange diameter to inside diameter = A/B
L = factor
M_o = total moment acting on the flange under operating conditions
M_G = moment based on gasket seating
M_0 = the greater moment between M_o and M_G
m = gasket factor = 0 for O-rings (self energizing per Appendix 2 - Table 2-5.1)
N = number of bolt holes in the flange
P = internal design pressure of hydrostatic proof test (per UG-100)
S_a = allowable bolt stress at atmospheric temperature
S_b = allowable bolt stress at design temperature
S_f = allowable design stress for the material of the flange at design temperature
S_H = calculated longitudinal stress in hub
S_R = calculated tangential stress in flange
S_T = calculated tangential stress in flange

R = radial distance from bolt circle to point of intersection of hub and back of flange
t = flange thickness
U = factor involving K (fig. 2-7.1)
V = factor for integral flanges (fig 2-7.3)
W = flange design bolt load under operation
W_{m1} = minimum required bolt load for the operating conditions (Appendix Y-4 [4])
w = width of O-ring
Y = factor involving K (fig. 2-7.1)
Z = factor involving K (fig. 2-7.1)

Internal Proof Test Pressure

$P := 500\frac{lb}{in^2}$

Flange and Bolt Geometry

$A := 6.250in \quad C := 6.12in \quad g_0 := 0.565in \quad n := 10 \quad h_C := 0.378in \quad d := 0.3602in \quad A_b := n \cdot \left[\pi \cdot \left(\frac{d}{2}\right)^2\right]$

$B := 4.125in \quad D := 0.5in \quad g_1 := g_0 \quad G := 4.56in \quad t_I := 0.5in \quad t_{II} := 0.75in$

$B_1 := B + g_0$ let : $B := B_1 \quad m := 0 \quad d_B := \frac{7}{16}in$

$R_0 := \frac{C - B}{2} - g_1 \quad h_D := R_0 + 0.5g_1 \quad h_G := \frac{C - G}{2} \quad h_T := \frac{R_0 + g_1 + h_G}{2} \quad l := t_I + t_{II} + \frac{1}{2} \cdot d_B$

Material Values

$E_I := 27.5 \cdot 10^6 \frac{lb}{in^2} \quad E_{II} := 29.4 \cdot 10^6 \frac{lb}{in^2} \quad S_f := 25.0 \cdot 10^3 \frac{lb}{in^2} \quad S_b := 33.8 \cdot 10^3 \frac{lb}{in^2} \quad E_{bolt} := E_I \quad r_{EII} := \frac{E_{II}}{E_{bolt}} \quad r_{EI} := \frac{E_I}{E_{bolt}}$

Calculation Forces and Factors

$\beta := \frac{C + B_1}{2B_1} \quad a := \frac{A + C}{2B_1} \quad AR := \frac{n \cdot D}{\pi C} \quad f := 1 \quad H := 0.785 \cdot G^2 \cdot P \quad H_p := 0lb \quad H_D := 0.785 \cdot B_1{}^2 \cdot P$

$H_T := H - H_D \quad H_G := 0lb \quad M_P := H_D \cdot h_D + H_T \cdot h_T + H_G \cdot h_G \quad M_s := 0$

$r_B := \frac{1}{n}\left(\frac{4}{\sqrt{1 - AR^2}} \operatorname{atan}\left(\sqrt{\frac{1 + AR}{1 - AR}}\right) - \pi - 2AR\right) \quad J_S := \frac{1}{B_1}\left(\frac{2h_D}{\beta} + \frac{h_C}{a}\right) + \pi \cdot r_B \quad J_P := \frac{1}{B_1}\left(\frac{h_D}{\beta} + \frac{h_C}{a}\right) + \pi \cdot r_B$

(Fig. 2-7.2) (Fig. 2-7.3)

$C_1 := \frac{-\left(0.748 - 1.567J_S \cdot \log\left(\frac{A}{B_1}\right)\right)}{\left(1 + 1.3J_S\right)} \quad C_2 := \frac{\left[\frac{\pi}{32}\left(P \cdot B_1{}^3\right) - 1.3J_P \cdot M_P\right]}{1 + 1.3J_S} \quad C_3 := 0 \quad F := 0.908920 \quad V := 0.550103 \quad C_4 := 0lb \cdot ft$

$X := \frac{E_I \cdot t_I{}^3}{E_I \cdot t_I{}^3 + E_{II} \cdot t_{II}{}^3} \quad F_I := g_0{}^2 \cdot \frac{\left(\sqrt{B \cdot g_0} + F \cdot t_I\right)}{V} \quad Z := \frac{\left(\frac{A}{B}\right)^2 + 1}{\left(\frac{A}{B}\right)^2 - 1}$

Rigid Body Rotation of Flanges

$\theta_I := \frac{X \cdot (C_4 - C_2)}{1.206 \cdot \log\left(\frac{A}{B_1}\right) - X \cdot C_3 - (1 - X) \cdot C_1} \cdot \frac{1}{E_I \cdot t_I{}^3} \quad \theta_{II} := -E_I \cdot t_I{}^3 \cdot \theta_I \cdot \left(\frac{E_{II} \cdot t_{II}{}^3}{E_I \cdot t_I{}^3}\right) \cdot \frac{1}{E_{II} \cdot t_{II}{}^3}$

Total Flange Moment at Diameter B_1

$M_{SI} := C_3 \cdot \left(E_I \cdot t_I{}^3 \cdot \theta_I\right) + C_4$

$M_{SII} := C_1 \cdot \left(E_{II} \cdot t_{II}{}^3 \cdot \theta_{II}\right) + C_2$

Unbalanced Flange Moment at Diameter B_1

$M_{uI} := 1.2068\left(E_I \cdot t_I{}^3 \cdot \theta_I\right) \cdot \log\left(\frac{A}{B_1}\right)$

$M_{uII} := 1.2068\left(E_{II} \cdot t_{II}{}^3 \cdot \theta_{II}\right) \cdot \log\left(\frac{A}{B_1}\right)$

Balanced Flange Moment at Diameter B 1

$M_{bI} := M_{SI} - M_{uI}$

$M_{bII} := M_{SII} - M_{uII}$

Slope of Flange at Diameter B 1

$$\theta_{BI} := \left[\frac{5.46}{\pi \cdot t_I^{\,3}} \cdot \left(J_S \cdot M_{bI} + J_P \cdot M_P\right) + E_{II} \cdot t_I^{\,3} \cdot \frac{\theta_I}{t_I^{\,3}}\right] \cdot \left(\frac{1}{E_I}\right)$$

$$H_C := \frac{M_P + M_{bI}}{h_C} \qquad W_{m1} := H + H_G + H_C$$

$$\theta_{BII} := \left[-1.337 \cdot \left(M_{SII} - \pi \cdot P \cdot \frac{B_1^{\,3}}{32}\right) \cdot \frac{1}{t_{II}^{\,3}}\right] \cdot \left(\frac{1}{E_{II}}\right)$$

Operating Bolt Stress:

Per Y-7 (a): $\sigma_b < S_b$

$$\sigma_b := \frac{W_{m1}}{A_b} \qquad \sigma_b = 1.727 \times 10^4 \frac{lb}{in^2} < S_b = 3.38 \times 10^4 \frac{lb}{in^2}$$

Design Prestress in Bolts:

$$S_i := \sigma_b - \frac{1.159 \cdot h_C^{\,2} \cdot \left(M_P + M_{bI}\right)}{2(1 - X)\, a \cdot t_I^{\,3} \cdot l \cdot r_{EI} \cdot B_1} \qquad S_i = 1.$$

Flange I (non-reducing flange) Stresses:

Radial Stress @ Bolt Circle:

$$S_{RBCI} := \frac{6 \cdot \left(M_P + M_{SI}\right)}{t_I^{\,2} \cdot \left(\pi \cdot C - n \cdot D\right)}$$

Per Y-7 (c): $S_R < S_f$

$$S_{RBCI} = 5.704 \times 10^3 \frac{lb}{in^2} < S_f = 2.5 \times 10^4 \frac{lb}{in^2}$$

Radial @ ID :

$$S_{RIDI} := -\left(\frac{2F \cdot t_I}{\sqrt{B \cdot g_0} + F \cdot t_I} + 6\right) \cdot \frac{M_{SI}}{\pi \cdot B_1 \cdot t_I^{\,2}}$$

$$S_{RIDI} = 0 \frac{lb}{in^2} < S_f = 2.5 \times 10^4 \frac{lb}{in^2}$$

Tangential @ ID :

$$S_{TI} := \frac{t_I \cdot E_I \cdot \theta_{BI}}{B_1} + \left(\frac{2 \cdot F \cdot t_I \cdot Z}{\sqrt{B \cdot g_0} + F \cdot t_I} - 1.8\right) \cdot \frac{M_{SI}}{\pi \cdot B_1 \cdot t_I^{\,2}}$$

Per Y-7 (d): $S_T < S_f$

$$S_{TI} = -131.114 \frac{lb}{in^2} < S_f = 2.5 \times 10^4 \frac{lb}{in^2}$$

Longitudinal Hub Stress in Flange I :

$$S_{HI} := \frac{\sqrt{B \cdot g_0} \cdot E_I \cdot \theta_{BI} \cdot f}{0.91 \cdot \left(\frac{g_1}{g_0}\right)^2 \cdot B_1 \cdot V}$$

Per Y-7 (e): $(S_H + S_R)/2$ and $(S_H + S_T)/2 < S_f$

$$\frac{S_{HI} + S_{RBCI}}{2} = 2.426 \times 10^3 \frac{lb}{in^2}$$

$$\frac{S_{HI} + S_{RIDI}}{2} = -426.359 \frac{lb}{in^2} < S_f = 2.5 \times 10^4$$

$$\frac{S_{HI} + S_{TI}}{2} = -491.916 \frac{lb}{in^2}$$

Flange II (reducing flange) Stresses:

Radial Stresses

@ Bolt Circle:

$$S_{RBCII} := \frac{6 \cdot \left(M_P + M_{SII}\right)}{t_{II}^{\,2}\left(\pi \cdot C - n \cdot D\right)}$$

@ B_1:

$$S_{RBII} := \frac{6 \cdot M_{SII}}{\pi B_1 \cdot t_{II}^{\,2}}$$

Per Y-7 (c): $S_R < S_f$

$$S_{RBCII} = 3.177 \times 10^3 \frac{lb}{in^2}$$

$$S_{RBII} = 619.901 \frac{lb}{in^2} < S_f = 2.5 \times 10^4 \frac{lb}{in^2}$$

@ center of Flange II :

$$S_{RCII} := \frac{0.3094 \cdot P \cdot B_1^{\,2}}{t_{II}^{\,2}} - 6 \cdot \frac{M_{SII}}{\pi \cdot B_1 \cdot t_{II}^{\,2}}$$

$$S_{RCII} = 5.43 \times 10^3 \frac{lb}{in^2}$$

Tangential Stresses

@ B_1:

$$S_{TBII} := \frac{t_{II} \cdot E_{II} \cdot \theta_{BII}}{B_1} - \frac{1.8 \cdot M_{SII}}{\pi \cdot B_1 \cdot t_{II}^2}$$

@ center of Flange II :

$$S_{TCII} := S_{RCII}$$

Per Y-7 (d): $S_T < S_f$

$$S_{TBII} = 1.946 \times 10^3 \frac{lb}{in^2} \quad < \quad S_f = 2.5 \times 10^4 \frac{lb}{in^2}$$

$$S_{TCII} = 5.43 \times 10^3 \frac{lb}{in^2}$$

Per Y-7 (e): $(S_H+S_R)/2$ and $(S_H+S_T)/2 < S_f$

$$\frac{S_{HI} + S_{RBCII}}{2} = 1.162 \times 10^3 \frac{lb}{in^2}$$

$$\frac{S_{HI} + S_{RBII}}{2} = -116.408 \frac{lb}{in^2}$$

$$\frac{S_{HI} + S_{RCII}}{2} = 2.288 \times 10^3 \frac{lb}{in^2} \quad < \quad S_f = 2.5 \times 10^4 \frac{lb}{in^2}$$

$$\frac{S_{HI} + S_{TI}}{2} = -491.916 \frac{lb}{in^2}$$

Per Y-7 (f): S_R and $S_T < S_f$:

$$S_{RCII} = 5.43 \times 10^3 \frac{lb}{in^2} \quad < \quad S_f = 2.5 \times 10^4 \frac{lb}{in^2}$$

$$S_{TCII} = 5.43 \times 10^3 \frac{lb}{in^2}$$

Pressure $_{max}$ = 1000psi

The bolt stress is the limiting component in the previous calculation and a corresponding maximum pressure of 1000 psig is determined through iteration.

The wall thickness of the Alternator Vessel is analyzed as a tube per UG-27 [4].

$$P := 500 \frac{lb}{in^2} \qquad r := 2.060\,in \qquad S := 20 \cdot 10^3 \frac{lb}{in^2}$$

$$t := \frac{P \cdot r}{S - 0.6 \cdot P} \qquad t = 0.052\ in$$

$$t_{actual} := 0.565\,in \qquad P_{max} := \frac{S \cdot t_{actual}}{r + 0.6 \cdot t_{actual}} \qquad P_{max} = 4.71 \times 10^3 \frac{lb}{in^2}$$

The previous calculation proves that the alternator vessel wall can maintain a maximum pressure of 4,710psig.

The alternator vessels are capped with identical blind flanges, which are also analyzed as blind flanges per UG-34 [4]. The flange geometry as well as the stress in the bolts is analyzed in the following calculation in order to determine the limiting component.

A = cross-sectional area of bolt at root diameter
c = factor depending on method of attachment = 0.25 for bolts (Fig UG-34p)
D = root diameter of bolt
d = bolt circle diameter

f_{joint} = joint factor based on flange assembly
f_{safety} = factor of safety
G = mean o-ring diameter
H = total hydrostatic end force on area inside flange
h_G = gasket moment arm = radial distance from bolts to gasket reaction
n = number of bolts
P = internal design pressure
P_{max_t} = maximum pressure based on flange thickness
S_f = maximum allowable stress of flange material
S_b = maximum allowable stress of bolt material
σ_{bolt} = required prestress in bolts
t = minimum required flange thickness
W = total bolt load

Internal Design Pressure:

$P := 500 \frac{lb}{in^2}$

Material Values:

$S_f := 20 \cdot 10^3 \frac{lb}{in^2}$ $S_b := 35 \cdot 10^3 \frac{lb}{in^2}$

Assembly Geometry:

$D := 0.3073\,in$ $d := 4.685\,in$ $G := 4.020\,in$ $n := 10$ $c := 0.25$

Flange Thickness:

$t := d \cdot \sqrt{\frac{c \cdot P}{S_f}}$ $t = 0.37\,in$ $t_{actual} := 0.5in$ $P_{max\_t} := \left[\left(\frac{t_{actual}}{d}\right)^2\right] \cdot \frac{S_f}{c}$ $P_{max\_t} = 911.194 \frac{lb}{in^2}$

Bolt Loading:

The minimum preload and prestress in the bolts to prevent separation upon pressurization:

$A_G := \pi \cdot \left(\frac{G}{2}\right)^2$ $A_{bolt} := \pi \cdot \left(\frac{D}{2}\right)^2$

$f_{joint} := 0.8$ $f_{safety} := 2$ $F_{blowoff} := A_G \cdot P$

$F_{preload} := \frac{F_{blowoff} \cdot f_{joint}}{n} \cdot f_{safety}$ $\sigma_{bolt} := \frac{F_{preload}}{A_{bolt}}$ $\sigma_{bolt} = 1.369 \times 10^4 \frac{lb}{in^2} < S_b = 3.5 \times 10^4 \frac{lb}{in^2}$

$Pressure_{max} = 911$ psi

The allowable bolt stress is greater than the required pre-stress; therefore the bolts chosen are sufficient. Finally, the maximum internal pressure for this flange assembly is determined by iterating the design pressure until either the required thickness (t) becomes greater than the actual thickness (t_{actual}) or the bolt stress (σ_b) becomes greater than the allowable stress (S_b). It turns out that the flange thickness equals the actual thickness at 911psig, which is therefore the maximum pressure contained by the Alternator Vessel Rear Blind Flanges.

B.4.11 Jet Pump

The jet pump causes the helium to experience a pressure drop as it oscillates between the AHX and Compliance regions, however, the exact location to provide the correct pressure change isn't exactly known. Therefore, this part is designed to translate axially by screwing it one way or the other through the Compliance flange. In order to prevent this part from being screwed out of the flange, there is a "lip" machined into the component just above the threaded portion. Likewise, screwing too far up is prevented by an interference between the top of the jet pump and a bore in the ambient heat exchanger. These interferences ensure that there are always a sufficient number of threads in contact.

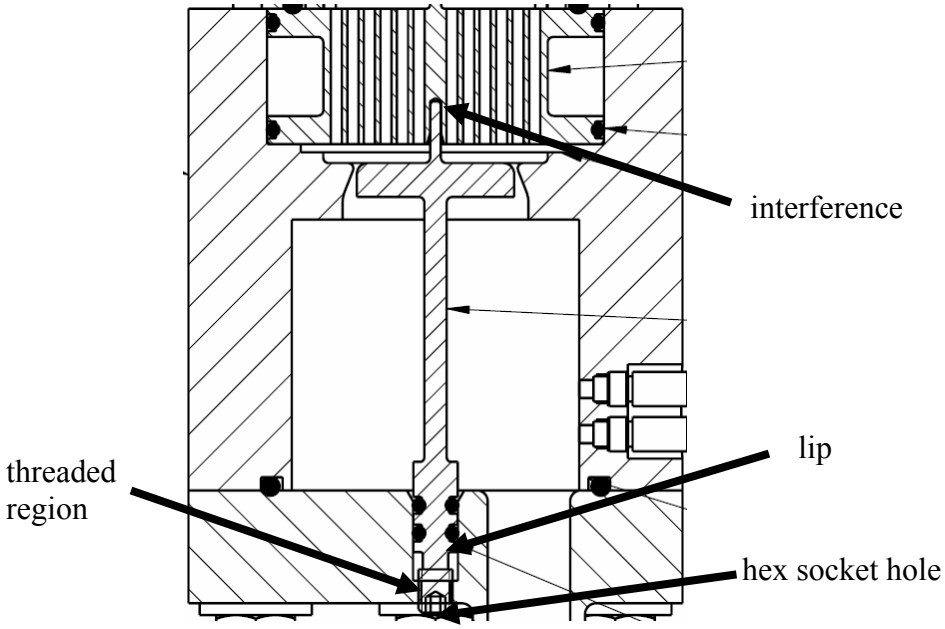

Figure B.11: Jet Pump assembly

UG-43 (g) [4] specifies the length of thread engagement for a stud to be the greater of the values between the nominal diameter and the length determined in the calculation below.

S_s = allowable stress of stud (jet pump) material (Type 304 stainless steel)
S = allowable stress of tapped material (Compliance flange) at design temperature
D = nominal bolt diameter
L = length of thread engagement

$$S_S := 25 \cdot 10^3 \frac{lb}{in^2} \quad S := 20 \cdot 10^3 \frac{lb}{in^2} \quad D := 0.190\,in \quad L := 0.75 \cdot D \cdot \frac{S_S}{S} \quad L = 0.178\ in$$

The length is less than the nominal diameter; therefore the thread engagement length should be a minimum of 0.125 inches at all times, which is less than the actual minimum length of 0.158 inches (based on the location of the interferences).

B.4.12 Other Components

Various Swagelok fittings and sensors will be sealed to the TAPC pressure vessel. The pressure ratings of these components are shown below in Table B.6.

Table B.6: Component pressure ratings.

Component	Maximum Pressure (psig)
Piezoelectric Pressure Transducer	2,000
Piezoresistive Pressure Transducer	10,000
Linear Variable Differential Transducer	3,000
Swagelok Tube Fitting Union	3,626
Swagelok Male Connector (O-seal Fitting)	3,000
Swagelok 3-Way Switching Valve	2,500

REFERENCES

[1] Backhaus S., Tward, E. and Petach, M. (2004). "Traveling-wave thermoacoustic electric generator," Applied Physics Letters

[2] CFIC (Clever Fellows Innovation Consortium, Inc.) Q Drive: Resonant Power Systems. www.qdrive.com (accessed March 1, 2006).

[3] Ward, W. and Swift, G. (1994) "Design Environment for Low Amplitude Thermoacoustic Engines, DeltaE," J. Acoust. Soc. Am., Vol. 95, pp. 3671-3672.

[4] ASME Boiler and Pressure Vessel Code, Section VIII, Division 1 (2004): Rules for Construction of Pressure Vessels.

[5] Swift, G. (2004) "A Brief Description of Thermoacoustics," Special Lay-Language Paper for ASA's 75th Anniversary Meeting. www.acoustics.org/press/147th/thermoacoustics.htm (accessed August 3, 2004).

[6] Garret, S. and Backhaus, S. "American Scientist Online - The Power of Sound," www.americanscientist.org (accessed August 3, 2004).

[7] Backhaus, S. and Swift, G. (2002) "New Varieties of Thermoacoustic Engines," LANL Report No. LA-UR 02-2721. 9th International Congress on Sound and Vibration.

[8] Hartley, R. (1951) "Electric Power Source," U.S. Patent No. 2,549,464.

[9] Marrison, W. (1958) "Heat-Controlled Acoustic Wave System," U.S. Patent No. 2,836,033.

[10] Ceperley, P. (1979) "A Pistonless Stirling Engine – The traveling wave heat engine," J. Acoust. Soc. Am., Vol. 66, pp. 1508-1513.

[11] Ceperley, P. (1982) "Resonant Traveling Wave Engine," U. S. Patent No. 4,355,517.

[12] Yazaki, T., Iwata, A., Maekawa, T. and Tominaga A. (1998) "Traveling Wave Thermoacoustic Engine in a Looped Tube," Physical Review Letters, Vol. 81, pp. 3128-3131.

[13] Backhaus, S. and Swift, G. (2000) "A thermoacoustic-Stirling heat engine: Detailed Study," J. Acoust. Soc. Am., Vol. 107, pp. 3148-3166.

[14] Backhaus, S. and Swift, G. (1999) "A thermoacoustic Stirling heat engine," Nature, Vol. 399, pp. 335-338.

[15] Petach, M., Tward, E. and Backhaus, S. (2004) "Design Of A High Efficiency Power Source (HEPS) Based On Thermoacoustic Technology," Final report, NASA contract no. NAS3-01103, CDRL 3f.

[16] Swift, G. (1988) "Thermoacoustic engines," J. Acoust. Soc. Am., Vol. 84, pp. 1145-1180.

[17] Feldman, K. T. Jr. (1968) "Review of the literature on Sondhauss thermoacoustic phenomena," J. Sound Vib. Vol. 7, pp. 71.

[18] Swift, G. (2002) *Thermoacoustics: A Unifying Perspective for Some Engines and Refrigerators*. Acoustical Society of America, Melville, NY.

[19] Backhaus, S. and Reid, R. (2005) "A Self-Circulating Heat Exchanger for Use in Stirling and Thermoacoustic-Stirling Engines," *Space Technology and Applications International Forum* – STAIF 2005. American Institute of Physics 0-7354-0230-2/05, pp 719-726.

[20] Olson, J. and Swift, G. (1994) "Similitude in Thermoacoustics," J. Acoust. Soc. Am., Vol. 95, pp. 1405-1412.

[21] Sun, D., Qiu, L., Zhang, W., Yan, W. and Chen, G. (2004) "Investigation on traveling wave thermoacoustic heat engine with high pressure amplitude," Energy Conversion and Management, Vol. 46, pp. 281-291.

[22] Weiland, N. (2004) "Feasibility Analysis of an Open Cycle Thermoacoustic Engine with Internal Pulse Combustion," Ph.D. dissertation, School of Mechanical Engineering, Georgia Institute of Technology.

[23] Avallone, E. and Baumeister, T. (1996) *Marks' Standard Handbook for Mechanical Engineering, 10th Edition.* pp. 4-12.

[24] Ceperley, P. (1988) "Gain and efficiency of a short traveling wave heat engine," J. Acoust. Soc. Am., Vol. 77, pp. 1239-1244.

[25] Backhaus, S. (2005) – Los Alamos National Laboratory. Private communications.

[26] Kinsler, L., Frey, A., Coppens, A. and Sanders, J. (1982) *Fundamentals of Acoustics, 3rd Edition.* John Wiley and Sons Publishing.

[27] Wollan, J., Swift, G., Backhaus, S. and Gardner, D. (2002) "Development of a Thermoacoustic Natural Gas Liquefier," LA-UR 02-1623. 2002 AIChE Meeting.

[28] Pahl, G. and Beitz, W. (1996) *Engineering Design: A Systematic Approach, 2nd Edition.* Spring-Verlag Publishing.

[29] Schewe, P. and Stein, B. "Acoustically Powered Deep-Space Electric Generator," www.aip.org/pnu/2004/split/695-2.html (accessed September 22, 2004).

[30] Hanson, T. "A traveling-wave engine to power deep space travel," www.lanl.gov/worldview/news/releases/archive/04-078.shtml (accessed September 21, 2004).

[31] Swagelok fittings. www.swagelok.com (accessed March 1, 2006).

[32] Spoor, P. and Swift, G. (1999) "Mode-locking of acoustic resonators and its application to vibration cancellation in acoustic heat engines," J. Acoust. Soc. Am., Vol. 106, pp. 1353-1362.

[33] Backhaus, S. (2004) – Los Alamos National Laboratory. Private communications.

[34] Ward, B. and Swift, G. (2001) "Design Environment for Low-Amplitude ThermoAcoustic Engines (DELTAE) Version 5.1 – Tutorial and User's Guide." LANL Report No. LA-CC-93-8. http://www.lanl.gov/thermoacoustics/.

[35] Taylor Forge & Pipe works. (1964) *Modern Flange Design.* Chicago, Illinois.

[36] Omegalux® High Watt Density Cartridge Heaters. www.omega.com (accessed March 1, 2006).

[37] Abaqus Finite Element Analysis Software. www.abaqus.com (accessed March 1, 2006).

[38] Wuthrich, J. (2005) – Lockheed Martin Corporation Private communications.

[39] Tlusty, G. (2000) *Manufacturing Processes and Equipment.* Prentice Hall.

[40] Organ, A. (1992) *Thermodynamics and Gas Dynamics of the Stirling Cycle Machine.* Cambridge University Press.

[41] Sefar America Inc., Monterey Park, California. www.sefar.com (accessed March 1, 2006).

[42] Alconox® - Powdered Precision Cleaner. www.alconox.com (accessed March 1, 2006).

[43] Olson, J. and Swift, G. (1997) "Acoustic streaming in pulse tube refrigerators: Tapered pulse tubes," Cryogenics, Vol. 37, pp. 769-776.

[44] Nebergall, W., Schmidt, F. and Holtzclaw, H. (1972) *General Chemistry, 4th Edition.* DC Heat and Company

[45] Swagelok® Tubing Data (1999). www.swagelok.com (accessed March 1, 2006).

[46] Idelchik, I.E. (2001) *Handbook of Hydraulic Resistance, 3rd Edition.* Begell House.

[47] Gedeon, D. (1997) "DC gas flows in Stirling and pulse-tube cryocoolers," *Cryocoolers 9*. Plenum, NY.

[48] Backhaus, S. and Swift, G. (2003) "An acoustic streaming instability in thermoacoustic devices utilizing jet pumps," J. Acoust. Soc. Am., Vol. 113, pp. 1317-1324.

[49] Smith, B. and Swift, G. (2003) "Power dissipation and time-averaged pressure in oscillating flow through a sudden area change," J. Acoust. Soc. Am., Vol. 113, pp. 2455-2463.

[50] Parker Hannifin Corporation: O-Ring Division. www.parker.com/o-ring (accessed March 1, 2006).

[51] Backhaus, S. (2006) – Los Alamos National Laboratory. Private communications.

[52] Omega® www.omega.com (accessed March 1, 2006).

[53] Douglas Electrical Components, Inc. www.douglaselectrical.com (accessed November 10, 2004).

[54] Harris Single Stage HVAC Regulator: Model 25. www.weldingmart.com (accessed April 1, 2005).

[55] Swagelok PGI Series B Model Positive Pressure Gauge. www.swagelok.com (accessed March 1, 2006).

[56] Endevco Model 8510B-2000. www.endevco.com (accessed November 10, 2004).

[57] Endevco Model 136. www.endevco.com (accessed November 10, 2004).

[58] PCB Piezotronics Inc. Model 105C12. www.pcb.com (accessed March 1, 2006).

[59] Schaevitz Model 249 XS-C. www.schaevitz.com (accessed November 10, 2004).

[60] Fluke 45 Dual Display Multimeter. www.fluke.com (accessed March 1, 2006).

[61] Fahy, F. (1977) "Measurement of acoustic Intensity Using the Cross-Spectral Density of Two Microphone Signals," J. Acoust. Soc. Am., Vol. 62, page 1067-1069.

[62] Fusco, A., Ward, W. and Swift, G. (1991) "Two-sensor power measurements in lossy ducts," J. Acoust. Soc. Am., Vol. 91, pp. 2229-2235.

[63] Holland, K. and Davies, P. (2000) "The Measurement of Sound Power Flux in Flow Ducts." J. Sound Vibration. Vol. 230, page 915-932.

[64] Ådom, M. and Bodén, H. (1988) "Error analysis of two-microphone measurements in ducts with flow." J. Acoust. Soc. Am., Vol. 83, page 2429-2438.

[65] Stanford Research Systems Digital Lock-In Amplifier Model SR830. www.thinkSRS.com (accessed March 1, 2006).

[66] Ohmite Wirewound Power Rheostats Model L 150 Watt. www.newarkinone.com (accessed December 1, 2005).

[67] Voltech™ PM3000A Power Analyzer. www.voltech.com (accessed March 1, 2006).

[68] Digi-Sense® Temperature Controller Model 230 Volt. www.coleparmer.com (accessed November 1, 2005).

[69] Lambda EMI Power Supply: Model EMS 300V-3.5A Series Switch Mode DC Power Supply. www.emipower.com (accessed March 1, 2006).

[70] Xantrex Model XFR 150V-18A. www.xantrex.com (accessed March 1, 2006).

[71] Thermo Neslab Digital One Model RTE7. www.thermo.com (accessed March 1, 2006).

[72] Elgar Continuous Wave AC Power Source Model CW801. www.elgar.com (accessed December 15, 2005).

[73] National Instruments Chassis Model SCXI 1001. www.ni.com (accessed October 15, 2005).

[74] National Instruments M Series Data Acquisition 1.25 Mega Samples/second card. www.ni.com (accessed October 15, 2005).

[75] National Instruments SCXI 8 Channel Simultaneous Sampling Module. www.ni.com (accessed October 15, 2005).

[76] National Instruments LabVIEW Version 7.1 Software. www.ni.com (accessed October 15, 2005).

[77] Corey, J. (2006) – CFIC, Inc. QDrive. Private communications.

[78] Keolian, R. (2006) - Applied Research Laboratory and The Pennsylvania State University. Private communications.

[79] Olson, J. and Swift, G. (1999) "Suppression of acoustic streaming in tapered pulse tubes," *Cryocoolers 10*. Plenum, NY.

[80] Smith, B. and Glezer. A. (1998) "The formation and evolution of synthetic jets. Phys. Fluids, Vol. 10, pp. 2281-2297.

[81] ASME Boiler and Pressure Vessel Code, Section IX (2004): Welding and Brazing Qualifications.

[82] Helium Gas Leak Detector Model UE25420. www.davis.com (accessed January 15, 2006).

[83] Northeast Gas Technologies ltd. Albany, NY.

[84] O'Keefe orifice www.okcc.com (accessed March 1, 2006).

[85] Digi-Sense® Temperature Controller: $230V_{ac}$ model. www.coleparmer.com (accessed November 1, 2005).